Keyhole repair in precipitation hardening aluminum alloys using refill friction stir spot welding

Vom Promotionsausschuss der
Technischen Universität Hamburg

zur Erlangung des akademischen Grades

Doktor-Ingenieur (Dr.-Ing.)

genehmigte Dissertation

von
Martin Reimann

aus
Merseburg (Saale)

2018

Gutachter:	Prof. Dr.-Ing. habil. Norbert Huber
	Dr.-Ing. habil. Jan Oke Peters
Vorsitzender des Prüfungsausschusses:	Prof. Dr.-Ing. habil. Bodo Fiedler
Tag der mündlichen Prüfung:	16.10.2018

Abstract

Aluminum alloys are widely used in transportation industries because of the increasing need to reduce the environmental impact. With advances in technology, the demand for complex parts and components that must be produced using several processing methods has increased. During fabrication and service, a wide range of defects can appear in aluminum components and structures, which could be repaired using a suitable through hole closure method. The search for a friction-based solid-state keyhole repair technique that fulfills the requirements for high-quality repair welds has become an important research topic because conventional fusion welding is difficult to apply in many aluminum alloys. However, many commonly available friction-based welding methods are complex and multistage processes that require specially designed equipment and are not suitable for sealing through holes. The development of an adequate keyhole repair process is thus actual necessity.

The present study addresses the development of a suitable keyhole repair procedure of structural aluminum parts using the refill friction stir spot welding process (RFSSW). For this newly developed repair method, a plug made of a similar material is applied as a filler element into the keyhole and RFSSW is used to weld the plug to the surrounding workpiece. To cover a wide range of alloys and potential applications, the repair method was investigated in different precipitation hardening aluminum alloys as well as different keyhole diameters and workpiece thicknesses. A fundamental analysis of the process and resulting material properties considering the alloy-dependent metallurgical transformations was conducted. Moreover, a knowledge-based process analysis approach was chosen to study the behavior of the base material during high-shear-rate plastic deformation and exposure to typical thermal cycles, which are both associated with the conditions found during friction welding. The influence of the base material composition and properties on the energy input during friction welding was investigated and a comprehensive analysis of the friction condition and flow stress development was conducted.

The developed keyhole repair process using RFSSW is a universal through-hole closure method with advantages such as defect-free welds, high weld efficiencies and superior surface appearance on both sides of the weld. Within the scope of the present work, processing conditions were defined that lead to defect free repair welds for all investigated materials and workpiece dimensions. The area of lowest strength was in all cases found outside of the weld spot, mainly in the heat affected zone. For all welded precipitation hardening aluminum alloys, metallurgical analysis revealed that the evolution of the strengthening precipitates during and after the weld primarily determines the final mechanical properties. Significant differences observed in the response of the base materials to the process were found to be caused by the alloy composition, specifically by the characteristics of the present precipitates. The fundamental process analysis revealed that in precipitation hardening aluminum alloys, the mechanical properties obtained under quasi-static testing conditions are not adequate to describe or predict the base material properties at the high strain rates and thermal cycles associated with friction welding operations. The alloy composition, initial temper condition and general precipitation evolution during the specific thermal cycles resulting from the friction welding operations were found to determine the material properties at the tested rates of deformation. The knowledge gained by this fundamental process analysis is key to enabling rapid process optimization by guiding the appropriate choice of process parameters for a given alloy.

Zusammenfassung

Aufgrund des steigenden Druckes die Umweltbelastung zu verringern, werden Aluminiumlegierungen in der Transportbranche breitflächig eingesetzt. Durch den technologischen Fortschritt hat die Nachfrage nach komplexen Bauteilen und Komponenten, die unter Zuhilfenahme verschiedenster Bearbeitungsmethoden produziert werden, zugenommen. Während der Herstellung und Wartung von solchen Aluminiumkomponenten und –strukturen können vielfache Defekte auftreten, die durch eine geeignete Durchgangsloch-Verschlussmethode repariert werden könnten. Da herkömmliche Schweißverfahren in vielen Aluminiumlegierungen nur schwer anwendbar sind, ist aus der Suche nach einer reibbasierten Festphase-Bohrlochverschlussmethode, die den Anforderungen höchster Reparaturqualität gerecht wird, ein bedeutender Forschungszweig geworden. Dennoch sind viele der derzeit vorhandenen Reibschweißmethoden komplexe, mehrstufige Prozesse, die nur mit speziellen Anlagen durchgeführt werden können und nicht dazu geeignet sind, Durchgangslöcher zu verschließen. Die Entwicklung einer geeigneten Bohrlochreparaturmethode ist daher eine tatsächliche Notwendigkeit.

In dieser Arbeit wurde eine Methode zum Verschließen von Durchgangslöchern entwickelt, bei der das reibbasierte Schweißverfahren Refill Friction Stir Spot Welding (RFSSW) zur Bohrlochreparatur an Aluminiumkomponenten verwendet wird. Bei dieser neu entwickelten Reparaturmethode wird ein artgleicher Stopfen als Füllwerkstoff eingesetzt und durch das RFSSW mit dem umliegenden Werkstück verschweißt. Um eine breites Spektrum an Legierungen und möglichen Anwendungsgebieten abzudecken wurde die Reparaturmethode in verschiedenen ausscheidungshärtenden Aluminiumlegierungen sowie Durchgangslochdurchmessern und Werkstückdicken untersucht. Eine fundamentale Analyse des Prozesses und der resultierenden mechanischen Eigenschaften unter Berücksichtigung der legierungsspezifischen metallurgischen Vorgänge wurde durchgeführt. Darüber hinaus wurde ein wissensbasierter Ansatz zur Prozessanalyse gewählt, um das Grundmaterialverhalten während plastischer Deformation bei hohen Scherraten und unter Einfluss von reibschweiß-typischen Temperaturzyklen zu analysieren. Der Einfluss der Grundmaterialzusammensetzung und -eigenschaften auf den Energieeintrag während des Schweißprozesses wurde untersucht und eine umfassende Analyse der Reibbedingungen und Fließspannungsentwicklung durchgeführt.

Die entwickelte Bohrlochreparatur mittels RFSSW ist eine universell einsetzbare Durchgangsloch-Reparaturmethode mit Vorteilen wie Defektfreiheit, hoher Schweißeffizienz und hervorragender Oberflächengüte auf beiden Seiten der Schweißung. Im Rahmen der vorliegenden Arbeit wurden Prozessbedingungen ermittelt, mit denen sich defektfreie Schweißpunkte in allen untersuchten Materialen und Werkstückdimensionen erzeugen lassen. Die Region geringster Festigkeit wurde in allen Fällen außerhalb des Schweißpunktes gefunden, überwiegend in der wärmebeeinflussten Zone. Die Mikrostrukturanalyse der geschweißten Aluminiumlegierungen zeigt, dass die finalen mechanischen Eigenschaften im Wesentlichen durch die Entwicklung der festigkeitssteigernden Ausscheidungen während und nach dem Schweißen bestimmt wird. Signifikante Unterschiede bei den bearbeiteten Grundmaterialien als Reaktion auf den Schweißprozess lassen sich auf unterschiedliche Legierungszusammensetzungen und besonders auf die Ausprägung der vorliegenden Ausscheidungen zurückführen. Die fundamentale Prozessanalyse hat ergeben, dass bei ausscheidungshärtenden Aluminiumlegierungen die mechanischen Eigenschaften, die unter quasi-statischen Testbedingungen ermittelt werden, nicht ausreichen, um die Grundmaterialeigenschaften bei hohen Dehnraten und reibschweiß-typischen Temperaturzyklen abzubilden. Die

Legierungszusammensetzung, der Werkstoffzustand und die Merkmale der Ausscheidungsentwicklung unter den reibschweiß-typischen Temperaturzyklen bestimmen die Materialeigenschaften bei den getesteten Deformationsraten. Erst das durch die hier gezeigte fundamentale Prozessanalyse gewonnene Wissen ermöglicht eine schnelle Prozessoptimierung durch die geeignete Wahl von Prozessparametern für eine gegebene Legierung.

Contents

Symbols and Abbreviations

a	Distance from a cross-section to the ideal cross-section
AA	Aluminum alloy
Al	Aluminum
A-PFFSR	Active-passive filling friction stir repair
BM	Base metal
BT-FSW	Bobbin tool friction stir welding
Cu	Copper
DSC	Differential scanning calorimetry
d_P	Probe diameter
d_S	Sleeve diameter
d_s	Sleeve diameter
EDX	Energy dispersive X-ray spectroscopy
FFSW	Filling friction stir welding
FHPP	Friction hydro pillar processing
FPW	Friction plug welding
FSpW	Friction spot welding
FSSW	Friction stir spot welds
FSW	Friction stir welding
FTPW	Friction taper plug welding
GB	Grain boundary
GP	Guinier-Preston
HAZ	Heat-affected zone
HV	Vickers hardness
k	Yield stress of the deformed material in pure shear
Li	Lithium
LSW	Laser spot welding

l_p	Distance between protruding parts of material on the surface of RFSSW
L	Phase in the precipitation sequence of AlMgSiCu
m	Friction factor
M	Torque
Mg	Magnesium
n	Sample number
N	Final sample
p	Applied contact pressure
PD	Plunge depth of the sleeve
$Q_{applied}$	Applied energy / energy input
$Q_{equipment}$	Energy to overcome the frictional resistance in the welding equipment
Q_{total}	Total energy needed to perform the RFSSW process
Q, Q'	Phases in the precipitation sequence of AlMgSiCu
QC	Phase in the precipitation sequence of AlMgSiCu
QP	Phase in the precipitation sequence of AlMgSiCu
r	Radius
RFSSW	Refill friction stir spot welding
rpm	Tool rotational speed
RPP	Final retracted probe position
RSW	Resistance spot welding
RT	Room temperature
S	Phase in the precipitation sequence of AlMgZnCu
SEM	Scanning electron microscope
Si	Silicon
SRFSW	Self-refilling friction stir welding
SSSS	Supersaturated solid solution
SSuBT-FSW	Semi–stationary shoulder bobbin tool friction stir welding with a stationary upper shoulder

SZ	Stirred zone
T	Phase in the precipitation sequence of AlMgZnCu
$t_{process}$	Total time of the welding process
Δt	Sampling time
TMAZ	Thermo-mechanically affected zone
UTS	Ultimate tensile strength
w	True width of a circular feature in a cross-section
x_1, x_2	Corner points of a circular feature in a cross-section
x_n	Penetration depth
YS	Yield strength
Zn	Zinc

β', β''	Phases in the precipitation sequence of AlMgSiCu
σ	Normal stress
η, η'	Phases in the precipitation sequence of AlMgZnCu
θ	Rotation angle
$\theta, \theta', \theta''$	Phases in the precipitation sequence of AlCu
μ	Friction coefficient
τ	Shear stress
ω	Angular velocity

1 Introduction

The realization of the substantial environmental and human costs of extensive fossil fuel consumption is a unique characteristic of our society in the past few decades. Great parts of current research efforts strive to meet the increasingly stringent requirements for advanced technologies helping reduce the environmental footprint on a sustainable basis. A critical feature of successful technology development is the judicious selection of the best materials coupled with manufacturing techniques that take full advantage of their properties. Aluminum alloys are widely used in high fossil fuel-consuming industries such as transportation because of advantages including their high strength-to-weight ratio, high corrosion resistance and good workability [1, 2]. In particular, precipitation hardening aluminum alloys are commonly used in the technology leading aerospace industry, as the many available alloys and treatments enable the tailoring of a material's properties to specific requirements [3-6].

During service of aerospace aluminum components and structures, a wide range of defects can occur. Economic considerations have resulted in aircrafts operating well beyond their original design life bringing to the forefront issues of maintenance and repair [7]. Critical defects that often lack a satisfactory repair procedure are damage to through holes such as corrosion or crack initiation on costly aircraft engine parts. The cracking of aluminum panels in the aircraft fuselage is another commonly observed defect [8].

The search for a suitable keyhole repair technique for aluminum alloys has become a popular area of research because of the economic advantage of avoiding to replace defective parts and increasing the service life of aircraft components. Notable saving potential of life extension and scrap avoidance by repairing defect aircraft parts exists particularly for applications such as corrosion on complex thin-walled engine components that until now lack a satisfactory repair procedure. Currently, these parts are substituted by costly replacement parts instead of being repaired because a keyhole repair procedure that fulfills the requirements for high-quality repair welds is not available.

With advances in aerospace technology, the demand has increased for complex parts and components that must be produced using several processing methods. During the processing of aluminum alloys, various defects can occur as well, for example during welding operations. Examples include hot cracking and porosity in fusion welds or volumetric defects (i.e. voids, tunnel-defects, etc.) in solid-state processes such as friction stir welding (FSW). At the end of friction stir welds, the exit hole of the welding tool inevitably remains and reduces the weld strength because of the locally reduced joining area. This is particularly problematic in circumferential welds, in which runoff plates are challenging. Suitable keyhole repair procedures for aerospace aluminum components are needed not only in repair during service, but also for these manufacturing processes as manufacturing constitutes the biggest portion of the cost of the airframe and great effort is being spent to reduce the production costs and part count in current aircraft production [9].

As a repair procedure, conventional fusion welding is difficult to apply to aerospace aluminum alloys because of solidification cracking, porosity and major strength loss due to the high heat input in the weld region [10, 11]. In many cases, common defects such as hot cracking generate the need for undesirable dissimilar filler materials [12]. The requirements of gas shielding of the weld pool and

the removal of oxide layers before or during the welding process further complicate the procedure [13].

State-of-the-art solid-state friction-based welding processes have shown superior performance when welding conventionally difficult-to-weld aluminum alloys. The general advantages of friction welding processes are low heat input, absence of bulk melting, superior surface appearance, wide applicability, as well as energy efficiency and environmental friendliness. For linear welds, the well-developed FSW was successfully applied to a wide variety of metal structures [10]. In spot-like joints, the development of refill friction stir spot welding (RFSSW) is especially noteworthy, as when it was applied to join various similar and dissimilar light metals such as aluminum, it showed advantages over competing welding processes [14-16].

A number of friction-based welding processes have been applied recently to keyhole repair applications in aerospace aluminum alloys, as summarized in Chapter 3. However, the processes used are predominantly complex and multistage and require specially designed welding equipment. Furthermore, most of the reported processes are not suitable for sealing through holes and/or are limited in terms of keyhole and workpiece dimensions. The literature is also lacking application studies of keyhole repair in a wide range of high-strength aluminum alloys, such as the AlZnMgCu alloy AA 7075.

To meet the demand for a high-performing and versatile repair procedure, a keyhole repair process using RFSSW is introduced in this work that can seal through holes in a wide range of aluminum alloys with diverse workpiece thicknesses and hole diameters because of encouraging results obtained previously with this technology in conventional spot welding [17]. The developed repair procedure is designed to be as simple as possible, performing the repair weld in a single step without any additional pre- or post-welding work steps and is feasible using commercially available RFSSW equipment. Additionally, the process seals through holes using a similar filler to the parent material and aims to achieve excellent structural and metallurgical weld efficiencies. To develop a fundamental understanding of the repair procedure using RFSSW, the base material evolution imposed by the weld and the resulting properties, including the alloy-dependent differences, are analyzed in detail.

Friction welding was successfully applied in several variations to a variety of aluminum alloys. Most studies provide detailed, but often empirical information on how welding affects microstructure and properties. However, friction welding processes are complex, as they involve many phenomena, including the high frictional heat generation that, combined with large plastic deformations and thermal cycles with very high heating and cooling rates, constitutes the typical weld characteristics. Many phenomena occur simultaneously during the welding process that are influenced by the base material properties and weld process characteristics. Various microstructural evolution phenomena resulting in heterogeneous material properties in and around the weld are commonly reported. However, the literature is lacking a comprehensive analysis of the behavior of aluminum alloys under friction welding conditions as this affects the heat input and thus significantly influences the final mechanical properties.

Because of the large variety of possible repair applications including various types of aluminum base materials, a fundamental process analysis is performed. A knowledge-based approach to process analysis is chosen to study the behavior of the base material during high-shear-rate plastic deformation while exposing it to the typical thermal cycle associated with friction welding operations.

The influence of the base material composition and material properties on the energy input during friction welding as well as a comprehensive analysis of the friction condition and flow stress development is given. This approach addresses the knowledge gap of a general description of the base material behavior during friction welding operations in aluminum alloys. Additionally it is key to enabling a rapid process optimization by guiding the appropriate choice of processing parameters for a given alloy and to transfer the repair procedure to new alloys or base materials.

2 Objectives and structure

2.1 Objectives

The need for a suitable procedure to repair keyholes in aerospace aluminum alloys is evident as indicated in Chapter 1. Refill friction stir spot welding is an ideal candidate for such an application. Moreover, due to the large amount of possible applications of a suitable repair procedure, a methodology is needed that correlates the base material properties to the energy input during the weld process. The understanding of the underlying mechanisms are key to gain significant advantages in terms of weld process optimization and transferability to other alloys. Hence, the objectives of this study are as follows:

- Development of a keyhole repair process using RFSSW to achieve high-quality keyhole closure welds in structural aluminum alloys.
- Development of process parameter windows yielding defect-free welds for application-oriented workpiece thicknesses and keyhole diameters in the aerospace alloys AA 2219-T851, AA 6061-T6 and AA 7075-T651.
- Fundamental process analysis determining the characteristic features of keyhole repair welds using RFSSW.
- Analysis of the alloy-dependent interaction of process parameters, workpiece thickness and keyhole size with the thermal cycle and microstructural evolution leading to the resulting mechanical properties of the welds.
- Investigation of the influence of the base material properties on the friction condition, flow stress development and energy input during friction welding of the alloys of interest.
- Comparison of the base material's flow stress development to that under quasi-static testing conditions at similar temperatures to categorize the material behavior of friction welding operations.

2.2 Structure

This work is structured in the following order:

In Chapter 1 and 2, the current study is introduced and the objectives of the work are presented.

Chapter 3 gives a concise overview of relevant repair applications and aluminum alloys. The state of the art in friction-based keyhole repair processes and the level of development of conventional RFSSW is given in addition.

The experimental setup and procedure for the keyhole repair welds using RFSSW is described in Chapter 4. Additionally, the base materials are introduced, and the analytical techniques for material characterization are presented.

In Chapter 5, a fundamental process analysis determining the characteristic features of keyhole repair welds using RFSSW is shown. The weld forces and torque, the energy input, and the thermal cycle, as well as the joint formation characteristics and the general mechanical properties, are discussed.

In Chapter 6, the contribution of the microstructure of the welds such as the metallographic features and precipitate morphology to the final mechanical properties of the welds is shown. For this, the metallographic features and precipitate evolution during the weld are discussed in detail. The

mechanical properties are analyzed comprehensively and an alloy-specific discussion of the microstructure contribution to the weld properties is given. Finally, the key differences between the alloys of interest are presented in detail. Additionally, the variation in mechanical properties within the developed process parameter windows is analyzed and the influence of different process variants such as tool diameter to sheet thickness ratio is illustrated for AA 6061-T6 and AA 7075-T651 to characterize the repair procedure over a wider range.

In Chapter 7, frictional experiments are used to analyze the base material behavior during high-shear-rate plastic deformation. The friction condition, flow stress development and energy input are discussed considering the boundary conditions typically seen for RFSSW. Furthermore, the influence of incipient melting, strain rate-dependent overstress and precipitate evolution on the observed flow stresses is analyzed. The conclusions are transferred to the repair process using RFSSW to explain energy input and temperature observations made in the previous chapters.

Chapter 8 summarizes the main conclusions of this study.

3 State of the art

A concise overview of relevant repair applications in aluminum alloys, the state of the art in friction based keyhole repair processes and of the level of development of conventional RFSSW is given in this chapter.

3.1 Relevant applications and representative base materials

A recent trend in the transportation industry is to improve customer value through creation of products that incorporate high-performance structural materials and advanced manufacturing technologies. The objective is to improving performance, reducing ownership costs, extending the service life and reducing environmental impact. Due to the increased number of product requirements and the greater range of structural materials available, the manufacturers are faced with complex choices for selecting a material to meet the requirements for a particular system. Lightweight construction has become a universal requirement for all transportation products; especially in the aerospace sector. The complexity of current design and manufacturing methods additionally requires structural materials to satisfy a much wider variety of properties such as strength, damage tolerance and corrosion resistance. [7]

Aluminum alloys are widely used in transportation sectors and particularly in the aerospace industry because of advantages including their high strength-to-weight ratio, high corrosion resistance and good workability [1, 2]. In particular, precipitation hardening aluminum alloys remain to be commonly used, as the many available alloys and treatments enable the tailoring of a material's properties to specific requirements [3-6].

Over the last several decades, global demand for aluminum has been increasing, and it is now the second most widely used metal after steel [18] and one third is used in the transportation industry [19]. A long term growth of the transportation sector is expected [20] in accordance with the expected global growth of population as reported by Cheah et al. [18] exemplary for the passenger vehicle stock in the United States.

Economic considerations have resulted in current aircraft operating well beyond their original design life bringing to the forefront issues of maintenance procedures, among corrosion resistance and fatigue behavior [7]. A major issue is damage on through holes because of corrosion on housing parts of aircraft engines made of aluminum alloys as shown in Figure 3.1.

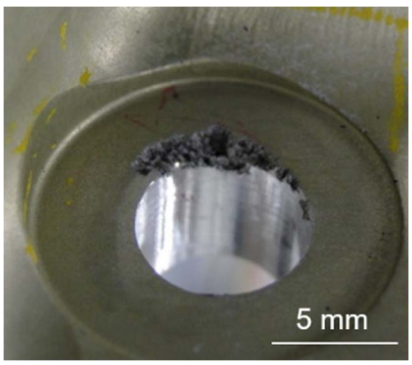

Figure 3.1 Corrosion on a through hole in an aircraft part made of aluminum.

A repair procedure that is capable of sealing through holes in aluminum alloys could as well improve the commonly performed patch repair in which often introduces dissimilar patch materials to aircraft structural panels [8].

Friction stir welding has shown superior capabilities when welding lightweight materials such as aluminum. The BT-FSW process variant is particularly suitable for closed structures such as pipes or hollow structures. A major drawback is the remaining exit hole at the end of the weld resulting from the extraction of the welding tool. Figure 3.2 shows a typical exit hole left by the BT-FSW process. A process dealing with this issue has to be chosen when employing the technique in industrial products. In some applications, the question of the keyhole closure can be avoided by creating a runoff plate that can be removed after the welding. Due to the lower shoulder connected to the probe, this is not possible when circumferential welding hollow structures with BT–FSW.

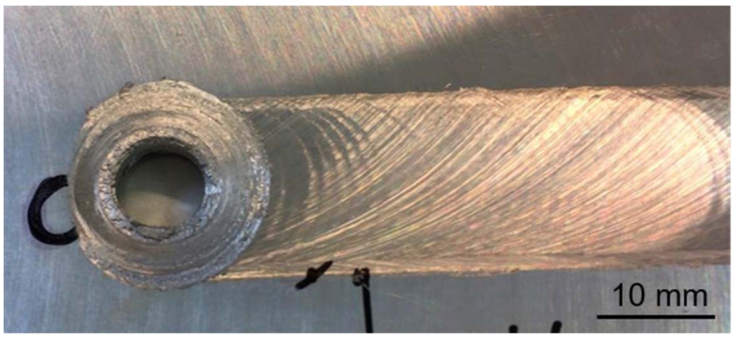

Figure 3.2 Exit hole at the end of the BT-FSW process resulting from the extraction of the welding tool.

The aerospace industry uses a wide variety of precipitation hardening aluminum alloys to produce parts in which the discussed repair applications occur. The 2xxx series alloys are based on the addition of Cu as the main alloying element and small amounts of several other elements and were the first precipitation hardening alloys to be discovered around 1910 [21]. AA 2219 is considered a promising structural material for use in the aerospace industry owing to its high strength-to-weight ratio, good fracture toughness and excellent stress-corrosion resistance [22]. Because of its admirable cryogenic properties, it is widely used for the fabrication of liquid propellant storage tanks for space structures, such as the fuel tanks of Saturn V S-IC, the Polar Satellite Launch Vehicle and Ariane 5 [5, 23, 24].

Alloys with Mg and Si as the main alloying elements, classed as the 6xxx series, are known to exhibit lower levels of alloying additions than other age hardening alloys. They have low to medium strength and are much more hot and cold workable [21]. AA 6061 is commonly used in automobile parts such as wheels or structural components and in aerospace structural components such as wings and fuselages [6]. Application prospects in the automotive industry led to extensive studies on the 6xxx series alloys around the year 2000. The aging response of AlMgSiCu alloys was found to be complex owing to the presence of many intermediate phases [25].

The 7xxx series AlZnMg(Cu) alloys are noted for including the highest strength aluminum alloys [21]. Alloys like AA 7075 have been widely used for aeronautical applications because of their desirable specific mechanical properties [3, 4].

The basic metallurgical concepts for maximizing properties of precipitation hardening aluminum alloys are well known. The desirable mechanical properties of this class of alloys are due to the formation of precipitates at the nanometric scale. This contributes to the strengthening of the alloy, as the strength is controlled by the obstruction of moving dislocations by precipitations. Precipitation processes occur because the solid solubility of certain alloying elements decreases with decreasing temperature.

Strengthening particles are formed during the decomposition process of the supersaturated solid solution (SSSS) towards an equilibrium state. The SSSS is obtained by heating the alloy to a temperature high enough to dissolve the minority components, followed by quenching to a lower temperature. This rapid cooling suppresses the nucleation of secondary phases so that the alloy exists at a lower temperature in an unstable supersaturated state after the solution heat treatment. If the alloy ages at temperatures within a certain alloy-specific interval, the secondary phases precipitate from the aluminum matrix by diffusion-driven nucleation and growth processes. After quenching, the SSSS allows the clustering and precipitation of phases to compensate for the unstable condition. At RT, this process is called natural aging. To bring the microstructure to a preferred, more stable condition, the alloy is exposed to moderate temperatures.

Precipitation is a complex process that may include several simultaneous reactions depending on the aging conditions and pretreatments. Typically, in the first cluster, Guinier-Preston (GP) zones and intermediate precipitates are formed before the equilibrium phase occurs. GP zones are ordered, solute-rich groups of atoms that might be only one or two atom planes in thickness. The intermediate precipitates are typically much larger in size than the GP zones and only partially coherent with the matrix. Normally, the formation of the final equilibrium precipitate involves complete loss of the coherency. It forms only at relatively high aging temperatures and has little hardening effects because it is typically coarsely dispersed. [26-28]

3.2 Friction-based keyhole repair processes

The need for a suitable keyhole repair process for high-strength aluminum alloys is evidenced by the variety of studies published recently in this research field. Several processes were employed, but other than the work published by the author [29-31], no further studies regarding keyhole repair using RFSSW have been conducted by other research groups.

In friction taper plug welding (FTPW, or friction plug welding, FPW), a tapered plug is forced co-axially into a keyhole with a similar taper, Figure 3.3. The conical surface of the plug is friction welded to the surface of the hole. In this method, post-machining is necessary on both sides of the workpiece to remove the unconsumed portions of the plug and the material that is extruded from the plate. Du et al. [32] used FPW to seal the through holes in AA 2219-T87 plates with a 10 mm thickness and found FPW to be feasible only in tapered through holes, not in standard through holes. The inclinations of the tapered hole and plug must be compatible to ensure that the typical defects in the lower portions of the weld are extruded from the plate. The maximum tensile strength of the friction plug welds was 72.3 % of the base metal (BM) strength with the thermo-mechanically affected zone (TMAZ) located close to the bonding interface, noted as the weakest location of the joints. Metz et al. [33] applied FPW in friction stir-welded AA 2195-T8 aluminum-copper-lithium alloy plates with a 6.36 mm thickness. The major plug diameter was 33 mm, and the minor diameter was 15.9 mm. The weakest area was measured near the plug weld interface, with 65 % of the BM hardness. In a different study, Metz and Barkey [34] found the strength of the same plug welded

samples to be 57 % of the BM strength compared with 68 % of the BM strength in friction stir-welded samples.

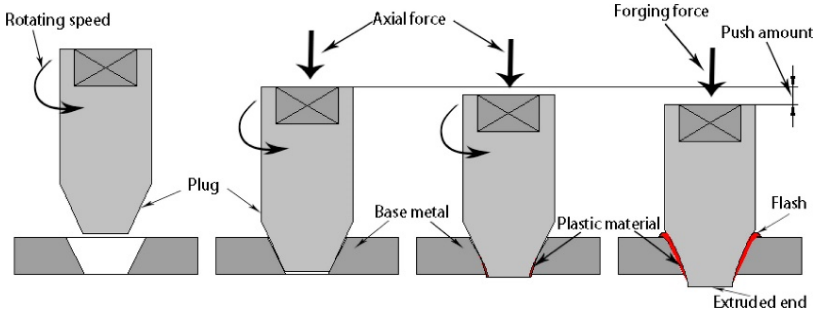

Figure 3.3 Schematic illustration of the FPW process. Reprinted from [32], with permission from Elsevier.

Filling friction stir welding (FFSW), as presented by Huang et al. [35], is derived from the plug welding process. A shoulder portion is added to the tapered plug to avoid stress concentration at the interface between the plug and hole. Huang et al. [35] sealed the exit holes with a diameter of 9.8 mm left by FSW using FFSW in Al-Cu-Mg alloy plates with a thickness of 7.8 mm. Additionally, friction stir processing was used to reprocess the sealed keyholes with a rotating non-consumable tool consisting of only a steel shoulder without a probe. The keyhole closure welds reached a tensile strength of 84.3 % of the base welds conducted by FSW. Han et al. [36] used the same approach of filling a keyhole left by FSW with FFSW and subsequently using friction stir processing as a post-weld processing step. Han et al. used a plug with a diameter of 10 mm made of AA 7075-T6 to seal keyholes in an AA 2219-T6 plate with a thickness of 7.8 mm and achieved 96.6 % of the FSW base weld strength. Behmand et al. [13] applied FFSW to remove a 6.5 mm-deep exit hole from friction stir-welded lap joints in AA 5456. The failure load on the coupons with the refilled keyhole reached 91 % of the corresponding defect-free FSW joint.

Zhang et al. [37] modified the FFSW method using a pin-free tool and a T-shaped filler bit to reduce the setup time for replacing the tool between the filling and reprocessing operations. Zhang and colleagues sealed keyholes left by FSW in AA 1060 sheets with a 4.7 mm thickness. To eliminate voids in the lower portion of the weld, Zn braze foil was pre-placed in the keyhole. The ultimate tensile strength of the keyhole closure welds reached 67.3 % of the BM strength. Until now, FFSW has been proven to seal only keyholes left by a conical FSW tool, for which the geometry of the filler bit must be adapted, and has not yet been applied to through holes.

Recently, a method called active-passive filling friction stir repair (A-PFFSR) was introduced by Ji et al. [38] in AZ31B magnesium alloy as schematically shown in Figure 3.4. A-PFFSR is a multistage process that uses different filler bits and non-consumable pinless tools. First, two active filling steps are applied to reshape the keyhole left by FSW. Next, passive filling is performed using a disc-shaped filler material. The filling material is heated by frictional heat generated by the pinless tool. Additionally, the forging force created by the tool is beneficial to creating a bond between the filling material and the surrounding workpiece. To achieve sound surface formation, the rotating tool must move transversally along the base friction stir weld after the dwelling period. Later, the same authors applied the technique to 7N01-T4 aluminum alloy sheets with a 4 mm thickness [39]. A-PFFSR was

used to seal keyholes left by the FSW process, reaching 82.1 % of the tensile strength of the FSW base welds and 69.9 % of the BM tensile strength.

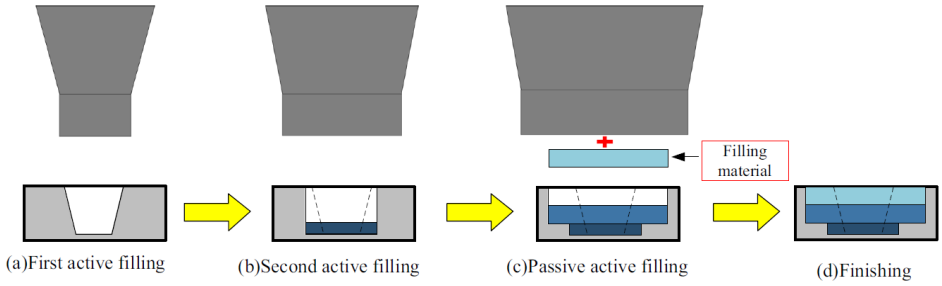

Figure 3.4 Schematic illustration of the A-PFFSR process. Reprinted from [39], with permission from Elsevier.

Recently, Chen et al. [40] introduced the method of refilling the exit hole of friction stir spot welds (FSSW) or friction stir welds using the same tool in an additional processing step. For this, the rotating tool penetrates the workpiece in a position close to the exit hole with a smaller penetration depth and travels along a circular path surrounding the keyhole, Figure 3.5. This refills the original keyhole and creates a new but smaller keyhole at a different exit location, Figure 3.6. However, this method accounts for the volume difference between the old and new exit hole by reducing the workpiece thickness in the region of the repair weld because no filler material is used; compare with Figure 3.6 (b). Additionally, this “keyhole refilled friction stir spot welding” process is not suitable for through-hole repair, and as a thickness reduction and a keyhole remain, it is considered unsuitable for high-performance applications.

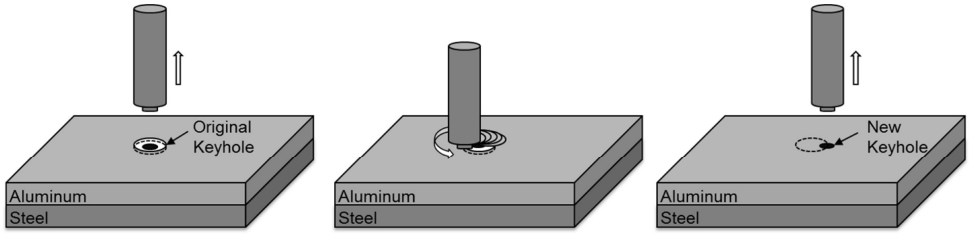

Figure 3.5 Schematic illustration of the keyhole refilled friction stir spot welding process. Reprinted from [40], with permission from Elsevier.

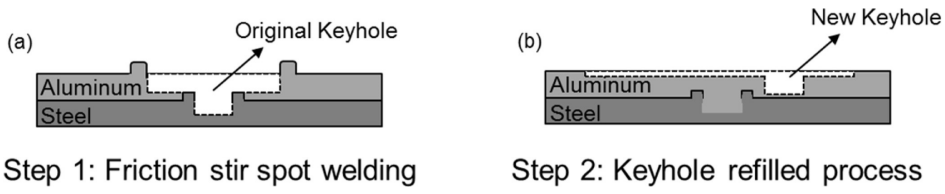

Figure 3.6 Schematic illustration of the cross-section of the keyhole refilled friction stir spot welding process. Reprinted from [40], with permission from Elsevier.

Self-refilling friction stir welding (SRFSW) was proposed by Zhou et al. [41] to seal the keyhole left by FSW in stainless steel. This multistage process uses a series of non-consumable tools with gradual

changes in pin geometry and size. As the keyhole is merely reshaped, a wide and shallow exit hole remains at the surface because of the lack of filler material. Sajed [42] used the same approach but employed only one refilling step, naming the procedure “two-stage refilled friction stir spot welding”. The double-acting friction stir spot welding tool and keyhole filling process employed by Uematsu et al. [43] follows the same approach. Similar to other processes that do not use filler material, the disadvantage of the workpiece thickness reduction remains. Additionally, SRFSW is not applicable to through holes.

Additional processes that are not discussed in detail are friction hydro pillar processing (FHPP), which was successfully applied to refill keyholes in steel but is not applicable to aluminum alloys [44], and the modified friction stir spot welding processes employed by Prakash and Muthukumaran [45] and Venukumar et al. [46]. All these processes cannot be applied as a universal keyhole repair process.

3.3 Conventional refill friction stir spot welding

The RFSSW process was developed and patented by Helmholtz-Zentrum Geesthacht GmbH [47] primarily to replace rivets and resistance spot welds in lightweight structures. In the early stages, the process was also called friction spot welding (FSpW). Since its development, conventional RFSSW was successfully applied to weld a wide variety of similar and dissimilar metal components in an overlapping configuration. The range of processed material combinations including aluminum encompasses configurations such as similar aluminum [48-50], dissimilar aluminum [51], aluminum to magnesium [52], aluminum to copper [53], aluminum to steel [54] and aluminum to titanium [55].

Conventional RFSSW joining two sheets of base material uses a non-consumable tool consisting of three independent movable parts: a stationary clamping ring and two rotating parts – the sleeve and the probe. The conventional RFSSW process is presented in Figure 3.7.

The weld process can be separated into four distinct stages. First, the clamping ring is pressed on the surface of the upper sheet, fastening the base material sheets for the rest of the process. Then, the rotating sleeve moves downwards, and the rotating probe moves upwards, displacing the plasticized workpiece material into the cavity under the retracting probe. After a predetermined plunge depth is reached, both the sleeve and probe move back to the initial surface of the upper sheet, pressing the plasticized material back into the weld. Finally, the tool is retracted, leaving the upper and lower sheet joined without a keyhole on the surface of the upper sheet. The RFSSW process can also be performed by plunging the probe downwards into the workpiece as the sleeve is retracted. This probe plunge mode is not commonly used because of the reduced joining area, which is associated with a decrease in weld strength. A detailed process explanation is given in Chapter 4.1.1 and 5.1, as the studied keyhole repair process is based on the same process as conventional RFSSW.

For dissimilar welds of light metal and a high melting point material such as steel or titanium, the light metal component is preferentially used as upper welding partner, as mostly tools made of steel are used. In this case, the tool plunge depth is pre-set so that the tool does not penetrate into the lower sheet but instead applies force and generates heat within the upper light metal sheet. If both of the welding partners are light metals, then the tool can be plunged into the lower sheet as well, thereby completely stirring the interface.

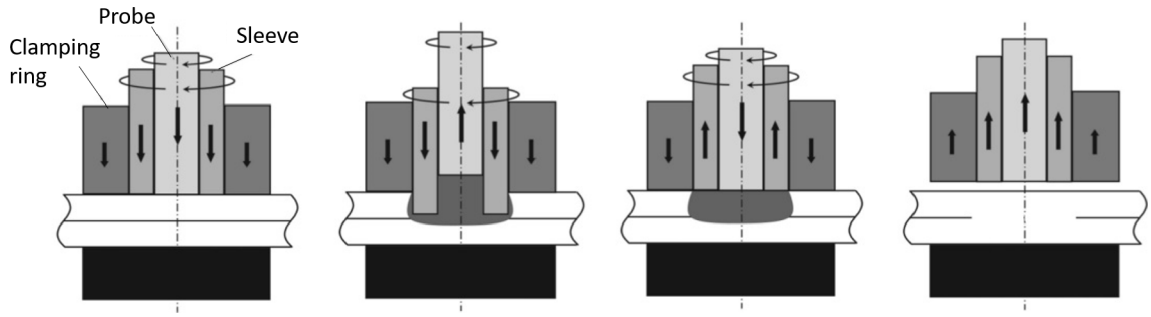

Figure 3.7 Schematic illustration of the RFSSW process. Adapted from [52], with permission from Elsevier.

The main characteristic of RFSSW is the solid-state nature of the process. During the weld, less energy is introduced into the welded workpiece than in fusion welding processes, and no bulk melting, as well as low residual stress and low distortion, occurs. This transfers the advantages of solid-state welding technologies, such as the absence of defects associated with conventional fusion welding techniques, e.g., pores and hot cracks. Additionally, the lower energy input of solid-state processes enables the realization of higher weld efficiencies in workpieces in which microstructural evolution caused by thermal cycle exposure decreases the strength, such as in precipitation hardening aluminum alloys. In contrast to typically used fusion welding processes such as resistance spot welding (RSW) and laser spot welding (LSW), friction-based welding processes are not limited by the presence of an oxide layer on the surface of an aluminum workpiece. In fusion welding, higher thermal energies are required to break up the oxide layer to melt down the substrate; this can induce the evaporation of alloy elements, leading to property degradation [49]. The general advantages of friction-based solid-state welding processes are thoroughly summarized by Mishra and Ma [10] for FSW.

The RFSSW process is known to produce a superior surface appearance (without keyholes or larger weld seams), which results in improved mechanical behavior and eliminates the need for additional surface treatment. The absence of a keyhole is the main advantage of RFSSW over other spot-like friction welding processes, such as the friction stir spot welding process.

When overlapping sheets of similar aluminum alloys are welded using RFSSW, different characteristic microstructural weld zones occur, Figure 3.8. These zones called stirred zone (SZ), thermo-mechanically affected zone (TMAZ), heat-affected zone (HAZ) and base material (BM), typically occur during friction welding processes in precipitation hardening aluminum alloys. For a detailed description of the microstructural zones, refer to Chapter 6.1, as the weld zone formation in this study is similar to that in conventional RFSSW. When two sheets are conventionally welded in a lap joint configuration, typical geometric and metallurgical patterns occur, such as hooking, partial bonding and bonding ligament [56]. The hook is a geometrical flaw formed by upward bending of the sheet interface during the RFSSW process. The hook, partial bonding and bonding ligament features are defined as the oxide layer that was not completely destroyed, and their formation is associated with the material flow during welding imposed by tool movement [57].

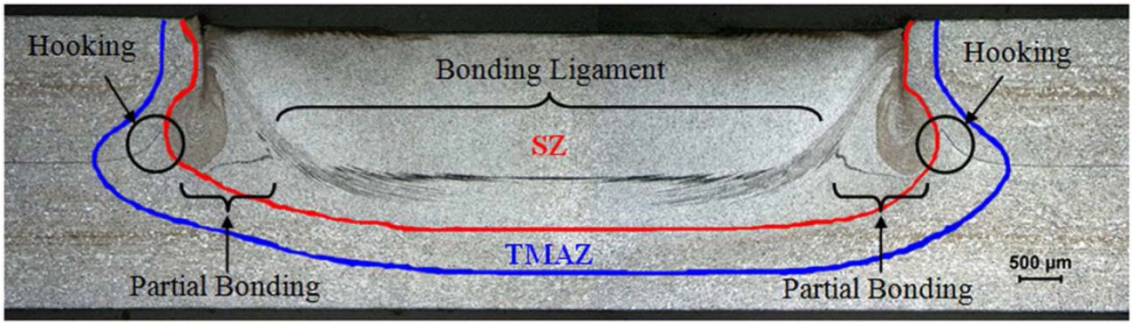

Figure 3.8 Typical weld zone and interface features in similar AA 6181-T4 conventional RFSSW. Reprinted from [56], with permission from John Wiley and Sons.

Most studies have shown that the RFSSW process can produce welds with good mechanical behavior in terms of strength and reproducibility when appropriate processing parameters and tool configurations are employed. Numerous studies evaluating the mechanical properties and interface features of joints welded by conventional RFSSW are currently available in the literature.

Allen and Arbegast [58] summarized that the lap shear strength of similar RFSSW aluminum joints approaches the strength range requirements of riveting and resistance spot welding. In contrast to the friction stir spot welding process, a large effective shear area was found along the interface between the upper and lower sheets. Most available studies evaluate the influence of process parameter and boundary conditions such as tool rotational speed, tool plunge depth or tool design on the properties of the joint [15, 48-50, 57, 59, 60].

In conventional RFSSW, the initial interface that has to be welded is located horizontally between the upper and lower sheet. Research interest is drawn to this joined interface, as fracture in lap shear loading mostly initiates in the highly stressed area where the weld cuts through the interface between the sheets. The deformation of the sheet interface on the sides of the joint, called hooking, is a common feature in conventional welds; compare description above and Figure 3.8. The hook geometry plays an important role in determining the fracture mechanism. If the hook geometry becomes too sharp because of inadequate process parameter settings, cracks initiate in the hook and grow under low levels of loading [15, 56]. The welded interface in the peripheral regions of the stirred zone (SZ) – as discussed in Chapter 5.3.1 – exists in conventional RFSSW, similar to the keyhole repair application developed in this work. Nevertheless, analysis of conventional RFSSW focuses on the interface between the upper and lower sheets because of the crack initiation in this region.

Under lap shear or cross-tension loading, various fracture modes occur in similar welds of aluminum alloys, such as nugget debonding and plug-type fracture on the upper and lower sheets, Figure 3.9. The fracture modes often have different names; for example, the nugget debonding fracture type is also called shear fracture [60] or fracture through weld [57]. In addition to the hook geometry, the effect of partial bonding is generally found to play an important role in the fracture type and final mechanical properties because both features act as crack initiation and propagation sites [57].

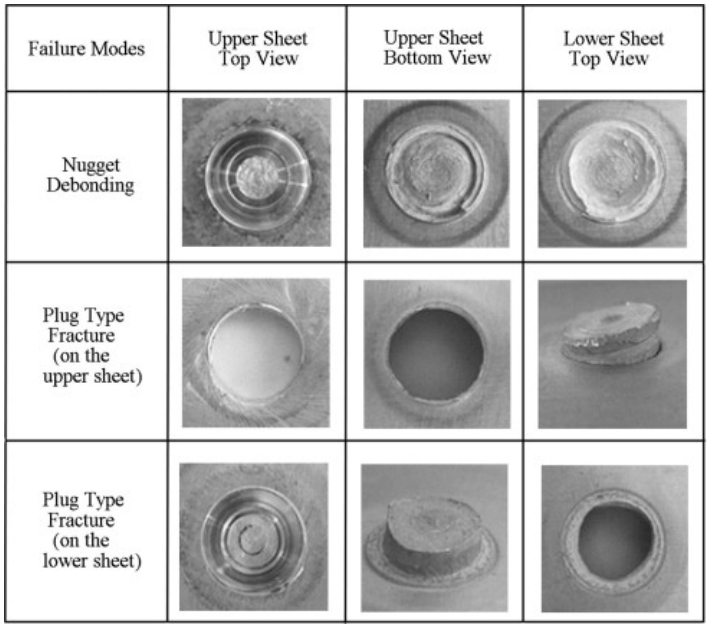

Figure 3.9 Macroscopic fracture appearance of RFSSW joints under cross-tension loading. Reprinted from [14], with permission from Elsevier.

Research regarding the joining of dissimilar metals using conventional RFSSW has focused on the formation of brittle intermetallic compounds [57]. Conventional RFSSW was found to limit the undesirable formation of intermetallic compounds, for example, in the Al-Ti-system, which is considered difficult to weld using fusion welding methods [61].

The RFSSW process is well known to produce solid-state welds in an overlap joint configuration in a wide range of lightweight alloys, including aluminum alloys that are usually associated with weldability problems when using conventional techniques. In this conventional application, RFSSW has been used to weld the precipitation hardening aluminum alloys of interest: AA 6061 [60, 62, 63] and AA 7075 [14, 64-66]. AA 2219 has not been welded using RFSSW but was successfully processed by other friction-based processes, such as FSW [67, 68], FPW [32, 69] and friction stir processing [70].

The high-strength AlZnMgCu alloy AA 7075 is generally considered highly complicated to weld with conventional fusion welding techniques [71]. Most studies found that the material was difficult to weld using RFSSW, as defects would form in the weld zone, such as voids, incomplete refill and lack of mixing, especially at higher plunge depths of greater than 2 mm [14]. To avoid the formation of defects, the formation of a remaining surface undercut with a depth of 0.2 mm was accepted by some authors [66]. In comparison, the AlMgSiCu alloy AA 6061 was successfully welded by different authors, both in peak-aged [63] and naturally aged [60] conditions.

4 Experimental procedure and materials

In this chapter, a concise overview of the welding procedure and equipment and of the materials and analytical techniques used in this work is given.

4.1 Welding procedure

4.1.1 Keyhole repair process using RFSSW

In this work, a procedure was developed to seal through holes such as the termination holes of FSW processes, drilled-out defects or damage to holes in aluminum structures. The developed keyhole repair method seals through holes by applying a plug as a filler material into a through hole in an aluminum workpiece, and the RFSSW process is used to weld the plug to the surrounding workpiece.

The repair process using RFSSW employs the same non-consumable tool as conventional RFSSW consisting of three independent movable parts: a stationary clamping ring and two rotating parts, the sleeve and the probe. The principles of the keyhole repair process are presented in Figure 4.1.

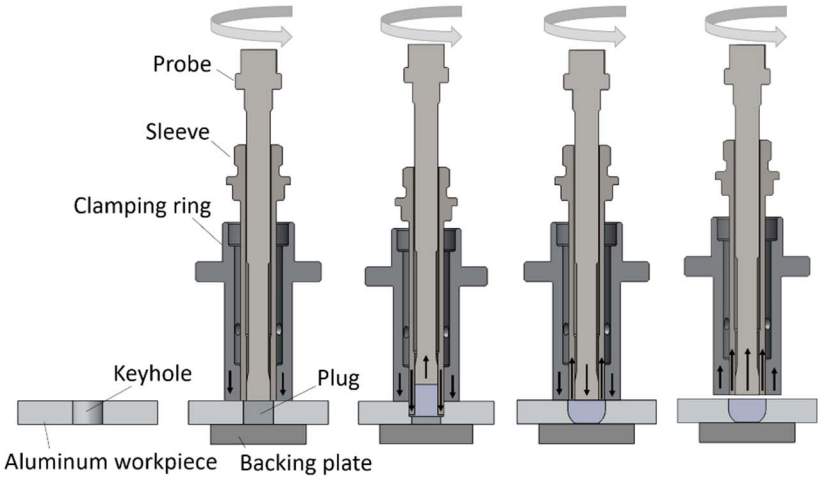

Figure 4.1 Illustration of the keyhole repair process using RFSSW with a cross-sectional view through the tool and welded specimen.

The repair process starts with moving the clamping ring downwards to clamp the workpiece. The sleeve and probe start to rotate in the same direction at a pre-set speed. The sleeve plunges downwards into the workpiece while simultaneously retracting the probe. The rotating sleeve generates frictional heat, thereby plasticizing the workpiece material, and the downward movement of the sleeve forces the softened material into the cavity left by the probe. The sleeve diameter is larger than the diameter of the plug that has previously been inserted into the keyhole. Thus, the interface between the plug and surrounding workpiece is completely stirred by the sleeve. When a predetermined plunge depth is reached, the rotating probe and the sleeve interchange their direction of movement. The sleeve moves upwards towards the initial position, and the probe moves downwards, pushing the material back into the joint to refill the hole left by the retracting sleeve. Metallic bonding is created at the interface between the refilling plasticized material and the surrounding workpiece. Finally, the tool

is retracted from the surface to leave the initial plug and surrounding workpiece completely joined. The welding procedure, including the individual tool part movement during the repair process, is discussed in detail in Chapter 5.1.

The keyhole repair welds using RFSSW were performed with custom-built equipment designed and constructed to investigate the RFSSW process, Figure 4.2. The axial and rotational movement of the tool parts is actuated by individual electromechanical transducers. Plunge depth as well as rotational and axial speed was controlled using the response value from the position control system in the drive amplifier in 10 ms steps. The axial load of the probe and sleeve is measured using four identical load cells each, whereas the axial load of the clamping ring was measured using three load cells. The torque of the sleeve and probe is measured using load sensors attached to the respective motors via lever arms. The motors are float-mounted; thus, the engine torque is transferred to the load cells. The load cells used were customized to the corresponding measurement range. The measurements were coupled with a data acquisition system so that the force, torque and position values were recorded simultaneously during each spot welding operation. To display the sleeve and probe torque and force, a moving average of 3 measurement values was calculated.

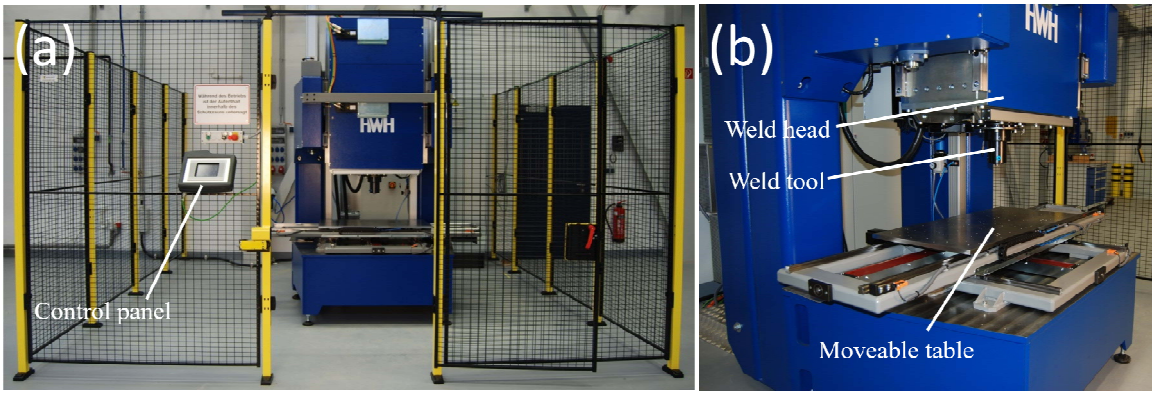

Figure 4.2 Welding equipment used in this study: (a) overview of the welding equipment with the control panel in a safety fence and (b) close-up view of the weld operational area.

RFSSW tools made of molybdenum-vanadium alloyed hot-work tool steel were used. A threaded probe and sleeve were used, as this is known to improve material flow and to avoid the formation of voids [15]. To seal different sizes of through holes, three different sized tools were developed; see Figure 4.3. The small tool features a 4 mm probe, a 6 mm sleeve and a 12 mm clamping ring diameter, while the respective diameters of the medium tool are 6 mm for the probe, 9 mm for the sleeve and 17 mm for the clamping ring. The large tool features probe, sleeve and clamping ring diameters of 8 mm, 12 mm and 20 mm, respectively.

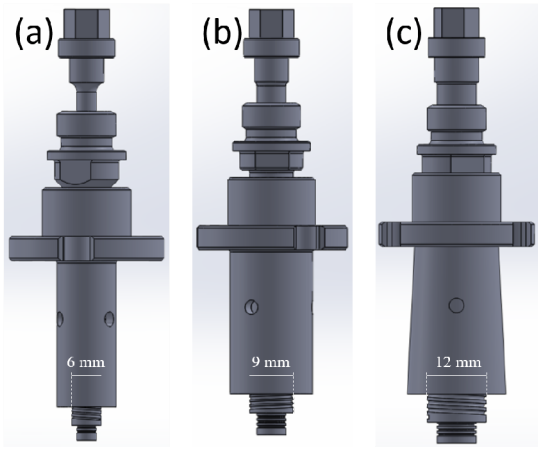

Figure 4.3 Illustration of the tools used in this study: (a) small tool, (b) medium tool and (c) large tool.

4.1.2 Experimental procedure

To apply the keyhole closure process discussed above, through holes were drilled in the BM, Figure 4.4 (a). Cylindrical plugs of the same material and identical dimensions were inserted manually into the holes, Figure 4.4 (b), and the repair weld using RFSSW was performed to join the plug and the surrounding workpiece, Figure 4.4 (c). The hole and plug were manufactured using the transition tolerance H7/j6, allowing manual insertion of the plug. The workpiece was processed in the as-welded condition without any surface treatment before or after the welding process.

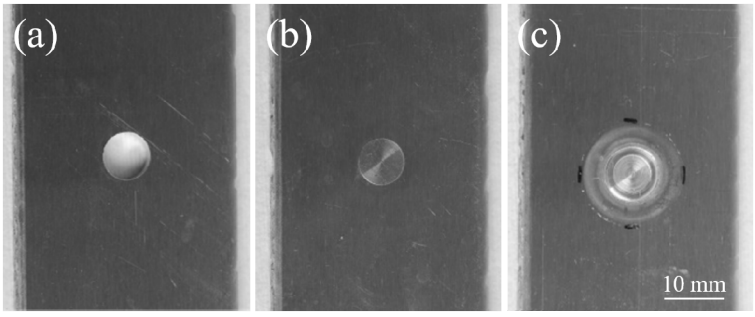

Figure 4.4 Detailed images of welded coupons featuring a keyhole (a), a keyhole filled by a plug (b) and a typical upper surface after the repair weld using RFSSW.

To analyze the influence of through holes corresponding to different plug diameters on the properties of the welds, application-oriented keyhole diameters of 5, 7.5 and 10 mm were employed in this study. As the developed repair procedure is intended to stir the interface of the plug and surrounding workpiece, the tool diameter was adapted to the keyhole/plug diameter so that the front surface of the sleeve concentrically contacts the interface during the sleeve plunge stage of the process. Table 4.1 summarizes the keyhole diameters and associated tool sizes.

Table 4.1 Summary of keyhole sizes and associated tool sizes used in this study to weld 3 and 6 mm thick sheets of the alloys of interest.

Keyhole and plug diameter (mm)	Tool size	Probe diameter (mm)	Sleeve diameter (mm)	Clamping ring diameter (mm)
5	Small	4	6	12
7.5	Medium	6	9	17
10	Large	8	12	20

The keyhole closure process was performed in the center of rectangular coupons as shown in Figure 4.5. For further analysis, the welded coupons were cross-sectioned or machined according to the description in the following chapters. Material being pressed out from the weld zone was observed if the welded sample was too narrow compared to the tool used. The size of the welded coupon was varied according to the plug and tool size used to avoid this occurrence.

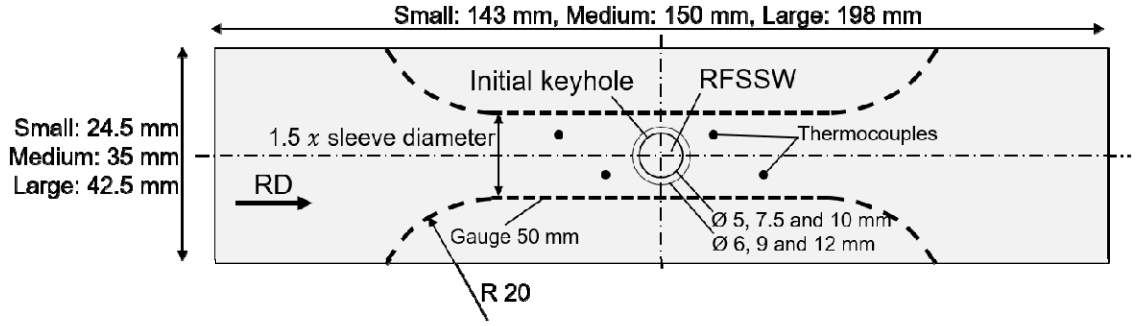

Figure 4.5 RFSSW welded coupons, adapted from [30].

To avoid lack of refill, as reported by Shen et al. [14] for higher plunge depths, the cavities between the tool parts should be filled with aluminum before the actual repair welding is performed. This is achieved by plunging into the BM with a plunge depth that is significantly higher than the repair weld plunging depth. This process causes aluminum intrusion into the tool and impedes additional material flow into the tool during the actual repair welds. Additionally, during keyhole closure, this effect can be avoided by using a plug with a height slightly larger than that of the surrounding workpiece.

The welded coupons were quenched in water at room temperature (RT) at 4 to 5 s after the repair process to avoid microstructural evolution during the cooling phase. Following the weld process, the coupons were stored at RT to allow post-weld natural aging. The results labeled “as-welded” in the following chapters were measured at approximately 1.5 to 2 h after welding.

4.1.3 Welding parameters

The main welding parameters evaluated in this study were the rotational speed, plunge speed and retract speed of the sleeve. The weld procedure used in this work is summarized in Table 4.2. In this study, the RFSSW process was conducted in position control mode. The clamping ring moves to a predefined position on the surface of the workpiece, and the welding operation is performed by monitoring and controlling the positions of the individual tool parts according to the weld procedure.

The weld procedure starts with the clamping ring reaching the pre-set clamping force. Tool position 0 describes the surface of the welded workpiece, whereas positive values of the tool position describe

the direction downwards into the workpiece, as shown in Chapter 5.1. The individual steps of the weld procedure describe the time to reach the desired values of rotational speed and position of the tool parts.

In the initial step, the rotational speed of the sleeve and probe is initiated, and the tool parts are retracted to avoid any premature contact to the workpiece. The rotational speeds of the sleeve and probe are similar; thus, no relative movement exists between them in a rotational sense. The first step of the weld procedure accelerates the sleeve and probe to reach the desired rotational speed of the welding process, and in the second step, the tool parts approach the surface of the sheet while maintaining the rotational speed. As described above, the third step is the sleeve plunge phase. The plunge depth PD, which depends on the sheet thickness used, has to be adjusted so that a certain gap remains between the sleeve and the backing structure to avoid contact. To ensure complete stirring of the interface between the plug and surrounding workpiece, the gap has to be adjusted to be as small as possible. Employing a gap distance similar to or smaller than the amount of workpiece material recrystallizing in direct contact with the sleeve front surface as discussed in Chapter 5.3 is advisable.

The time set for this process is calculated using the PD and the desired plunge speed of the sleeve. To maintain a constant volume, the cavity underneath the probe must occupy the same volume as that pushed away by the plunging sleeve. The probe must retract further than the sleeve plunges because the front surface of the sleeve is larger than that of the probe for the tools used in this study. The final retracted probe position RPP for the sleeve plunge step in mm is calculated according to:

$$RPP = -\left(\left(\frac{d_S}{d_P}\right) - 1\right) * PD \tag{1}$$

where d_S is the sleeve diameter, d_P is the probe diameter and PD is the plunge depth of the sleeve. Most welding equipment will calculate the retracted probe position automatically according to a position controlled welding procedure. In the fourth step of the process, the sleeve is retracted, and the probe is pushed downwards to the surface of the workpiece. During the fifth and final step, both tool parts retract 1 mm from the surface of the workpiece, and the rotational speed is reduced.

Table 4.2 Weld procedure for keyhole closure using RFSSW.

Step	Time (s)	Sleeve		Probe	
		Position (mm)	rpm	Position (mm)	rpm
Initial	-	-1	500	-1	500
1	0.5	-1	weld rpm	-1	weld rpm
2	1	0	weld rpm	0	weld rpm
3	PD / plunge speed	PD	weld rpm	RPP	weld rpm
4	PD / retract speed	0	weld rpm	0	weld rpm
5	0.5	-1	500	-1	500

To demonstrate certain correlations, the sleeve revolutions per mm plunge and retract are calculated using the sleeve plunge and retract speed and the tool rotational speed. This parameter is similar to the weld pitch ratio known from FSW [72] and is introduced for RFSSW in this study.

Experimental design

To characterize the keyhole repair welds using RFSSW, the three alloys of interest were processed using various tool sizes, process parameters and sheet thicknesses. In this section, an overview of the conducted experiments is given.

A process parameter window yielding defect-free welds was developed for each alloy of interest, Table 4.3. Welding employing process parameter combinations outside of the given window results in weld defects such as voids or incomplete refill. The influence of the process parameters, the sheet thickness and the tool size was analyzed within the respective process parameter window. When the small and large tool, which are in an early stage of development, are employed, process parameters with generally lower rotational speeds and sleeve plunge and retract speeds were chosen from the respective process parameter window to prevent tool failure.

Table 4.3 Process parameter window yielding defect-free welds in the alloys of interest.

	Process parameter window		
	Clamping force (small, medium and large tool)	**Rotational speed (rpm)**	**Sleeve plunge and retract speeds (mm/s)**
AA 6061-T6	4 kN, 7 kN, and 12 kN	1650 to 3050	0.625 to 1.125
AA7075-T651	7 kN, 9 kN and 15 kN	1375 to 2224	0.64 to 1.106
AA 2219-T851	7kN (medium tool)	1200 to 1500	0.6 to 1

For AA 6061-T6 and AA 7075-T651, extensive studies were conducted to characterize the general thermal cycle, microstructure and mechanical properties of welded specimens. The influence of the process parameters, sheet thickness and tool size on the resulting thermal cycle, microstructure and mechanical properties was analyzed for these alloy. For AA 2219-T851, a smaller scale study was conducted to characterize the general thermal cycle, microstructure and mechanical properties of welded specimens. A detailed description of the design of experiments employed for each alloy is given below.

Additional welds to the ones reported below were conducted, for example, repair welds to analyze the microstructural characteristics and formation mechanism, differential scanning calorimetry (DSC) analysis or completely different weld experiments to analyze the material behavior during high-shear-rate plastic deformation. The process parameters or, if necessary, a description of the experimental approach is given in the respective chapters for those experiments.

Unless otherwise noted, the reported characteristics in this work refer to the keyhole repair process described above. To analyze whether the observed phenomena are caused by the interface of the plug and surrounding workpiece or by the plug itself, replicates of selected welds were performed directly in the base material without a keyhole or plug.

AA 6061-T6

To correlate energy input with thermal cycle and analyze the influence of the process parameters on AA 6061-T6, the temperature in the heat-affected zone (HAZ) was measured in a 3^3 full factorial design study with two replicates repairing keyholes with diameter of 7.5 mm in 3 mm sheets. The tool rotational speed was varied from 1700 to 3000 rpm, and the sleeve plunge and retract speed were varied from 0.844 to 1.056 mm/s. The thermal cycle characteristics as well as the effect of changing

tool size and sheet thickness were analyzed in this alloy by employing the center point parameter or another parameter set within the process parameter window.

To analyze the mechanical properties of the keyhole repair welds in AA 6061-T6, a face-centered central composite design employing 4 factors at 3 levels and 7 center point replicates was analyzed repairing keyholes with a diameter of 7.5 mm in 6 mm thick sheets. The factors were tool rotational speed (2000 – 2700 rpm), sleeve plunge speed (0.75 – 1 mm/s), sleeve retract speed (0.75 – 1 mm/s) and dwell time (0 – 1 s). As the standard deviation was found to be low and the process parameter variation did not significantly influence the mechanical properties, additional axial points of the central composite design were added to analyze the tensile characteristics. The process parameter range tested to obtain the tensile characteristics were thus rotational speeds from 1650 to 3050 rpm, sleeve plunge speeds from 0.625 to 1.125 mm/s, sleeve retract speeds from 0.625 to 1.125 mm/s and dwell times from 0 to 1.5 s.

In 3 mm thick sheets welded using the medium size tool in AA 6061-T6, the influence of the process parameters was analyzed employing a factorial design with 2 factors at 3 levels and 2 overall replicates, as well as 3 additional center point replicates. The factors were tool rotational speed (1700 – 2809 rpm) as well as sleeve plunge and retract speed (0.8 – 1.1 mm/s).

To compare the mechanical properties of welds employing different tool sizes in 3 mm thick sheets, repair welds using the small tool at 1700 rpm and 0.6 mm/s sleeve plunge and retract speed and using the large tool at 2350 rpm and 0.95 mm/s sleeve plunge and retract speed were conducted.

AA 7075-T651

To correlate energy input with thermal cycle and analyze the influence of the process parameters on AA 7075-T651, the temperature in the HAZ was measured in a 3^3 full factorial design study including 3 center point replicates repairing keyholes with a diameter of 7.5 mm in 3 mm sheets. The tool rotational speed was varied from 1500 to 2100 rpm and the sleeve plunge and retract speed used were varied from 0.75 to 1 mm/s. The thermal cycle characteristics as well as the tool size and sheet thickness influence were analyzed in this alloy by employing the center point parameter or another parameter set within the process parameter window.

To analyze the mechanical properties of the keyhole repair welds in AA 7075-T651, a central composite design employing two factors at 5 levels and 5 center point replicates was analyzed in 3 mm-thick sheets using the medium size tool. The tool rotational speed was varied in a range from 1375 to 2224 rpm, and the sleeve plunge and retract speeds used were varied from 0.64 to 1.06 mm/s.

In 6 mm-thick sheets, the influence of the process parameters was analyzed by employing a full factorial design with 3 factors on 3 levels and 5 center point replicates. The factors were tool rotational speeds from 1500 to 2100 rpm, sleeve plunge speeds from 0.7 to 1 mm/s and sleeve retract speeds from 0.7 – 1 mm/s. Additional experiments at the center point parameters were conducted to analyze the influence of dwell time at the highest plunge depth and of post-weld natural aging on the tensile characteristics. Analysis of dwell time was conducted by holding for 2, 4 and 6 s at the maximum plunge depth with 2 replicates each with the center point parameter. The influence of post-weld natural aging was tested by performing hardness and tensile tests at different days of aging up to a maximum of 25 weeks.

To compare the mechanical properties of welds employing different tool sizes, repair welds using the small tool at 1500 rpm and 0.5 mm/s sleeve plunge and retract speed and using the large tool at 1800 rpm and 0.85 mm/s sleeve plunge and retract speed were conducted in 3 mm-thick sheets.

AA 2219-T851

To analyze the thermal cycle characteristics, microstructure and mechanical properties of AA 2219-T851, welds at a 1350 rpm tool rotational speed and 0.6 mm/s sleeve plunge and retract speeds were conducted in 3 and 6 mm-thick sheets employing the medium size tool.

4.1.4 Energy input calculation

To calculate the energy input during the RFSSW process, an approach similar to that introduced by Su et al. [73] for friction stir spot welding is applied. The total energy needed to perform the RFSSW process is calculated using the axial force, penetration depth, rotational speed and torque according to:

$$Q_{total} = \sum_{n=1}^{n=N} Force(n)(x_n - x_{n-1}) + \sum_{n=1}^{n=N} Torque(n)\omega(n)\Delta t \quad (2)$$

where x_n is the penetration depth at sample n, ω is the angular velocity (rad s^{-1}), n is the sample number, N is the final sample, and Δt is the sampling time. The equation must be applied to the probe and sleeve measurements. Similar to the findings of Su et al. [73] for friction stir spot welding, the contribution from tool rotation is much higher than that due to tool penetration. To characterize the energy input introduced into the welded workpiece, the composition of the total amount of energy calculated using the equation above has to be analyzed.

Frictional resistance in the welding equipment

The frictional resistance in the welding equipment includes the energy needed to rotate the actuators themselves and the frictional resistance in the bearings of all the moving parts in the equipment. Because of the position of the torque and force sensors, the energy needed to overcome this frictional resistance is included in the total energy calculation. As this energy $Q_{equipment}$ is assumed not to affect the welded workpiece by a temperature increase or similar effect, it must be excluded from the total energy input:

$$Q_{applied} = Q_{total} - Q_{equipment} \quad (3)$$

In this way, the energy needed to overcome the frictional resistance inside the weld equipment does not distort the calculated applied energy. For detailed information of how $Q_{equipment}$ was calculated, refer to Appendix A.

$Q_{applied}$ is the applied energy, also referred to as energy input that is thought to influence the base material. The reported values of energy input in this work refer to $Q_{applied}$. Still, this calculated energy input does not solely contain the energy needed to overcome the frictional resistance between the tool and workpiece and the energy needed to move the workpiece material in the tool cavity and back into the weld. The energy needed to overcome the frictional resistance in the weld tool and to accelerate the tool parts is included in $Q_{applied}$.

Frictional resistance between the tool parts

The frictional resistance between the individual tool parts describes the energy needed to generate the relative movement between the three touching tool parts. As the sleeve and clamping ring are typically connected by aluminum inside the tool, a significant amount of energy is needed to rotate the sleeve inside the clamping ring. The probe and sleeve rotate with the same pre-set rotational sleeve so that no relative movement occurs in the rotational direction between these tool parts. Nevertheless, the aluminum in between the probe and sleeve as well as the static friction enables the transmission of torque and force between these tool parts. This complicates the interpretation of the different torque measurements, as the tool parts are affecting each other constantly and the measured values are highly influenced by the aluminum intrusion and wear level of the weld tool.

The energy needed to overcome the frictional resistance between the tool parts is critical to the consideration of the applied energy. The energy conversion due to this frictional resistance does not occur directly in the welded interface or in the welded workpiece. Instead, it occurs in close contact to the workpiece and therefore certainly affects the welded material by heat dissipation. As the heat dissipation conditions are not certain, the energy needed to overcome the frictional resistance between the tool parts is included in the calculation of $Q_{applied}$. Still, a significant amount of the heat is assumed to be conducted through the tool upwards into the welding equipment. It is also assumed that the heat dissipation conditions may vary between the alloys of interest. An estimation of the energy needed to overcome the frictional resistance in the tool parts is given in Chapter 5.1.

Acceleration of the tool parts

As the tool rotational speed is constant during the welding process, the energy needed to accelerate the rotating parts of the welding equipment has to be applied before the actual welding process and will not be included in the total energy calculation. The acceleration of the tool parts in the axial direction during the welding process will be included in the total energy calculation. However, as the energy needed to perform the total axial movement is significantly lower than the contribution of the rotational movement, the energy needed for axial acceleration can be neglected.

4.2 Base material

To cover a wide range of alloying elements and properties, one alloy from each of the three typically used precipitation hardening series was used. As discussed in the following chapters, the chemical composition and mechanical properties of the alloys of interest are the basis for the classification of the material behavior during and after friction welding. The mechanical properties of the plugs were confirmed to match those from the respective BM sheet via hardness measurements. Slight differences from the values shown below are assumed to be caused by the difference in grain structure due to different manufacturing processes.

4.2.1 Aluminum alloy 7075 – T651

The material used in the current study is AA 7075-T651 sheets and plates with 3 and 6 mm thicknesses. The chemical composition and mechanical properties of this material are listed in Table 4.4 and Table 4.5. The temper used was T651, i.e., solution heat treated, stress relieved by stretching and artificially aged. The plugs used as filler material for keyhole closure are machined from extruded rods made from the same alloy in the T6 condition.

Table 4.4 Chemical composition of the AA 7075 used in this study in weight% – obtained by optical emission spectrometry.

	Si	Fe	Mg	Cu	Mn	Cr	Zn	Ti	Al
3 mm	0.07	0.12	2.7	1.7	0.03	0.18	5.9	0.05	Rem.
6 mm	0.12	0.24	2.6	1.6	0.12	0.21	5.9	0.04	Rem.

Table 4.5 Mechanical properties of the AA 7075-T651 used in this study.

	Hardness (HV0.2)	Yield strength (MPa)	Tensile strength (MPa)	Elongation (%)
3 mm	175.2	518	588	11.6
6 mm	184.9	529	576	14.79

4.2.2 Aluminum alloy 6061 – T6

The material used in the current study is the AlMgSiCu alloy AA 6061-T6 in sheets and plates with 3 and 6 mm thicknesses. The chemical composition and mechanical properties of this material are listed in Table 4.6 and Table 4.7. The temper used was T6, i.e., solution heat treated and artificially aged. The plugs used as filler material for keyhole closure are machined from extruded rods made from the same alloy in the T6 condition.

Table 4.6 Chemical composition of the AA 6061 used in this study in weight% – obtained by optical emission spectrometry.

	Si	Fe	Mg	Cu	Mn	Cr	Zn	Ti	Al
3 mm	0.47	0.41	0.85	0.26	0.06	0.09	< 0.01	0.03	Rem.
6 mm	0.59	0.45	1.0	0.35	0.13	0.18	0.11	0.02	Rem.

Table 4.7 Mechanical properties of the AA 6061-T6 used in this study.

	Hardness (HV0.2)	Yield strength (MPa)	Tensile strength (MPa)	Elongation (%)
3 mm	105	267	315	16.4
6 mm	108	284	324	16.1

4.2.3 Aluminum alloy 2219 – T851

The material used in the current study is the AlCu alloy AA 2219-T851 in sheets and plates with 3 and 6 mm thicknesses. The chemical composition and mechanical properties of this material are listed in Table 4.8 and Table 4.9. The temper used was T851, i.e., solution heat treated, stress relieved by stretching and artificially aged. The plugs used as filler material for keyhole closure are machined from extruded rods made from the same alloy in the T6 condition.

Table 4.8 Chemical composition of AA 2219 used in this study in weight% – obtained by optical emission spectrometry.

	Si	Fe	Cu	Mn	Mg	Zn	Ti	V	Zr	Al
3 mm	0.04	0.09	6.4	0.28	< 0.01	0.05	0.03	0.06	0.11	Rem.
6 mm	0.04	0.1	6.1	0.29	< 0.01	0.05	0.04	0.07	0.13	Rem.

Table 4.9 Mechanical properties of the AA 2219-T851 used in this study.

	Hardness (HV0.2)	Yield strength (MPa)	Tensile strength (MPa)	Elongation (%)
3 and 6 mm	139	353	453	12.68

4.3 Thermal cycle analysis

To correlate the microstructural changes in the different weld zones of the base materials with the temperature exposure during welding, the thermal cycle was monitored at different characteristic positions. For this, K-type thermocouples were embedded in the aluminum sheets at mid-thickness and distances of 9 mm and 17 mm from the center of the weld, as indicated in Figure 4.5. Additionally, the thermal cycle in the weld center was measured by applying a thermocouple at mid-thickness in the plug from the lower surface.

4.4 Metallographic analysis

4.4.1 Metallographic procedure

To obtain cross-sections for metallographic analysis, the samples were cut by diamond abrasive wheels and embedded in a cold mounting resin. The embedded samples were prepared by standard metallographic specimen preparation procedures using flat grinding and finish polishing. For microstructural analysis using polarized light microscopy, samples were anodized using a 3 vol-% solution of HBF4, known as BARKER solution, at 24 V for 2 min for AA 2219 and AA 7075 and at 20 V for 3 min for AA 6061. The grain size was measured following ASTM standard E112-13.

4.4.2 Microscopy

Optical microscopy observations were conducted using a Leica DM IRM optical light microscope, Leica Microsystems GmbH. To characterize various features of the welded microstructures and to analyze the fracture surfaces, an SEM (Quanta™ 650 FEG, FEI Company) was used. Samples for SEM analysis were not etched or mounted in resin.

Correction method for the measurement of circular features in spot welds

When an RFSSW spot is cross-sectioned, it is particularly important to section the sample in the exact middle of the spot weld to ensure dimensional correctness between different cross-sections. Standard metallographic preparation procedures do not deliver the required accuracy. To overcome the problem of inaccurate microstructural measurements due to the position of the cross-section, a correction method applied to measurements of circular microstructural features – for example, the weld zones – is introduced.

The gap between the sleeve and clamping ring of the RFSSW tool leaves a circle of protruding material on the surface of the sheet. In a cross-section, the distance between the protruding parts of material should be equal to the outer sleeve diameter when cross-sectioning the samples in the exact center of the spot weld. The distance a of the cross-section to the ideal cross-section through the center of the weld is calculated using the distance between the protruding parts of material l_p and the sleeve diameter d_s; see Figure 4.6:

$$a = \sqrt{\left(\frac{d_s}{2}\right)^2 - \left(\frac{l_p}{2}\right)^2} \tag{4}$$

Assuming that the macrostructural features are circular in an RFSSW, the measured width from a circular feature x_1 to x_2 will be smaller than the true radial width w; see Figure 4.6. The true distance from point x_1 to the center of the weld is calculated using the measured distance from the point to the center of the weld in the cross-section used:

$$x_{1_{real}} = \sqrt{x_{1_{measured}}^2 + a^2} \tag{5}$$

The true distance from point x_2 to the center of the weld can be calculated similarly. Finally, the true width of the circular feature can be calculated as:

$$w = x_{2_{real}} - x_{1_{real}} \tag{6}$$

The abovementioned correction method applies to horizontal measurements of the distance in or of circular features only. In RFSSW, it applies to measurements, for example, of the width of weld zones, but not to measurements of grain sizes.

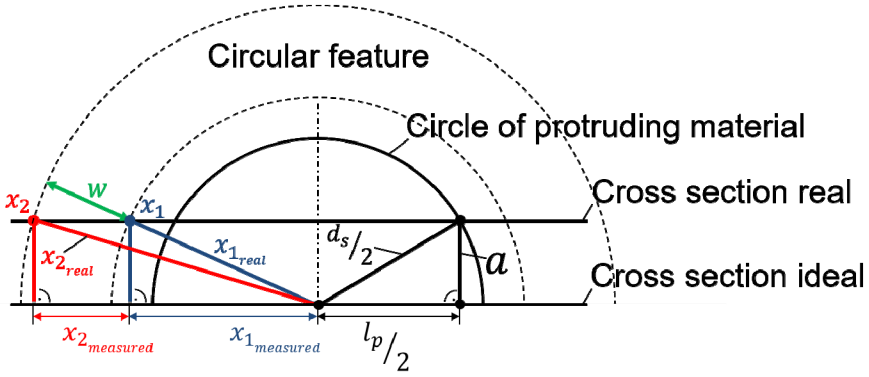

Figure 4.6 Measurement of circular features in cross-sections of RFSSW. Adapted from [30].

4.5 Mechanical testing

Microhardness, micro flat tensile and tensile tests of the base material and welded samples were conducted in this work. The welded coupons were tested after the alloy-specific post-weld natural aging process completed with no further heat or surface treatment.

4.5.1 Microhardness test

Microhardness testing was performed on the aluminum samples to analyze the local mechanical properties. The measurements were performed according to the Vickers method (DIN EN ISO 6507) using Zwick Roell Indentec ZHV 2 hardness testing equipment. Unless otherwise mentioned, the

indentation lines were drawn horizontally at half of the respective sheet thickness in the cross-sections.

4.5.2 Tensile test

For mechanical testing, the welded samples were machined to a dog-bone shape with a gauge length of 50 mm; for comparison, see Figure 4.5. The gauge width was defined as 1.5 times the sleeve diameter, whereas the thickness was given by the thickness of the plate. The remaining sample dimensions were calculated according to DIN 50125:2009-07. Tensile tests were performed in accordance with ISO 6892-1:2009 testing in the rolling direction at RT and at a speed of 1 mm/min using a universal testing machine (Zwick/Roell type 1478).

Digital image correlation

For optical displacement measurements during tensile testing, a digital image correlation (DIC) system (ARAMIS, developed by GOM) consisting of a CCD camera imaging the specimen surface in different loading states and a sensor connected to a computer with image elaboration software was used. The surface of the welded coupons was spray painted to create a random gray intensity distribution that during testing deforms with the specimen surface as a carrier of deformation information. The DIC system records the specimen surface during the deformation and computes the motion of each image point by comparing the images in different states of deformation. The processor was directly connected to the tensile testing machine to obtain the respective load level related to the acquired images.

4.5.3 Micro flat tensile test

Micro flat tensile testing was chosen to analyze the welded interface at the outer regions of the SZ. The specimen geometry was electro-discharge machined according to the design introduced in [74] featuring a gauge length of 10 mm. The micro tensile tests were performed at RT with a constant testing velocity of 0.2 mm/min, and the displacement was measured using a laser extensometer.

4.6 Differential scanning calorimetry

To characterize the precipitate evolution in the aluminum alloys initiated by the welding process, differential scanning calorimetry (DSC) was used. The DSC technique has been used in several investigations to characterize the solid-state reactions accompanying the dissolution and formation of precipitates [75-78]. It was found that DSC analysis can be used as a rapid phase characterization method and that it provides a complementary and quantitative description of the overall microstructure compared to scanning transmission electron microscopy [79].

DSC analysis was performed using a heat flux-type Netzsch DSC 200 F3 Maia instrument on disc-shaped samples with a mass of 70 mg and a diameter of 5 mm. The samples were extracted from the welded coupons horizontally for 3 mm sheets and vertically for 6 mm sheets to increase position accuracy. The reported positions of the DSC measurements refer to the position of the center of the extracted samples in the welded specimens. Pure aluminum crucibles were employed, and a thermodynamically inert 99.5 % pure aluminum disc of equal shape and mass was used as a reference sample. Pure nitrogen was used as the purge gas. The aluminum crucibles were closed by putting the lid on without sealing it to avoid crucible deformation caused by gas expansion. Baseline

measurements were performed by inserting pure aluminum samples into both sides of the DSC furnace. The sample and baseline measurements were recorded sequentially to avoid baseline drift. At least three DSC runs were performed for each measurement to establish reproducibility.

The DSC runs included isothermal steps at RT and at the respective peak temperature where no heat was exchanged by microstructural changes within the sample, enabling reasonable post-processing of the measurements. A heating rate of 10 K/min was selected. Post-run data processing was performed similar to the method reported by Osten et al. [80], i.e., by subtracting a third-degree polynomial to erase the remaining zero-level curvature. For analysis, the excess specific heat capacity c_p – heat flow normalized by the sample mass and scan rate – reflecting the enthalpy changes caused by phase reactions [81, 82] is reported.

5 Process description

The general process description of keyhole repair welds using RFSSW is given in this chapter. The forces and torques acting on the weld tool and the energy input resulting in the typical thermal cycle development are discussed. Additionally, this chapter presents typical joint formation processes of keyhole repair welds using RFSSW. The microstructure and interface formation mechanisms are presented and a general description of the mechanical properties of keyhole repair welds considering the typical strengthening effects in precipitation hardening aluminum alloys is shown.

5.1 Process forces, torque and energy input

The characteristic behavior of the tool positions and rotational speed over process time is shown in Figure 5.1. Here, the surface of the welded sheet is defined as tool position 0; positive values of the tool position describe the direction downwards into the workpiece. The clamping ring moves to the initial position on the surface of the sheet and holds this position for the rest of the welding process. The sleeve and probe are retracted 1 mm from the surface of the sheet to prevent frictional energy generation between the tool and workpiece before the process starts. In the first step, the sleeve and probe are accelerated to the desired rotational speed and are moved downwards to 0.3 mm above the sheet surface. The rotational speed and the direction of rotation of the sleeve and probe are chosen to be equal in this study. The moving tool parts plunge downwards to touch the surface of the sheet while maintaining a constant rotational speed. The actual welding process starts with the sleeve being plunged into the workpiece as the probe is retracted. To constrain the plasticized material that has been displaced by the sleeve into the cavity left by the retracting probe, the probe is retracted further than the sleeve plunges downwards owing to the different front surface size. Thus, the axial speed of the retracting probe is higher than the plunging speed of the sleeve. As the rotational speed of the moving parts is constant, the relative movement between the probe and sleeve is the axial movement. In the second step of the process, the sleeve is retracted as the probe pushes the softened material from the tool cavity back into the joint. The RFSSW keyhole closure process ends with the tool being lifted from the surface of the sheet.

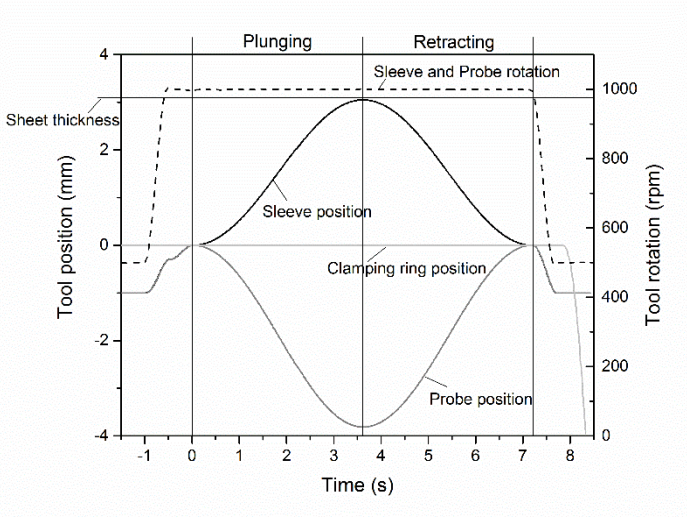

Figure 5.1 Representative tool part positions and rotational speeds during a keyhole repair weld using RFSSW. [30]

Process forces and torque

A typical distribution of the force and torque acting on the rotating tool parts is shown in Figure 5.2 (a). Positive forces describe forces downwards in the direction of the plunging tool.

With initial contact with the sheet, the sleeve force increases, whereas the probe force decreases in the first half of the process. The highest force on the sleeve is reached during the sleeve plunge phase. The probe force behaves oppositely to the sleeve force. The minimum probe force occurs simultaneously to the maximum sleeve force. The probe force increases afterwards during the sleeve-retracting phase of the process, indicating that in this phase, the material is pushed down by the movement of the probe. With the tool parts approaching the upper surface of the sheet in the final phase of the process, both probe and sleeve force approach low values.

Because the rotational speed is constant during the RFSSW process, the torque needed to accelerate the tool parts to the set rotational speed is not included in the analysis. The sleeve and probe torques start at similar values at the beginning of the process when both tool parts are touching the surface of the aluminum sheet. The sleeve torque increases during the plunging phase and continuously decreases during the welding process. The slight decrease in sleeve torque values is assumed to be caused by the softening of the base material. The probe torque decreases during the first half of the process. With no relative rotational movement between the probe and sleeve, this is assumed to be related to the softening of the base material in contact with the probe. The probe torque typically increases slightly with the downward movement as the plasticized material is forced against the front surface of the probe, generating frictional resistance.

As described in Chapter 4.1.4, the individual tool parts constantly influence each other. The force and torque distributions should thus be analyzed with caution. Figure 5.2 (b) shows the force and torque acting on the probe and sleeve during the same welding procedure but without any aluminum workpiece. In this case, the welding equipment performs the same weld process as the one shown in Figure 5.2 (a) in a test run, plunging into air, thereby indicating the force and torque needed to overcome the frictional resistance in the welding equipment and welding tool exclusively. The shown measurement was performed immediately after the weld presented in Figure 5.2 (a). The tool, installation position, relative position of the individual tool parts and level of aluminum intrusion in the tool are thus similar. Nevertheless, as no additional aluminum is pressed into the cavities between the tool parts and as the rotation is assumed to displace some of the existing aluminum in the tool cavities, the condition in the weld tool is slightly different from the condition during welding.

The forces acting on the tool parts show a very similar trend to those arising during the actual weld except for the lower absolute values and the lower probe-force peak in the second half of the process. Still, with peak values of approximately 6 kN for the sleeve and 3 kN on the probe, the forces are higher than expected considering that the parts are plunging into the air. The torque values of both the probe and sleeve are relatively constant at approximately 5 Nm during this experiment. Compared to those of the RFSSW repair weld, the sleeve torque is reduced, whereas the probe torque is very similar.

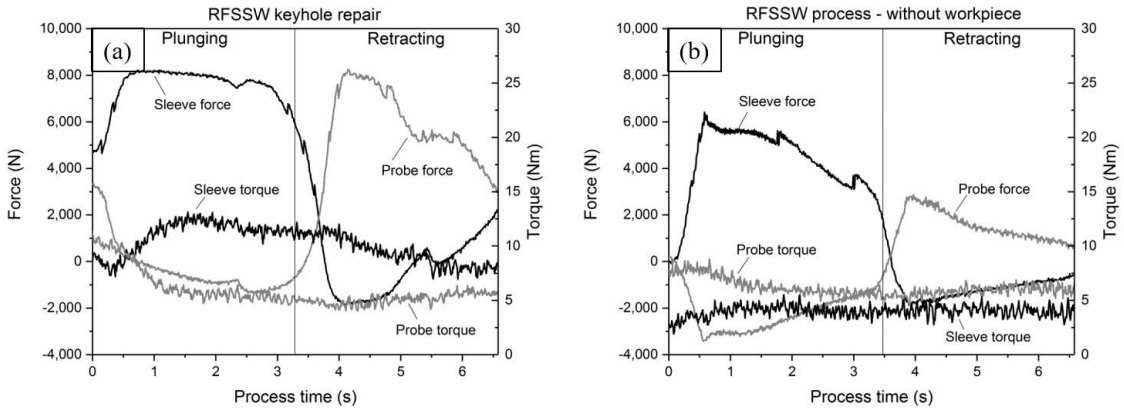

Figure 5.2 Force and torque distribution during RFSSW keyhole repair process in a 3 mm sheet of AA 7075 (a) and RFSSW process without a workpiece but with an aluminum clogged tool (b). Both processes employing the medium size tool and a 1800 rpm rotation speed and 0.85 mm sleeve plunge and retract speeds.

The difference between the curves shown in Figure 5.2 (a) and (b) is caused by the welded aluminum workpiece. A general correction, e.g., subtraction of the force and torque needed in a weld process without a workpiece, is not feasible, as the measurements vary significantly.

Energy input

In general, the measurement of the energy input is essential, since the ideal measurement of forces and torques contains only those needed for the weld process. The forces and torques would allow conclusions regarding the friction condition and material behavior during the process, and the energy input could be used to compare the different alloys used in this study. In the experimental setup used, the measured values of force and torque are highly dependent on the tool, the installation position of the tool, the relative position of the individual tool parts and the level of aluminum intrusion, as described above. This is illustrated by the energy needed to move the aluminum-filled welding tool according to the typical weld process even in the absence of a workpiece. The measurements shown in Figure 5.2 (a) and (b) are part of a test series, in which the experimental procedures without a workpiece were performed directly after standard keyhole repair welds in 3 mm sheets of AA 7075-T651 to guarantee similar testing conditions. On average, the $Q_{applied}$ without a workpiece is 3.6±1.6 kJ compared to 8.7±1.1 kJ for the repair welds in this test series. The measurement of $Q_{applied}$ thus includes the energy needed to overcome the frictional resistance in the tool parts only for the procedure without a workpiece, as introduced in Chapter 4.1.4. The energy needed to overcome the frictional resistance in the tool parts accounts for approximately 40 % of the energy input of the repair welds using RFSSW ($Q_{applied}$) in this particular test series. As the changes in the tool, the relative position of the tool parts and especially the aluminum intrusion level in the tool vary throughout this study, the energy input cannot be used to compare welds of different test series in which the tool is changed or significantly different amounts of aluminum intrusion is assumed.

Within individual test series featuring varying process parameters, an increase in the tool revolutions per mm plunge and retract was found to lead to an increase in the energy input. Figure 5.3 shows this

for welds in AA 6061-T6 and AA 7075-T651. An increase in the revolutions per mm plunge/retract increases the rotation angle over which the torque has to overcome the frictional resistance to hold the constant rotational speed. This results in higher energy input. A similar trend was also found for repair welds using RFSSW in 6 mm-thick sheets of AA 7075-T651 [31]. As it is not certain where the energy conversion occurs that is resulting in the values of $Q_{applied}$ in Figure 5.3, the absolute values cannot be used for evaluation. Thus, the fact that the calculated values are similar for the two alloys is a coincidence. Additionally, it is uncertain how much of the energy increase is affecting the welded base material. The thermal cycle is assumed to be a better indicator to estimate the energy input into the welded sheet; see Section 5.2.

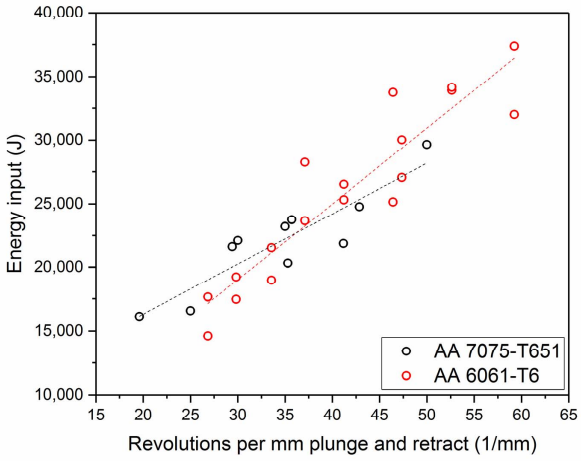

Figure 5.3 Increase in the energy input with increasing tool revolutions per mm plunge and retract using the medium size tool in 3 mm-thick sheets of AA 7075-T651 and AA 6061-T6.

5.2 Thermal cycle analysis

The temperature development in and around the weld spot caused by the energy input is essential to gain information on temperature-dependent phenomena controlling microstructural changes. Figure 5.4 shows typical thermal cycles during keyhole repair welding using 1800 rpm rotational speed and 0.85 mm/s sleeve plunge and retract speeds in the alloys of interest. The temperature rises during the plunge phase of the sleeve with high heating rates. In the center of the weld, the peak temperature is typically reached at mid-process when the sleeve reaches at the pre-set plunge depth. At distances of 9 and 17 mm from the center of the weld, the peak temperature is typically reached during the sleeve retraction phase. The temperature decreases significantly in the weld center during the sleeve retraction phase. After the welding process, the tool is withdrawn from the surface of the workpiece, and the temperature levels out during the cooling process. All welded samples were quenched approximately 5 s after the welding process. For obvious reasons, the quenching effect is not visible in Figure 5.4. As heat conduction is a relatively sluggish process, the heat reaches the positions of measurement in the HAZ with a certain time lag. The correlation of temperature with process time is thus complex. It was determined that the first significant increase in temperature corresponds to the start of the process.

The thermal cycles feature high heating rates and short exposure times at the highest temperatures and high cooling rates. The heating rates are approximately 90°C/s in the weld center and 50°C/s and 30°C/s at 9 mm and 17 mm, respectively, from the center of the weld with minimal variations between the base materials and process parameters.

The thermal cycles exhibit the repeatable effect of the temperature in the order AA 6061-T6 > AA 2219-T851 > AA 7075-T651 in the HAZ when welded using the same process parameters. Such a trend could not be verified for the center of the weld, as the standard deviation is higher for these measurements. Slight differences in the thermocouple position cause a difference in measured temperature in the center of the weld. The thermocouple in the weld center is highly affected by the material flow, which results in changes in the thermocouple position during the process. Such changes in position cannot be tracked. This leads to uncertainty about the exact position of the thermocouple and high standard deviations.

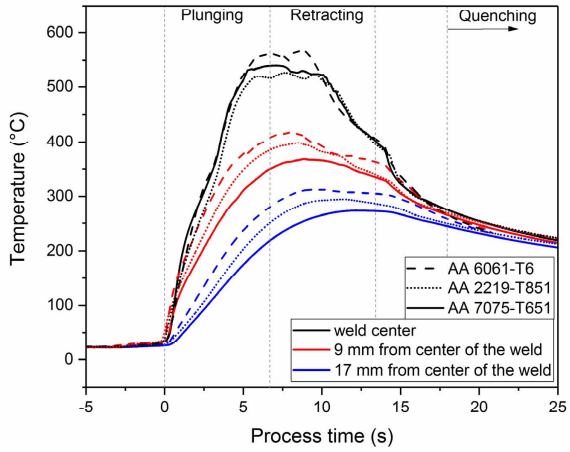

Figure 5.4 Thermal cycle of welds in 6 mm sheets of AA 2219-T851, AA 6061-T6 and AA 7075-T651 welded using a 1800 rpm rotational speed and 0.85 mm/s sleeve plunge and retract speeds.

For the characteristic of the thermal cycle two factors play a decisive role: the energy input into the workpiece and the respective process time. If a high amount of energy is introduced into a workpiece over a long time span, the peak temperature might not rise as high as it would when a lower amount of energy is introduced in a short amount of time. The exposure time to elevated temperatures, on the other hand, would be higher in this case.

The temperature increase in the different weld zones is affected by the heat input and heat transfer conditions. When the boundary conditions for heat transfer are similar, comparing the thermal cycles of different alloys welded with identical process parameters thus is a better way to estimate energy input differences than calculating the energy input. As the heat transfer conditions in and around the tool are not known, the calculated energy cannot be used as a measure for the real energy input into the workpiece. As explained in Chapter 4.1.4, most of the heat generated in the tool is assumed to be dissipated into the welding equipment; thus, it primarily does not affect the welded workpiece. Nevertheless, the energy input in the welded workpiece is affected by the tool and the aluminum

intrusion level to some extent. Measurements comparing the effect of the BM, sheet thickness or process parameters are thus conducted with the least possible variation in influencing factors.

When the same process parameters are used, the temperature in the HAZ in AA 6061-T6 is higher than that in AA 2219-T851, which in turn is higher than that in AA 7075-T651. Moreover, the boundary conditions surrounding the welded specimens are similar. Consequently, it is assumed that the energy input follows the order AA 6061-T6 > AA 2219-T851 > AA 7075-T651. Dedicated experiments were conducted to provide an accurate measurement of the energy input at conditions similar to RFSSW. These experiments are presented and discussed in Chapter 7.

Influence of the process parameters, workpiece thickness and tool size

For the repair welds using RFSSW, the characteristic thermal cycle with high heating and cooling rates and short exposure times to the peak temperature was found to depend on the process parameters, sheet thickness and tool size. The results are shown for AA 6061 as an example in this chapter. Equivalent results for AA 7075-T651 and AA 2219-T851 are presented in Appendix B.

The peak temperature in the HAZ depends on the rotational speed and the sleeve plunge and retract speeds, as illustrated in Figure 5.5 for welds repairing keyholes with a diameter of 7.5 mm in 3 mm-thick sheets. The peak temperature tends to increase with increasing tool rpm and with decreasing sleeve plunge and retract speeds. For this tool and sheet thickness combination, at 9 mm from the center of the weld, the highest peak temperature was measured at 405°C; the lowest peak temperature at 362°C, depending on the process parameters in AA 6061-T6. At 17 mm from the center of the weld, the highest peak temperature was measured at 294°C and the lowest peak temperature at 262°C.

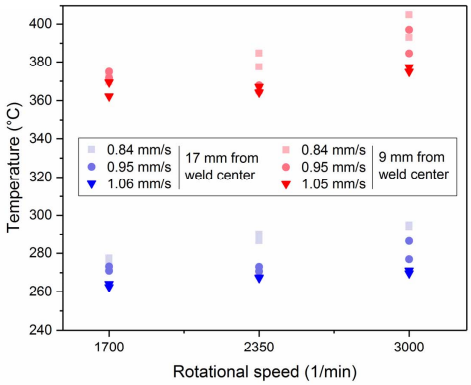

Figure 5.5 Peak temperatures in the HAZ of 3 mm sheets of AA 6061-T6 depending on the rotational speed and sleeve plunge and retract speeds. The same test series was used to calculate the energy input depending on the tool revolutions per mm plunge and retract in Figure 5.3.

Increasing the sheet thickness leads to a change in peak temperature and exposure time while maintaining the typical characteristics of the thermal cycle. Figure 5.6 shows the thermal cycle repairing keyholes with a diameter of 7.5 mm in 3 and 6 mm-thick sheets of AA 6061-T6 with the same process parameters. In the HAZ, both the peak temperature and the exposure time increase with increasing sheet thickness. In the SZ, the exposure time increases, whereas the measurement of the peak temperature is not comparable, as indicated above. The increased exposure time is obviously

caused by the longer weld duration needed when employing the same process parameters, whereas the change in peak temperature is also affected by the change in heat dissipation conditions. Increasing the sheet thickness from 3 to 6 mm increases the peak temperature in the HAZ approximately 30-40°C and doubles the exposure time.

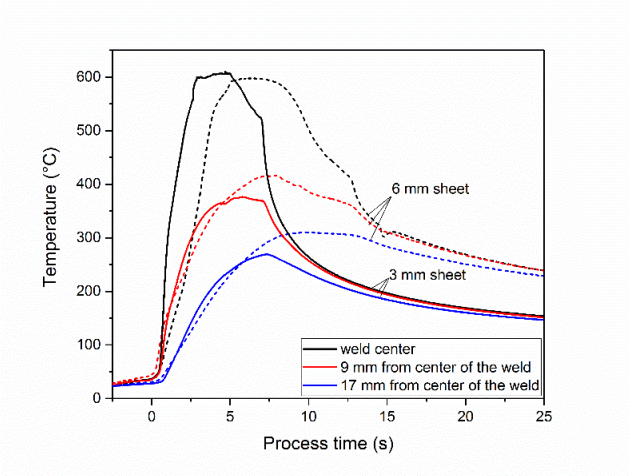

Figure 5.6 Influence of sheet thickness on the typical thermal cycle in AA 6061-T6 welded at 2350 rpm and 0.95 mm/s using the medium size tool to repair keyholes with a diameter of 7.5 mm.

The thermal cycle as a function of the tool size at the position of lowest hardness is shown in Figure 5.7 (a) and at 12 mm from the center of the weld in Figure 5.7 (b). As the sheet thickness and process parameters are the same, the exposure time is similar when comparing welds employing different tool sizes. Nevertheless, the temperatures at a specific distance from the center of the weld increase significantly with increasing tool size. This result is caused by an increase in energy input arising from the use of a larger tool diameter. At the respective position of lowest strength, similar thermal cycles have been recorded, Figure 5.7 (a). Interpreting these findings, the variation in specimen size has to be considered, which changes the heat dissipation conditions. A comprehensive analysis of the mechanical properties is given in Chapter 6.3.3, 6.2.3 and 6.4.3.

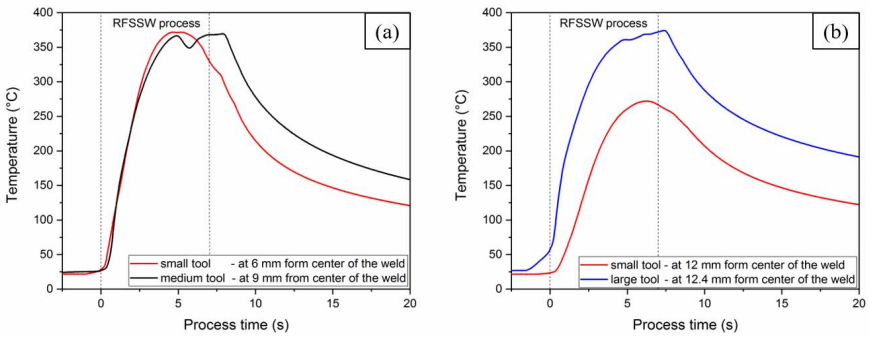

Figure 5.7 Influence of tool size on the thermal cycle in 3 mm-thick sheets of AA 6061-T6 welded at a 1700 rpm rotational speed and 0.84 mm/s plunge and retract speeds: temperature development of welds using the small and medium size tools at the respective position of lowest hardness (a) and of welds using the small and large size tool at 12 mm from the center of the respective weld (b).

5.3 Joint formation

5.3.1 Microstructure formation

The microstructure observed after welding captures the entire flow history of the weld (a description of the final microstructural features is shown in Chapter 6.1.). In order to understand the multi-step RFSSW process, stop-action technique was used to reveal the microstructure formation during the welding process. The analysis of the microstructure formation mechanism in this section is bases on previously published work by the author [31].

Figure 5.8 (a) shows the cross-section after the stop-action technique was applied during the sleeve plunge phase. The material displaced by the downward moving sleeve is clearly located in the cavity underneath the retracting probe. The material from inside the tool was torn off because of the application of the stop-action technique.

The material underneath the rotating sleeve is pressed into the center of the tool. The zone influenced by the sleeve is quite narrow. Because the processed material does not recrystallize evenly with the sleeve plunge depth, the recrystallization and material flow process is more complex. In the initial step of the process, when both of the rotating tool parts come in contact with the surface of the plug and workpiece, a zone of recrystallized material forms close to the surface of the plate. This recrystallized zone is approximately 0.6 mm deep in the weld center. In Figure 5.8 (a), this zone is visible in the upper area of the material underneath the probe.

During the sleeve plunge phase, the material that is not in direct contact with the sleeve is not completely recrystallized, especially in the center of the weld. The elongated grain structure from the plug is still visible. The strain rates are assumed to be lower in the center of the weld where the material primarily moves upwards during the sleeve plunge phase.

The material in the probe cavity does not rotate during the sleeve plunge phase. If it rotated, then a high-shear-rate zone would form in the lower areas of the probe cavity (approximately where the material was torn off in the stop-action experiments) since the plug material underneath the sleeve does not rotate. This process would force the material that is pushed into the probe cavity to pass this zone of high shear. Consequently, the material in the probe cavity would be recrystallized or highly deformed in the rotational direction.

The interface between the plug and surrounding workpiece is not broken and stirred during the sleeve plunging process; in fact, it is pressed into the probe cavity. This interface is still visible but shows damage at higher magnification because of stretching due to the difference in travel between the sleeve and probe. The probe must retract more than the sleeve plunge depth to accommodate the same volume of displaced material. The parts of the interface directly underneath the sleeve are bent towards the center of the weld, indicating the material flow direction.

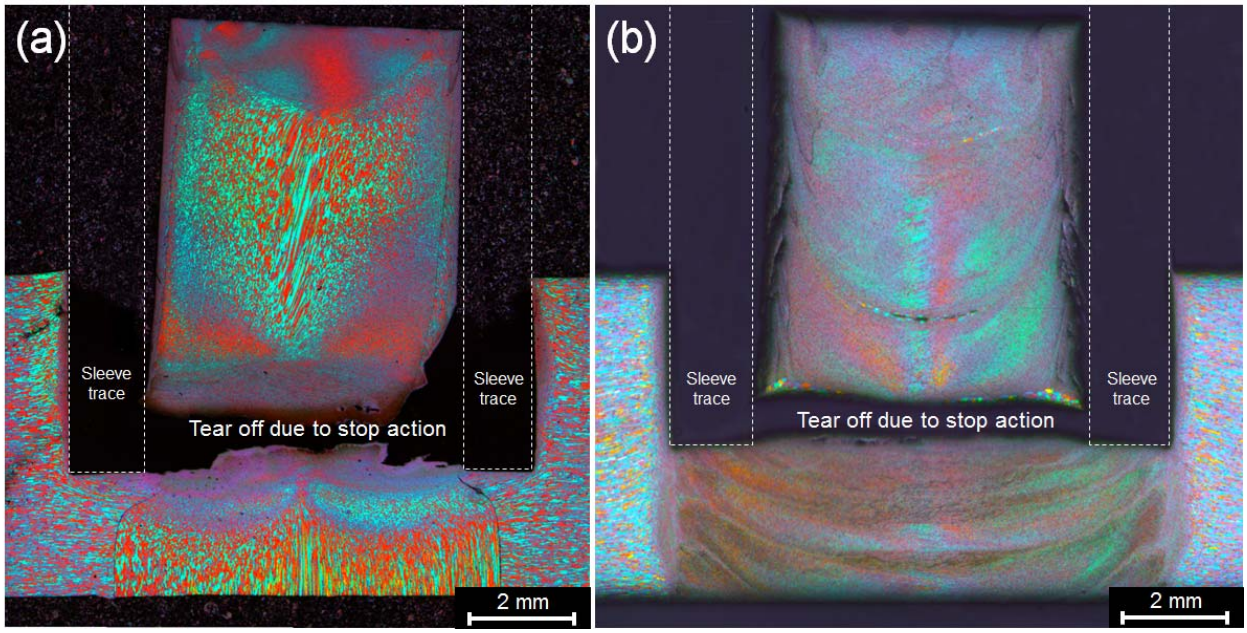

Figure 5.8 Low-magnification overview of stop-action samples of 6 mm sheets of AA 7075-T651: (a) during the sleeve plunge phase and (b) during the sleeve retraction phase of the RFSSW keyhole repair weld.[31]

Figure 5.8 (b) shows a cross-section in which the stop-action technique is applied during the sleeve retraction phase. In this scenario, the material from inside the tool cavity was torn off because of the stop-action technique. The lower portion of the torn-off stub exhibits larger equiaxed grains. The rupture introduced additional plastic deformation into the stub. After the stop-action process, the stub remained in contact with the tool for several minutes, maintaining the elevated temperature and thus enabling grain growth. The flaky surface appearance on the stub can be attributed to sleeve retraction during the stop-action process.

During the sleeve retraction phase, the probe pushes the material in the tool cavity downwards, where high pressure forces the material laterally and slightly upwards to fill the cavity left by the retracting sleeve. A loss of material into the cavities between the tool parts during the process will cause an incomplete refilling of the weld spot in this step of the process. This might lead to void formation in the outer regions of the SZ if the interspaces between the tool parts were not filled with entrapped material.

The material inside the tool cavity shows significantly smaller grains than the same material during the sleeve plunge phase, indicating recrystallization. Certain bands of lower grain size are visible, indicating high concave shear in this material, similar to the final microstructure. Therefore, the rotation of the cylinder-like material is assumed to occur in layers. The areas of highest shear rate form the bands of smaller grain size. The band of unrecrystallized material in the center of the final weld is already separated inside the tool cavity similar to the final microstructural characteristic. The cross-section in Figure 5.8 (b) shows those remaining BM grains as highly distorted in the rotational direction in the weld center, which arises from a higher distance from the cross-section to the exact center of the weld than that in Figure 5.8 (a).

The initial interface between the plug and surrounding workpiece is stirred into the surrounding volume during this process stage. In the material trapped inside the tool cavity, remnants from the joining interfaces are only partially visible. After passing what is assumed to be the area of highest shear rates in the transition zone from inside the tool cavity to the final microstructure, the interface is no longer visible.

During the plunge phase, the material underneath the sleeve is bent in the direction of the weld center and has not been broken up. Because the sleeve must comply with a safety clearance to the backing, a portion of the interface at the lower end of the plug remains underneath the sleeve without becoming entirely shifted into the probe cavity. In contrast to the material that is redistributed from the cavity underneath the probe during the sleeve retraction phase, this material experiences only insufficient stirring.

Figure 5.9 shows a stop-action sample during the sleeve plunge phase, indicating the behavior of material in direct contact with the rotating sleeve. The TMAZ shows both upward deformation and downward deformation in regions close to the edge of the sleeve. Recrystallization can be observed up to approximately 200 µm underneath and on the sides of the rotating sleeve. Thus, the area of the SZ surrounding the sleeve forms during the sleeve plunge phase, and in the second half of the process, the material from inside the tool cavity is distributed against the previously recrystallized material.

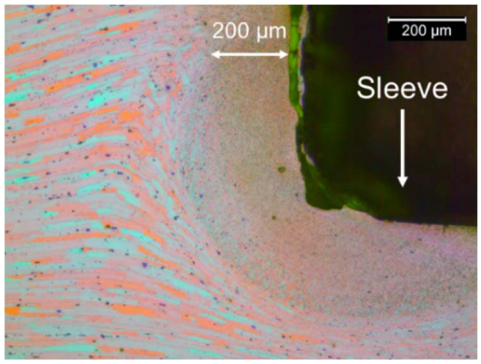

Figure 5.9 High magnification of the sleeve outer edge during the sleeve plunge phase obtained via stop-action experiments in AA 7075-T651.[31]

The discussed phenomena of join formation explain why partial recrystallization is observed in keyhole closure welds. It is assumed that the high plunge depth causes these phenomena because most of the shear required for recrystallization originates from direct contact of the BM with the rotating tool parts. At higher plunge depth, the material in the lower parts of the weld center neither come into contact with rotating tool parts nor are sheared inside the tool cavity during the process. The main directions of material flow in this area are upwards during the sleeve plunge phase and downwards during the sleeve retraction phase, which does not introduce sufficient deformation to begin recrystallization.

To visualize the joint of the plug and the surrounding workpiece, keyhole closure welds were performed employing a dissimilar plug, Figure 5.10. Because of the different etching responses, good contrast between the different alloys was achieved. The mechanisms described above during the sleeve retraction phase of the RFSSW process cause a layered distribution of the plug and surrounding material in the outer regions of the SZ. The characteristic concave form of the layered

material that correlates to the shear layer distribution resembles the hemispherical plane of friction reported for FHPP [83]. Note that the different material properties in this weld lead to a circular undercut on the surface of the sheet in the outer regions of the SZ, often referred to as “lack of refill”. This effect could be avoided by process parameter adjustment. However, for the purpose of this experiment, this defect can be neglected.

Figure 5.10 Low-magnification overview of a 6 mm sheet of AA 6061-T6 welded using a plug made of AA 7075-T651.

5.3.2 Interface formation

The interface in the outer region of the SZ, where the material from inside the tool cavity refills the cavity left by the retracting sleeve, is the actual welded interface. The location of this interface is defined by the outer diameter of the sleeve, as indicated in Figure 6.1. There, the temperature, pressure and pressure duration define the bonding strength, as a diffusion-driven bonding process generates the weld. Additionally, it is assumed that no oxide layer is present at the contacting interface and that interatomic attractive forces occur, contributing to the bonding mechanism [84]. The material underneath the retracting sleeve is thought to have a rotational velocity component; thus, some stirring might enhance the diffusion process due to vacancies formation. No studies were found in the literature on the analysis of this characteristic interface.

To analyze the bonding mechanism and strength of the welded interface, additional welding experiments were conducted. Through the use of a customized measuring device, the pressure on the welded interface was monitored. A detailed description of the experiments is given in Appendix C. Due to the complexity of this measurements only two samples in AA 7075-T651 were investigated. The obtained bonding pressure values are thus interpreted as an estimate and used as reference values for the other two alloys of interest, since the sleeve and probe forces show similar characteristics. Based on the thermal cycle of typical repair welds shown in Chapter 5.2, the temperature at the welded interface during the refilling stage of the process is thought to be approximately 500°C. The sleeve retraction phase of the process took approximately 6.5 s. The pressure at the welded interface was measured in the range of 70 – 120 MPa.

Additionally, micro flat tensile specimens were manufactured in which the welded interface is included in the gauge section of the specimen. The experimental procedure and detailed results are discussed in Appendix C. The ultimate tensile strength (UTS) of the welded interface was found to be greater than 264 MPa for AA 6061-T6 and greater than 505 MPa for AA 7075-T651. For AA 6061-T6, the ultimate tensile strength of the welded interface is higher than those of standard

welded tensile specimens (an analysis of the mechanical properties is shown in Chapter 6.3). In AA 7075-T651 the ultimate tensile strength of the welded interface is also higher than those of standard welded tensile specimens when fracture occurs in the HAZ. Nevertheless, about half of the standard specimens fractured in the region of the welded interface in this alloy, which is, as analyzed in Chapter 6.2, caused by the interface remnants in the lower part of the SZ. It is thus assumed that the strength of the welded interface exceeds the strength in the area of lowest hardness for these two alloys.

To categorize the obtained interfacial strength, the measured values of ultimate tensile strength were compared to diffusion bonding processes employing the same alloys. Finding comparable values in the literature is complex because the temper, thermal cycle and microstructural characteristics are often different. Still, the properties of similar base materials from diffusion bonding experiments can be used to evaluate the bonding strength at the welded interface during RFSSW.

Zuruzi et al. [85] analyzed the effect of surface roughness on the properties of diffusion bonded AA 6061. The in situ interface treatment technique reported in [86] was used to disrupt the surface oxide layer. A bonding pressure of 8.08 MPa at 450°C for up to 90 min was used. The highest ultimate tensile strength achieved was approximately 130 MPa at approximately 80 min of holding time. However, the initial temper state of the base material was not reported.

Sagai Francis Britto et al. [87] diffusion welded AA 7075-T6 by applying a bonding pressure of 10 MPa for 45 min at 425°C. The achieved tensile strength was reported in the range of 50-65 MPa, which is significantly lower than the value reported above of the welded interfacial strength for RFSSW. Huang et al. [88] diffusion welded AA 7075 with a grain size of 6 µm. The shear strength of the bonded specimens reached the BM shear strength of approximately 205 MPa with a bonding pressure of 2.5 – 3.8 MPa, a bonding temperature of 510°C-520°C and a bonding time of 90 – 120 min. To compare to the strength of the bonded interface used in this study, the tensile strength can be calculated by multiplying the shear strength by $\sqrt{3}$, which results in 355 MPa.

Compared to those used during the refilling step of RFSSW, the bonding pressures typically used in diffusion bonding are significantly lower to avoid any macro deformation of the parts, and the bonding times are significantly higher [87-89]. The strength of the welded interface in this study was found to be significantly higher than that of diffusion bonded interfaces. In addition to the higher pressure, the stirring action of the tool is assumed to cause the higher bonding strength.

5.3.3 Strengthening effects and mechanical properties

In precipitation hardening aluminum alloys, a superposition of several strengthening effects occurs, including grain refinement, precipitation hardening and dislocation strengthening, resulting in complex relations between the initial microstructural condition, the thermomechanical treatment during friction welding and the resulting mechanical properties [90].

Precipitate evolution

The welding process causes profound microstructural changes since the alloys investigated in this study contain precipitates, which undergo transformations at elevated temperature. The precipitate evolution caused by exposure to the weld thermal cycle in different weld zones is a complex function of the peak temperature, exposure time as well as heating and cooling rate and depends highly on the

alloy composition and temper state. As precipitation is the main hardening mechanism in the alloys of interest, the exposure to different thermal cycles in the weld zones causes microstructural changes that lead to local variation in mechanical properties. The precipitation evolution for the alloys of interest is analyzed in Chapter 6.3.2, 6.2.2 and 6.4.2 in each case because the aging response depends on the composition and initial temper and thus cannot be generalized.

Grain size and dislocation density

The grains in the SZ were significantly refined, thereby increasing the number of grain boundaries. Grain boundaries can either weaken (intercrystalline fracture, stress-corrosion cracking) or strengthen (Hall-Petch effect) polycrystalline metallic materials [91]. For the quasi-static tests conducted in this study, the strengthening impediment of dislocation movement by grain boundaries is assumed to be dominant. Thus, the strength contribution from grain boundary strengthening is higher in the SZ than in the TMAZ and BM.

A different dislocation density in the stirred regions of friction welds from that in the BM caused by the dynamic recrystallization process is commonly reported. The dislocation density and thus the strength contribution were reported to be higher in the BM of various friction welded precipitation hardening aluminum alloys, e.g., of friction stir-welded AA 2198-T8 [90], AA 6061-T6 [92] and AA 7075-T6 [93].

To assess the general influence of grain refinement strengthening and dislocation strengthening in the alloys of interest, welded samples were solution heat treated and aged at RT; see Appendix D. This treatment equalizes the precipitation morphology in the different weld zones of the welded specimens. Any remaining difference in the hardness of the weld zones can thus be attributed to a difference in grain size and dislocation density. For the alloys of interest, no significant difference in hardness between the weld zones could be determined, whereas significant differences in grain size were apparent. Similar results were reported for solution-treated and artificially aged repair welds using RFSSW of AA 6061-T6 [29]. Since smaller grains cause an increase in strength in aluminum alloys, the weld zones must exhibit a remaining difference in dislocation density to achieve the same hardness. The dislocation density has thus not been equalized in the different weld zones during the solution heat treatment. In AA 2219, the dislocation density might be further reduced in the SZ during the solution treatment due to grain growth. It is thus assumed that the effect of higher grain refinement strengthening is essentially neutralized by the lower dislocation strengthening effect in the SZ than in the HAZ of the welds. This assumption is in reasonable accordance with the results reported by Gao et al. [90] for friction stir-welded AA 2198-T8.

General description of the mechanical properties of keyhole repair welds

The local strength distribution in the different weld zones in the alloys of interest is thus mainly determined by the precipitation morphology. As the alloys were processed in peak-aged conditions, any exposure to elevated temperature will lead to strength reduction by precipitate evolution. Although the deformation during the weld process will undoubtedly have an influence on the precipitate evolution, it is generally assumed that they are second order compared to effects caused by thermal exposure [94]. The kinetics of dissolution, overaging and re-precipitation are alloy dependent and explained in detail in the Chapters 6.2.2, 6.3.2 and 6.4.3 for the alloys of interest. As a result of the weld thermal cycle, transformation of multiple phases and the tendency towards dissolution and subsequent natural aging occurs, which may continue over long timescales. Since the

thermal cycle differs significantly at different distances from the center of the weld, as described in Chapter 5.2, the precipitate evolution varies in the different weld zones.

Typically, the local strength distribution after friction welding of peak-aged precipitation hardening aluminum alloys follows a W-shape over a cross-section though the weld [14, 29, 95-99]. Normally, the SZ features a relatively constant hardness, whereas the lowest values of hardness occur in the HAZ or TMAZ. The development of a W-shape from a near-U-shape in the as-welded condition mainly results from a strength increase in the weld center due to post-weld natural aging. Still, this does not exclude a strength increase due to natural aging in the TMAZ and HAZ. With increasing distance from the weld center, the temperature exposure decreases. At a certain distance, the thermal cycle will not cause significant precipitate evolution. At this point, the strength equals the BM strength, and the HAZ ends.

The strength reduction in and around the weld spot caused mainly by the thermal cycle exposure during RFSSW leads to a typical response during quasi-static tensile testing. Typical strain maps and the strain distribution at the vertical centerline through the center of the weld acquired via DIC, namely, a 6 mm sheet of AA 7075-T651 with keyhole diameter of 7.5 mm repair-welded using the medium size tool, are presented in Figure 5.11. During tensile testing, strain concentrates at approximately 20 mm around the center of the weld, which corresponds to the HAZ dimensions, resulting in a reduced total elongation compared to the BM values. Yielding begins in the areas of lowest hardness, as shown in Figure 5.11 (a). At higher stress, most of the strain accumulates in the areas of low strength in the HAZ at approximately 10 mm from the center of the weld. Note that the area of lowest strength in AA 2219-T851 typically develops closer to the center of the weld than the distribution shown, which applies to AA 6061-T6 and AA 7075-T651. Additionally, strain concentration peaks occur in the outer regions of the SZ. The strain distribution characteristic is inversely proportional to the hardness distribution, except for the peaks in the SZ that become apparent due to the high resolution of the DIC measurement.

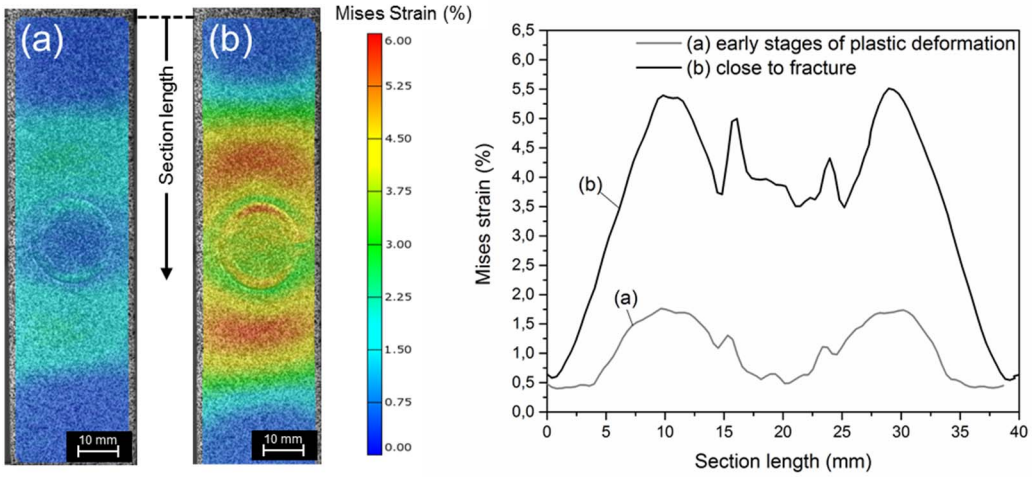

Figure 5.11 Strain maps and strain distribution through the centerline of 6 mm-thick AA 7075-T651 coupons during tensile testing of keyhole closure welded samples (a) at early stages of plastic deformation and (b) close to fracture [31].

6 Microstructural features, precipitate evolution and mechanical properties

The microstructural features, precipitate evolution and mechanical properties of keyhole repair welds using RFSSW in the alloys of interest are shown in this chapter. For this, a comprehensive analysis of the microstructural features of the welds is conducted. Additionally, a detailed analysis of the precipitate evolution in each of the alloys and the resulting mechanical properties of the repair welds are shown. The contribution of the changes in precipitate morphology to the mechanical properties are discussed in detail. The influence of the process parameters, tool size and workpiece thickness to the mechanical properties is shown to characterize the repair procedure over a wider range.

6.1 Microstructural features of keyhole repair welds

The macroscopic structure of a typical cross-section before and after the RFSSW keyhole closure process is shown in Figure 6.1. The comprehensive analysis of the microstructural features is shown exemplary for AA 7075-T651 as this section is in part bases on previously published work by the author [31]. In the pre-welded cross-section, the plug made from an extruded rod shows typical vertically elongated grains, whereas the workpiece material shows elongated pancake-shaped grains in the rolling direction.

As shown in Figure 6.1 (b), the through hole was successfully refilled by joining the plug to the surrounding workpiece. Based on the characteristics of the cross-section, the weld structure is found to be symmetrical with respect to the tool axis. The macrograph of the welded sample displays a defect-free joint without incomplete refill or voids. The initial interface between the plug and the surrounding workpiece is no longer visible.

The microstructure can be classified into four regions that are typical of friction-based processes in precipitation hardening aluminum alloys: SZ, TMAZ, HAZ and BM (compare the microstructural features of conventional welds using RFSSW in Chapter 3.3). BM refers to the material that was not affected by the welding process. The HAZ experiences only thermal cycle exposure during the welding process and is not subjected to plastic deformation. The grain size in the HAZ corresponds to the unaffected base material. The TMAZ is subjected to moderate temperatures and strain rates and is characterized by a deformed microstructure. In the cross-section shown in Figure 6.1, the grains in the TMAZ are bent upwards in the direction of the retracting sleeve. The TMAZ has a torus-like shape that is concavely arched away from the center of the weld. Recrystallization does not occur in the TMAZ because the strain is insufficient. In the SZ, both the temperature and strain rates reach their highest values, forcing the microstructure to recrystallize.

The SZ is wider than the sleeve diameter, indicating high shear rates and temperatures leading to dynamic recrystallization on the outside of the rotating sleeve. Applying the correction method reported in Chapter 4.4.2, the size of the SZ shows an increasing trend with increasing sleeve revolutions per mm plunge and retract; see Appendix E. Still, the standard deviation of the measurement is rather high, and the observed changes in SZ size are small.

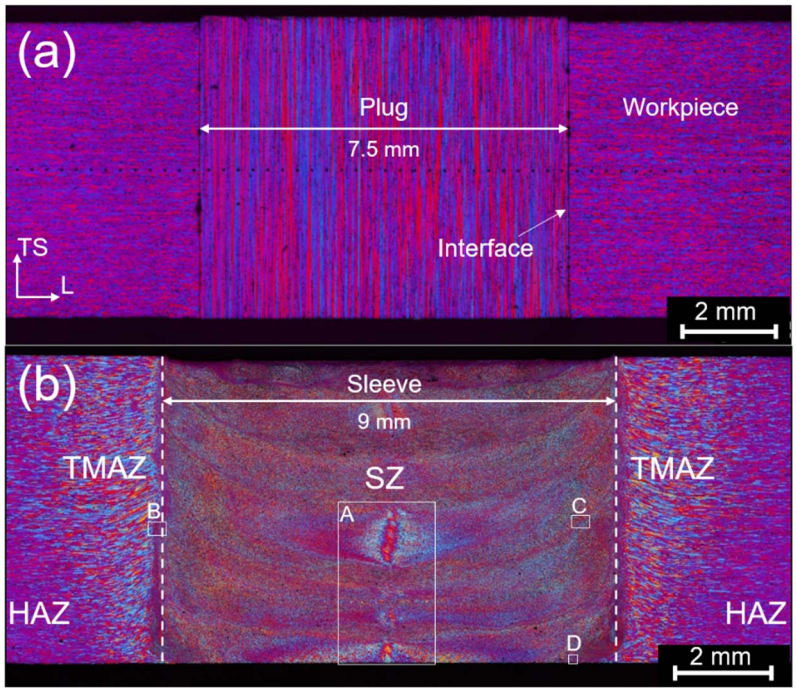

Figure 6.1 Low-magnification overview of unwelded and welded samples of repair welds of keyholes with a diameter of 7.5 mm in 6 mm-thick sheets of AA 7075-T651: (a) unwelded cross-section with an extruded plug and the surrounding workpiece, (b) typical appearance of a welded sample. Adapted from [31].

The accepted view is that the material in the SZ experiences dynamic recrystallization and forms fine equiaxed grains, as these features define the SZ. For conventional RFSSW in AlZnMg(Cu) alloys, Shen et al. [14] and Zhao et al. [64] reported full recrystallization in the SZ. Shen et al. [14] noted a difference in grain size in the SZ and reported much finer recrystallized grains in the outer regions of the SZ than in the center of the weld as well as a variation in the thickness direction. For other friction-based processes in AA 7075, Gerlich et al. [100] observed fine recrystallized grains in the SZ of the friction stir spot welded microstructure.

Magnified views of regions A, B and C in Figure 6.1 are shown in Figure 6.2 to investigate the typical SZ in detail. Figure 6.2 (A) shows the typical inhomogeneity of the grains in the SZ observed in this study. In the center of the SZ at the lower portions of the welded plates, deformed grains are visible that are leftover grains from the initial microstructure of the plug. The elongated grains of the plug experienced strain rates that are not sufficiently high to recrystallize the material. The grains are deformed because of the shear introduced by rotating tool parts.

In addition to these anomalies, the SZ consists of fully recrystallized equiaxed grains. In the regions of the SZ that surround the diameter of the sleeve, a grain size gradient with decreasing diameter is commonly measured in the direction towards the center of the weld, as shown in Figure 6.2 (B). The regions of the SZ that were in direct contact with the outer surface of the rotating sleeve exhibit the smallest grains.

Figure 6.2 (C) shows a layer of smaller grains often seen in the SZ. The layers have a concave shape and are visible throughout the entire SZ. In the center of the weld, the layers are not as defined as

those in the outer regions, where they appear to be quite sharp. In the outer regions of the SZ, the shear layers often appear as dark lines in the overall microstructure and are not to be confused with the dark line-shaped formation caused by secondary phases further discussed in Chapter 7.4.3. The interruption of the unrecrystallized grains in the center of the weld shown in Figure 6.2 (A) is caused by these shear bands. The shear bands originate from material flow inhomogeneity leading to shear localization. In regions where the deformation is localized, the heat causing a local temperature increase by plastic deformation is not dissipated since the time is too short. The flow stress in this region will decrease, and further plastic deformation will become localized and concentrated in a narrow region [101].

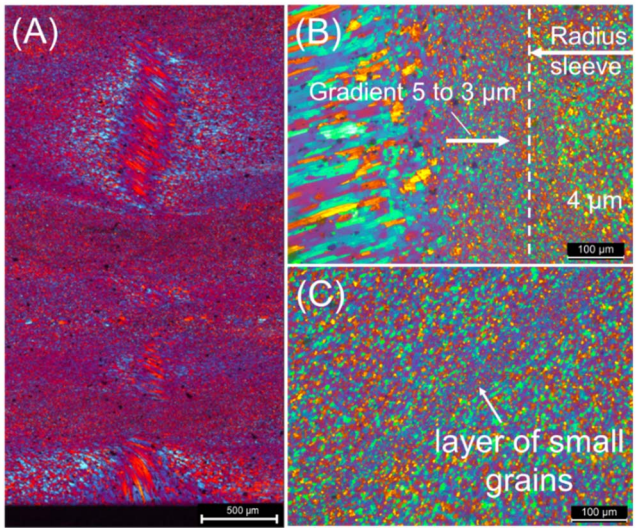

Figure 6.2 Magnified views of regions A, B and C marked in Figure 6.1: (A) partial recrystallization and inhomogeneous grain structure in the SZ, (B) grain size gradient in outer regions of the SZ, (C) layer of small grains in the SZ. [31]

At higher magnification, irregularities in the lower parts of the SZ can be observed as remnants from the interface between the plug and surrounding workpiece, Figure 6.3. A void accumulation forming a typical path starting on the lower surface of the welded workpiece occurs. These remnants are approximately 80 µm long and are typically bended towards the center of the weld. The position of the remnants differs from the initial position of the interface between the plug and surrounding workpiece: the remnants are located further from the center of the weld during the refilling stage of the process. The remnants are assumed to be caused by insufficient stirring during the welding process in the areas underneath the rotating sleeve, as described in Chapter 5.3.1. This phenomenon typically occurs in AA 7075-T651 and AA 2219-T851 and was also found in AA 2198-T851[30] but could not be observed in AA 6061-T6. Similar phenomena have been reported in butt-joints of aluminum alloys using FSW: such phenomena have been interpreted as a high density of oxide particles originating from the original layer present in the abutting surface [102, 103].

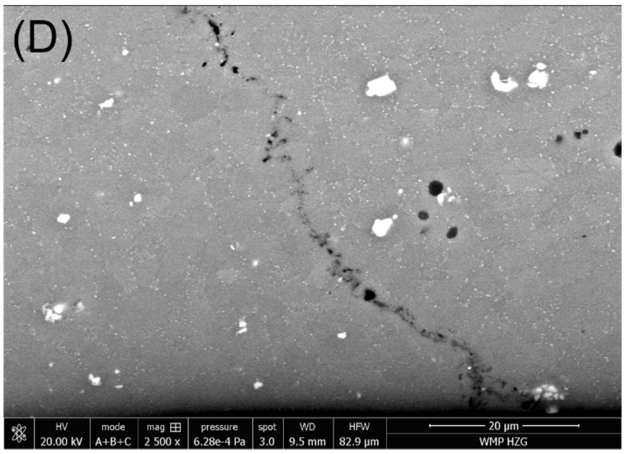

Figure 6.3 Magnified views of region D marked in Figure 6.1 showing remnants from the initial plug-workpiece interface.

Cross-sections of a typical keyhole closure weld formed via RFSSW in the L-TL plane are shown in Figure 6.4. The overview (a) reveals circular weld formation at mid-thickness. Figure 6.4 (b) shows elongated grains in the circumferential direction and certain globular grains at approximately 1 mm from the center of the weld. Figure 6.4 (c) displays fine globular grains, revealing that only a certain ratio of the small and round grains in typical cross-sections (e.g. Figure 6.1) might be recrystallized and equiaxed grains. It is unlikely that the elongated grains in detail (b) are formed from recrystallized and grown grains. The elongated grains are assumed to form from unrecrystallized BM.

The multi-phase aluminum alloys used in this study contain coarse intermetallic particles (often referred to as constituent particles) that form during ingot solidification and are too coarse to interfere with the movement of dislocations or grain boundaries. During rolling, these particles fracture, which causes them to become aligned in the direction of the plastic deformation [104]. In the BM, the constituent particles are thus observed to be aligned in the L direction. Figure 6.4 (b) shows typical alignment of the constituent particles in the circumferential direction in the SZ in accordance with the grain deformation, but in Figure 6.4 (c), no structure of the particles is apparent. Examples of the constituent particles are indicated by arrows in the respective images. The decrease in constituent particles in the zone of high-strain-rate plastic deformation and redistribution in the direction of plastic deformation was also reported for other friction-based processes [69].

The transition zone from the SZ to the TMAZ is shown in Figure 6.4 (d). In the rotational direction, deformed grains form in the beginning of the TMAZ. These grains appear to be of medium size and without a defined structure in the L-TS cross-section in Figure 6.2 (b).

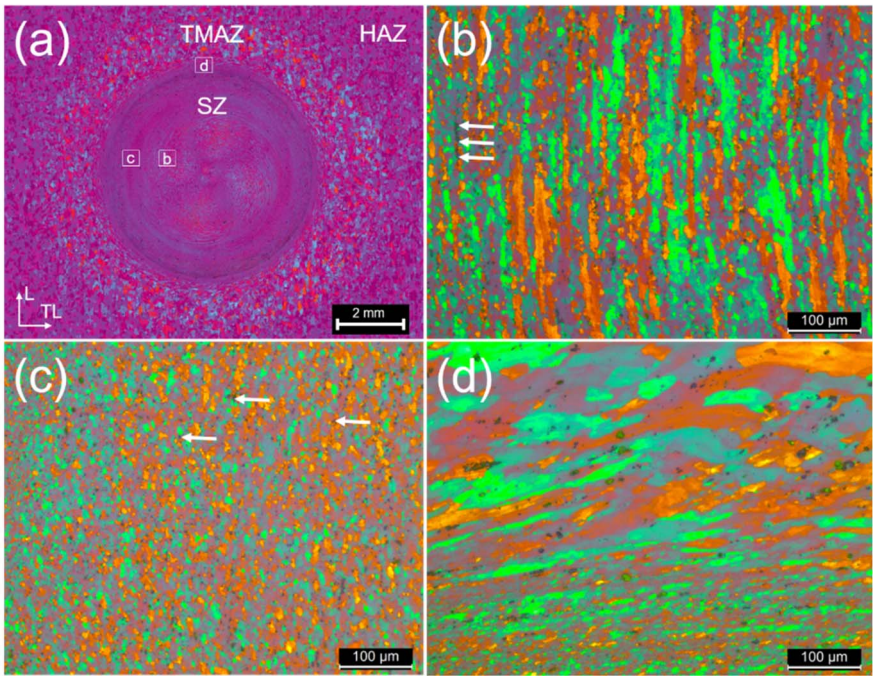

Figure 6.4 Microstructures in the L-TL plane section of keyhole closure welds in AA 7075-T651: (a) Low-magnification overview of RFSSW keyhole closure, (b) elongated grains in the SZ in the peripheral direction, (c) equiaxed grains in the SZ, (d) elongated grains in the TMAZ in the peripheral direction. [31]

Aluminum alloy 6061-T6

The microstructure in welded AA 6061-T6 is shown in Figure 6.5 (a) and (b) for repair welds in 3 mm-thick sheets using the small and medium size tools as an example. In this alloy, the base material features slightly pancake-shaped grains with a length of approximately 50 – 100 µm, Figure 6.5 (A). After the RFSSW process, the characteristic weld zones occur. The SZ is quite narrow with a width of approximately 9.24 mm at mid-height in 3 mm sheets welded using the medium size tool, whereas the width of the TMAZ (approximately 1.48 mm) is comparable to those in the other two alloys of interest. The grains in the TMAZ appear less deformed in AA 6061 and the SZ features mostly small recrystallized grains of approximately 18 µm in diameter with a homogeneous grain size distribution; the shear layer formation reported above does not occur. Still, partial recrystallization in the lower parts of the SZ occurs at times, Figure 6.5 (B). The recrystallization in the SZ of welds using the small tool is typically more comprehensive, especially in AA 6061-T6, which results from the proximity of the respective regions in the SZ to the rotating sleeve during the RFSSW process. In AA 6061-T6, remnants from the initial plug-workpiece interface typically appear in the outer parts of the SZ, Figure 6.5 (C), where the plug and workpiece material is thought to be deposited in a layered structure, as described in Chapter 5.3.1.

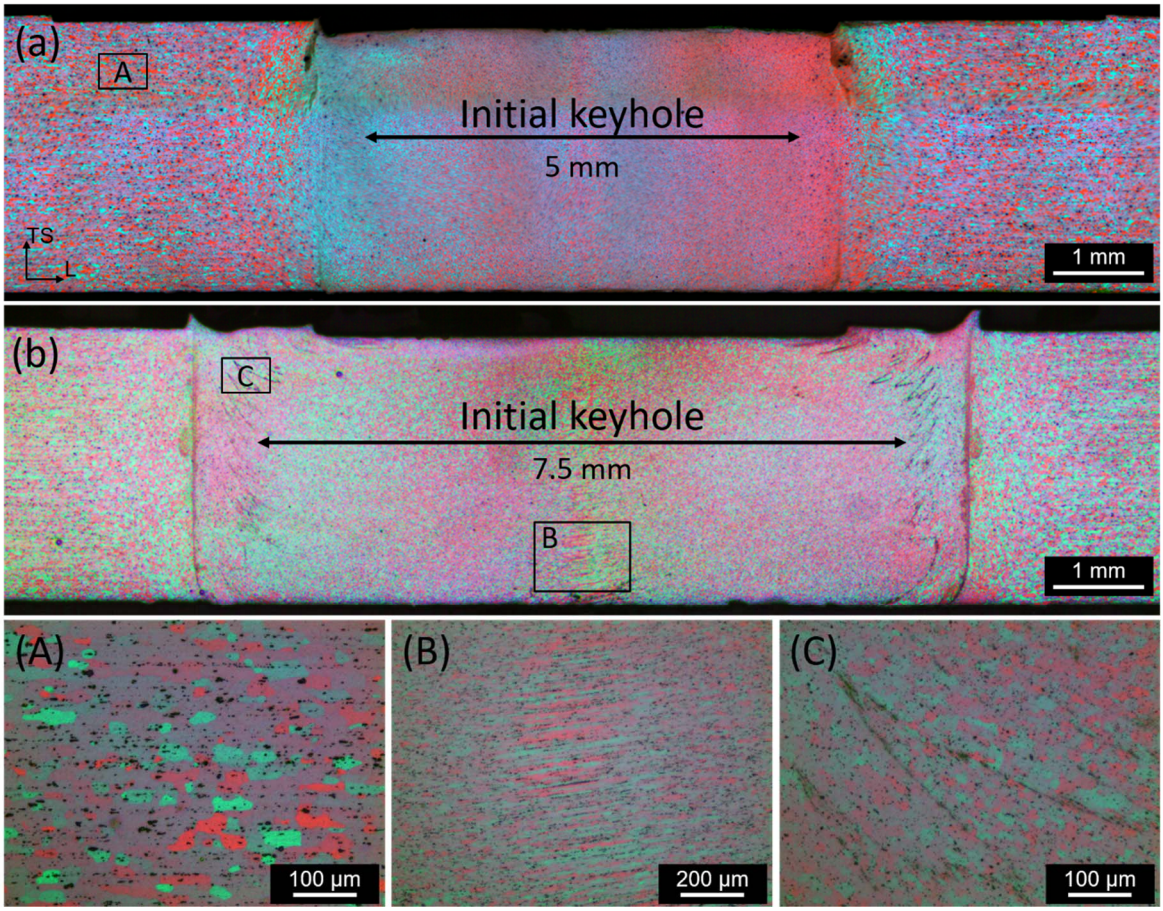

Figure 6.5 Low-magnification overview of welds in 3 mm-thick sheets of AA 6061-T6 using (a) the small and (b) medium tools. Magnified views of regions A, B and C marked in (a) and (b): (A) unaffected base material, (B) deformed grains in the SZ and (C) typical interface remnant formation.

Aluminum alloy 7075-T651

Typically, the grains of the SZ that are fully recrystallized show an average diameter of approximately 4 µm, whereas the average grain size in the shear layers is approximately 2.5 - 3 µm in diameter. In the center of the weld, the shear layers do not appear as defined as those in the outer regions, where they are quite sharp with a thickness near 35 µm. The grain size gradient in the outer regions of the SZ changes the average grain diameter from approximately 5 to 3 µm; see Figure 6.2. The SZ is approximately 400 to 600 µm wider than the sleeve diameter when employing the medium size tool, and the TMAZ has a thickness of approximately 1.4 mm at mid-height.

Aluminum alloy 2219-T851

The microstructure in welded AA 2219-T851 is shown in Figure 6.6 (a) and (b) for repair welds in 3 and 6 mm-thick sheets using the medium size tool. In this alloy, the base material features large pancake-shaped grains with lengths up to 3 mm, Figure 6.6 (A). The TMAZ is approximately 1.47 mm wide, but the region of high deformation close to the SZ is quite narrow, Figure 6.6 (B). The SZ is 9.76 mm wide at mid-height in both 3 and 6 mm-thick sheets, extending 0.38 mm wider

on each side of the rotating sleeve and featuring a very inhomogeneous grain size distribution, Figure 6.6 (C). The average grain diameter of the recrystallized grains in the SZ is 12.8 µm.

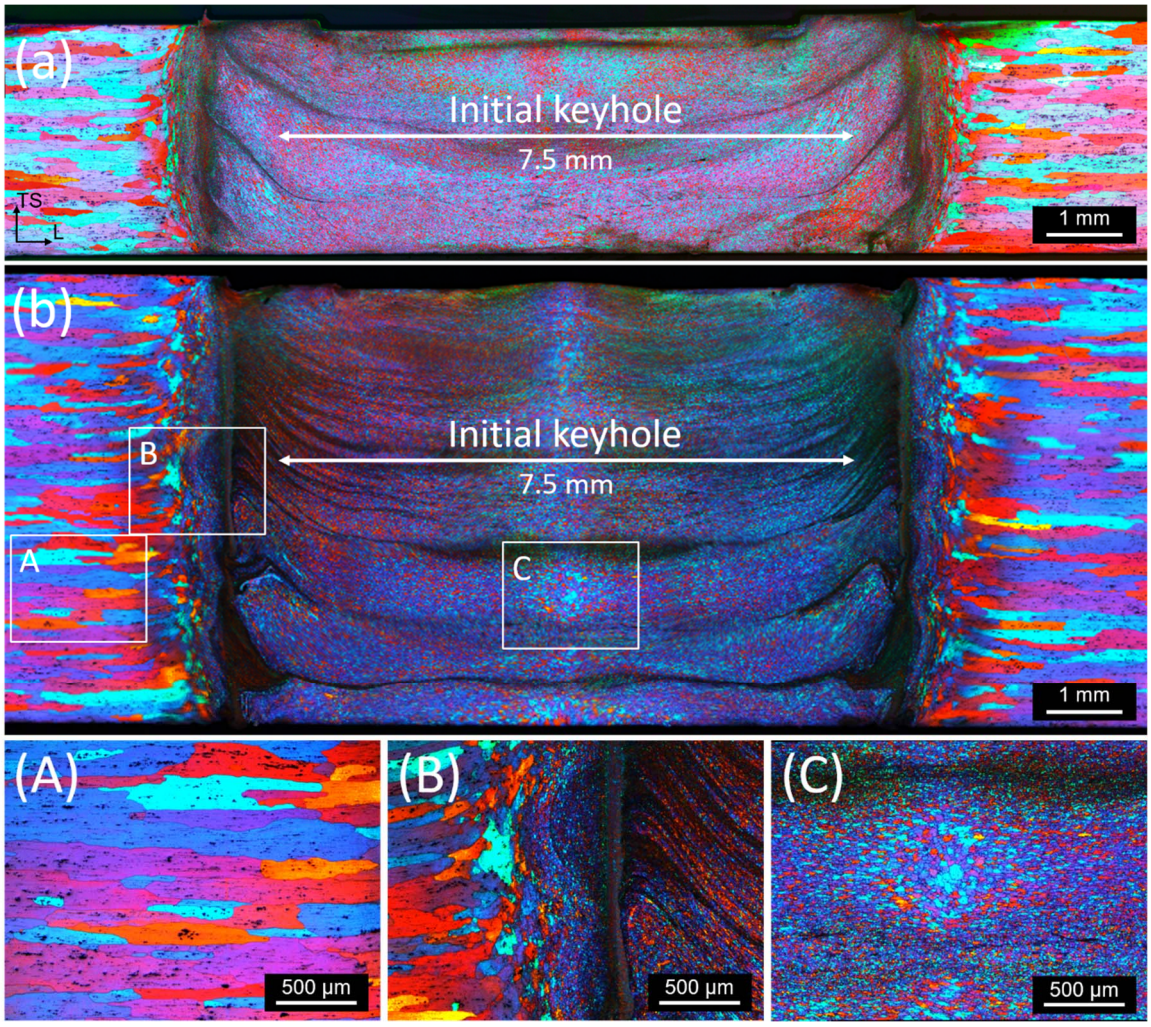

Figure 6.6 Low-magnification overview of welds repairing keyholes with a diameter of 7.5 mm in (a) 3 mm- and (b) 6 mm-thick sheets of AA 2219-T851. Magnified views of regions A, B and C marked in (a) and (b): (A) unaffected base material, (B) transition from TMAZ to SZ and (C) typical inhomogeneity in the SZ. [105]

6.2 Aluminum alloy 7075-T651

6.2.1 Temperature analysis

The peak temperatures measured in the different weld zones are shown in Table 6.1 for repair welds using the center point process parameters in AA 7075-T651. An analysis of the thermal cycle can be found in Chapter 5.2 and Appendix B for this alloy.

Table 6.1 Peak temperatures in the SZ and HAZ in a 3 mm sheet of AA 7075-T651 welded using the medium size tool at 1800 rpm rotational speed and 0.85 mm/s plunge and retract speeds.

Alloy	SZ (°C)	HAZ at 9 mm from weld center (°C)	HAZ at 17 mm from weld center (°C)
AA 7075-T651	541	364	260

6.2.2 Precipitate evolution

The precipitation of AlMgZnCu alloys involves three possible precipitation sequences, depending on the composition [106]. The generally accepted main precipitation sequence [4, 107-109] involves mostly Mg and Zn and is thought to dominate the strengthening in AA 7075:

$$SSSS \rightarrow GP\ zones \rightarrow \eta' \rightarrow \eta$$

The fully coherent GP zones have a spherical shape and were reported to have a composition close to MgZn [106]. Two types of GP zones exist during the early stages of precipitation. The first ones, GP(I) zones, are formed above RT, while the more stable GP(II) zones were reported to form above 70°C. The GP(I) zones change their composition by Mg enrichment during heat treatment and revert completely before the next metastable phase forms, whereas the GP(II) zones are thought to transform into η' phases without dissolution. [110]. Additionally, vacancy-rich clusters with a high Zn content form during quenching from elevated temperatures, which are thought to be precursors of the GP(II) or η' phases [110]. The metastable precipitate η' has a composition and crystal structure close to that of $MgZn_2$ but has a semicoherent interface with the aluminum matrix. The η' phase forms by transformation of the homogeneously distributed GP(II) zones or by nucleation in the area of locally enhanced solute concentration created by GP(I) zone dissolution. The incoherent equilibrium phase η was traditionally thought to have a composition of $MgZn_2$ but was also found to contain other components, i.e., $Mg(Zn,Al,Cu)_2$ or $Mg(Zn_2AlCu)$ [109].

Two other sequences involving S (Al_2MgCu) and T (quaternary phase often referred to as $Al_2Mg_3Zn_3$ or $Mg_{32}(Zn,Al)_{49}$) phases occurring at temperatures above 200°C are reported [109, 111]. These phases are generally thought to precipitate directly from the solute-rich matrix and do not contribute to the alloy strengthening, especially as commercial aging treatments are conducted below 180°C [109].

The main strengthening mechanism appears to be based on the contribution of both coherent GP zones and semicoherent η' precipitates [4, 112].

The DSC curves of the as-received base material in the T651 temper and the solution heat-treated base material are shown in Figure 6.7. The BM was solution heat treated at 480°C for 60 min and quenched in water to RT in order to obtain an SSSS prior to DSC analysis.

Solution heat-treated base material

The calorimetric thermogram of the solution heat-treated samples is in accordance with literature data [108]. The first exothermic peak at 87°C corresponds to GP-zone formation (peak A). The following exothermic doublet at 205°C and 235°C is associated with η' precipitation (peak C) and η precipitation (peak D), respectively. The fourth exothermic peak at 282°C (peak E) corresponds to η growth by Ostwald ripening. The broad endothermic peak at temperatures above 300°C corresponds to the dissolution of the η precipitates (peak F) [108]. The precipitation of the additional equilibrium phases T and S might be included in the formation peaks or are suppressed by superimposed dissolution reactions.

As-received base material

The DSC analysis of the as-received BM is in accordance with other investigations [107, 112, 113]. The first exothermic reaction between 30°C and 160°C is mainly associated with the formation of coherent spherical GP zones [113]. The first endothermic peak at 187°C corresponds primarily to the dissolution of GP zones (peak B). Some preexisting η' precipitates are also expected to dissolve in this temperature range. Formation and growth of the η' phase occurs in this temperature range and is superimposed with the endothermic reaction observed. Additional η' phase formation is thought to be partially included in the subsequent exothermic peak associated with η phase formation [107]. With η formation at 230°C followed by η growth at approximately 255°C and dissolution above 300°C, the behavior at elevated temperatures is similar to that of the solution heat-treated samples.

The as-received base material consist mainly of η' precipitates and exhibits enough solute in the solution for further GP-zone formation.

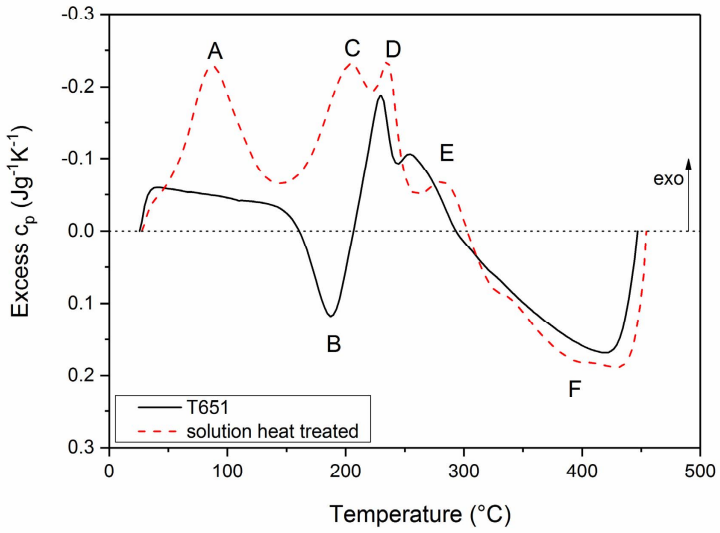

Figure 6.7 DSC curves of AA 7075-T651 in the as-received and solution heat-treated conditions.

Weld zones

The DSC thermograms of samples taken from the different weld zones after complete post-weld natural aging are shown in Figure 6.8. The samples are taken from repair welds of 7.5 mm keyholes in 3 mm-thick sheets welded at a 1800 rpm rotational speed and 0.85 mm/s plunge and retract speeds. Samples were taken from the weld center (SZ) and 9 mm and 17 mm from the weld center within the HAZ. The curves of the samples taken from the SZ and 9 mm from the weld center exhibit similar characteristics, whereas the curve of the sample taken 17 mm from the weld center indicates completely different development.

Kamp et al. [94] developed a model to predict the precipitation evolution during FSW of 7xxx series aluminum alloys. The model was successfully used to predict precipitation evolution in AA 7449 and AA 7010 [94, 114] as well as in AA 7050 [115]. The thermal cycles used in these studies are taken

from FSW of thick plates; therefore, longer thermal cycles than those during the welds in this study are considered. The fastest reported welding cycle took approximately 20 s from RT to peak temperature and back below 100°C in AA 7050 [115], whereas the thermal cycles for AA 7449 took more than 100 s to reach similar peak temperatures [114]. It is still worth comparing the detailed results of these studies with the findings of the DSC analysis in order to characterize the precipitate evolution during RFSSW.

Kamp et al. [114] reported complete dissolution of the preexisting η' precipitates and of the η particles that formed during heating in the heating stage in AA 7449 when increasing the temperatures above 430°C. In a critical range of cooling rates, the model predicts the formation of a limited amount (below a 0.5 % volume fraction) of significantly coarsened η particles (avg. size of 100 nm). Some η' particles can form during cooling with a volume fraction of approximately 2 %. A large amount of solute is reported to be present in solution in the as-welded condition. In AA 7050, complete dissolution of all precipitates and no further precipitation during cooling if the peak temperature exceeds 400°C are reported [115].

Stirred zone

The weld center experiences temperatures above 500°C during the welding process. Most of the strengthening precipitates dissolve during the heating phase of the weld thermal cycle. The black DSC curve in Figure 6.8, representing the SZ, indicates that GP zones form during post-weld natural aging from the large amount of solute that is present in the solution in the as-welded condition. In the subsequent DSC analysis, some additional η' precursors are formed at relatively low temperatures (peak A). At temperatures above 100°C, the endothermic GP-zone dissolution peak, which is known from DSC analysis of the BM in the T6 temper, emerges. With increasing temperature, η' and η formation originating from GP zones formed during post-weld natural aging and during the DSC thermal cycle dominates. The η' formation peak that develops is smaller than that in the DSC curve of the solution heat-treated BM. This indicates the presence of η' precipitates before DSC analysis. Additionally, the small η-growth peak indicates some existing coarsened η precipitates.

The SZ of AA 7075-T651 after RFSSW therefore presents a precipitation morphology with small amounts of existing η' and/or coarsened η phases and large amounts of solute elements in the solution. These findings are in accordance with the abovementioned precipitation model. Thus, it can be assumed that the still existing η' and/or coarse η phases form during the cooling phase of the weld thermal cycle.

Heat-affected zone at 9 mm from the center of the weld

In the HAZ, at 9 mm from the center of the weld, a peak temperature of 364°C and significantly longer thermal cycles with lower heating and cooling rates than those in the SZ were measured. The red DSC curve in Figure 6.8 indicates similar precipitation characteristics as in the SZ with less dissolution during welding and more existing η precipitates in the as-welded condition. In accordance, Kamp et al. [114] and Kamp et al. [115] reported the dissolution of small η' precipitates while heating AA 7449 and AA 7050 to similar temperatures. Coarse η' precipitates transform into η precipitates. A large number of smaller η precipitates dissolve, whereas coarser η precipitates coarsen further. In the cooling leg of the thermal cycle, a small volume fraction of η precipitates was found to form in addition to the undissolved ones in AA 7449 [114].

In contrast to the SZ, some of the existing η precipitates in the as-welded condition are assumed to originate from coarsened undissolved precipitates during welding. The lower heating rate in the HAZ led to less dissolution of the η precipitates, as the existing phases have more time to stabilize by coarsening. Additionally, the lower peak temperature reduces the time above the critical temperature for particle dissolution. The mechanism of η precipitate formation during cooling is assumed to be similar to the mechanism in the SZ. For GP-zone formation during post-weld natural aging, less solute is available in the solution in the as-welded condition.

Heat-affected zone at 17 mm from the center of the weld

In the HAZ, at 17 mm from the center of the weld, the peak temperatures reach 260°C, and therefore, the dissolution temperature is not exceeded. The DSC curve provided in Figure 6.8 indicates very little GP-zone and η'- and η-phase formation. The dominant mechanism during the weld thermal cycle is overaging of preexisting η' precipitates. For post-weld natural aging, only small amounts of solute are left in the solution.

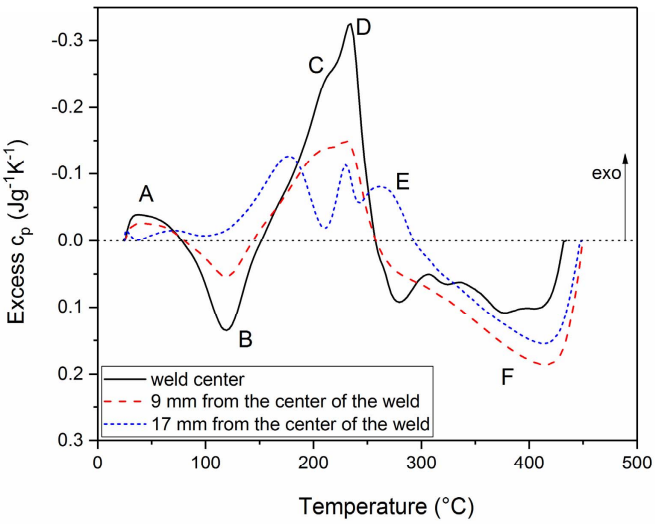

Figure 6.8 DSC curves of the SZ and the HAZ at 9 and 17 mm from the center of the weld of a 3 mm-thick sheet of AA 7075-T651 welded using the medium size tool.

6.2.3 Mechanical properties

Microhardness

The microhardness distribution along the cross-section at mid-height with different durations of post-weld natural aging is presented in Figure 6.9 for repair welds of 7.5 mm diameter keyholes in 6 mm-thick sheet of AA 7075-T651. The keyhole closure welds develop a W-shape hardness distribution, which is typically observed for friction-based welding processes in precipitation hardened aluminum alloys. The SZ shows a relatively constant hardness. From the beginning of the TMAZ, the hardness values decrease continuously to a minimum in the HAZ. Subsequently, as the distance from the center of the weld increases, the hardness values in the HAZ increase to the BM hardness.

For the weld shown in 6 mm-thick sheets welded using the medium size tool, the hardness in the SZ is approximately 36 % lower than the BM values, and the lowest hardness located in the HAZ is 42 % lower than the BM values in the as-welded condition. During post-weld natural aging, on average, the hardness increases in all weld zones, namely, to 148 $HV_{0.2}$ in the SZ and 129 $HV_{0.2}$ in the areas of lowest hardness. These values are 22 % and 33 % lower than the respective BM values. After 4 weeks of post-weld natural aging, no further changes in hardness were measured. After post-weld natural aging, the hardness profiles are in accordance with the findings of Shen et al. [14] in overlap welds of AA 7075 using RFSSW. Additionally, the fully aged SZ hardness is in accordance with the SZ hardness found in the friction stir spot welding of AA 7075 and is similar to the hardness values in a AA 7075 sheet that was solution heat treated and aged at RT for 7 days (149 HV) by Gerlich et al. [100].

After aging, on average, the lowest hardness is located approximately 10 mm from the center of the weld. The heating and thermal transients shown in the thermal cycle at 9 mm from the center of the weld in Figure 8.3 therefore generally represent the most unfavorable case for the BM. The constant hardness in the SZ leads to the assumption that the temperature distribution in the SZ is homogeneous during welding.

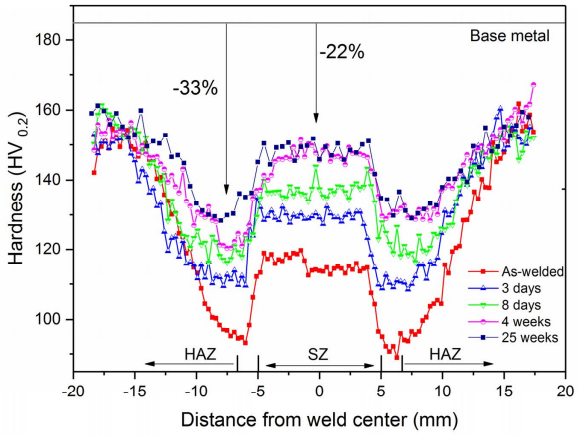

Figure 6.9 Hardness profile of the RFSSW keyhole repair weld in AA 7075-T651 welded at a 1800 rpm rotational speed and 0.85 mm/s sleeve plunge and retract speeds with different post-weld natural aging durations. [31]

Influence of process parameters

No significant influence of the process parameter on the absolute values of microhardness could be observed. Inside the tested process parameter range, when the medium size tool is used to repair 7.5 mm keyholes in 6 mm-thick sheets, the standard deviation is 3.04 % for the average hardness in the SZ and 6.61 % for the measurements of lowest hardness. The higher value for lowest hardness measurements is due to the manner in which microhardness is measured. Hardness measurements are taken at regular distances and will not necessarily hit the exact position of lowest hardness, which increases the standard deviation of that measurement.

No significant influence of the process parameters was found in welds using the medium size tool in 3 mm-thick sheets of AA 7075-T651 either. Within the tested process parameter range, the standard deviation is 2.99 % for the average hardness in the SZ and 3.34 % for the measurements of lowest hardness.

Nevertheless, the measurement of the distance from the position of lowest hardness to the center of the weld tends to increase with increasing revolutions per mm during the welding; see Appendix G. The higher heat input and increasing temperatures in the HAZ shift the thermal cycle that is most unfavorable for the BM to locations further away from the center of the weld.

Influence of tool size

The tool size significantly influences the hardness profile, as shown in Figure 6.10 for welds in 3 mm-thick sheets of AA 7075-T651. The W-shape of the hardness profile narrows with decreasing tool size because of the changes in thermal cycle characteristics, as described above. Additionally, the hardness of the SZ decreases with increasing tool size. On average, the hardness in the SZ is 162 $HV_{0.2}$ when using the small tool, 145 $HV_{0.2}$ when using the medium tool and 137 $HV_{0.2}$ when using the large tool.

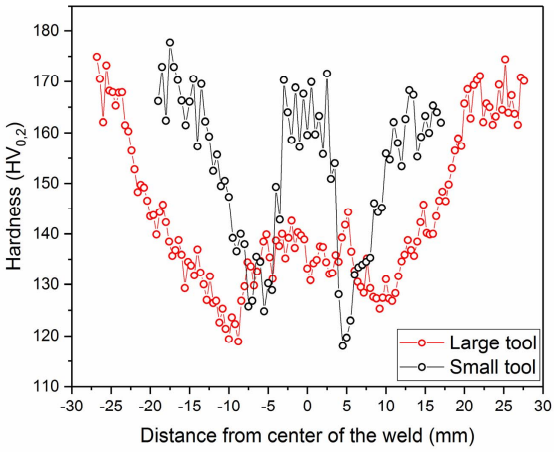

Figure 6.10 Hardness profile of RFSSW keyhole closure welds in 3 mm-thick sheets of AA 7075-T651 using large and small tool, welded at 1500 rpm and 0.5 mm/s (small tool) and 1800 rpm and 0.85 mm/s (large tool).

Analysis of tensile characteristics

Representative stress-strain curves of keyhole repair welds using RFSSW are presented in Figure 6.11. The BM results are in accordance with the literature data. Under monotonic uniaxial loading, the repair welds display characteristic behavior, showing two fracture modes. In AA 7075-T651, welded coupons fractured in either the region of lowest hardness in the HAZ or the outer regions of the SZ. Approximately 70 % of the tested samples failed in the SZ, and the fracture modes were found to not depend on the process parameters. All welded samples regardless of tool size and sheet thickness begin to yield very similar, whereas the ultimate tensile strength (UTS) depends on the

fracture mode. The SZ fracture occurs earlier, reducing the UTS compared to samples that failed in HAZ fracture mode.

Influence of process parameters

In both 3 and 6 mm sheets welded using the medium size tool, no significant influence of the process parameters within the process parameter range employed was found. In welds in 6 mm sheets, the yield strength (YS) showed no dependence on the welding parameters with a standard deviation of 5.1 %. Similarly, the process parameters did not influence the UTS significantly. The standard deviation of the UTS was 1.4 % for HAZ failure and 5.2 % for SZ failure. In 3 mm-thick sheets, the standard deviation of the YS was 2.3 %, and the standard deviation of the UTS was 1.8 % for HAZ failure and 6.1 % for SZ failure.

Influence of sheet thickness and tool size

The sheet thickness significantly influences the tensile characteristic of the welded coupons. In 6 mm-thick sheets, samples welded with the medium size tool begin to yield at 291 MPa (55 % of the BM YS), the UTS in HAZ failure is 425 MPa (74 % of the BM UTS), and the UTS in SZ failure is 401 MPa (70 % of the BM UTS). Decreasing the sheet thickness increases the YS and UTS, Figure 6.11 (a). In 3 mm-thick sheets, the YS is 332 MPa (64 % of BM YS), the UTS in HAZ fracture is 469 MPa (80 % of the BM UTS), and the UTS in SZ fracture is 453 MPa (77 % of the BM UTS).

Employing the small, medium and large tools in welding 3 mm-thick sheets of AA 7075-T651 was found to not influence the tensile characteristic on a large scale, Figure 6.11 (b). Compared to those with the medium size tool, the average YS and UTS in HAZ fracture with the small tool were found to be similar at 331 MPa and 472 MPa, respectively, whereas the UTS in SZ fracture with the small tool was slightly decreased at 399 MPa. The coupons welded using the large tool all failed in SZ fracture with a YS of 305 MPa and a UTS of 340 MPa.

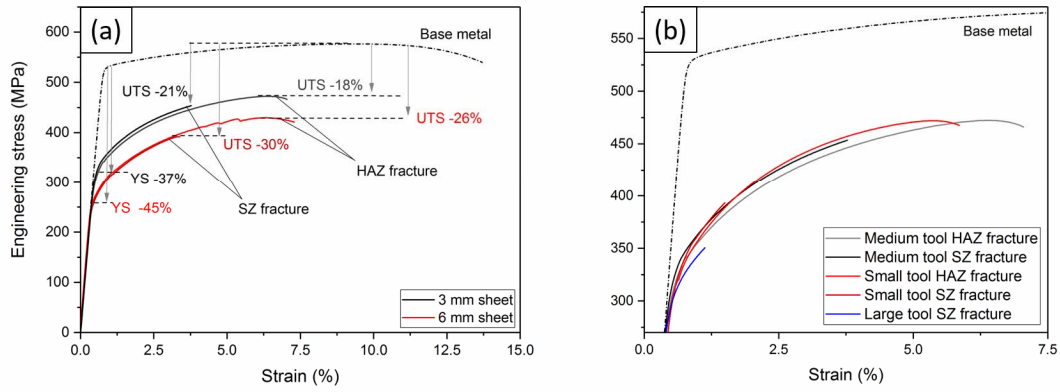

Figure 6.11 Comparison of stress-strain diagrams of keyhole repair welds to those of the BM in AA 7075-T651 welded (a) using the medium size tool in 3 and 6 mm-thick sheets and (b) using different tool sizes in 3 mm-thick sheets.

Fracture modes

The two failure modes reveal the main weakened areas in the keyhole closure welded samples. The first is the area of lowest strength in the HAZ, which is introduced by the thermal cycle during welding. This weakened zone can be observed in the microhardness distribution. The second failure occurs in the outer region of the SZ.

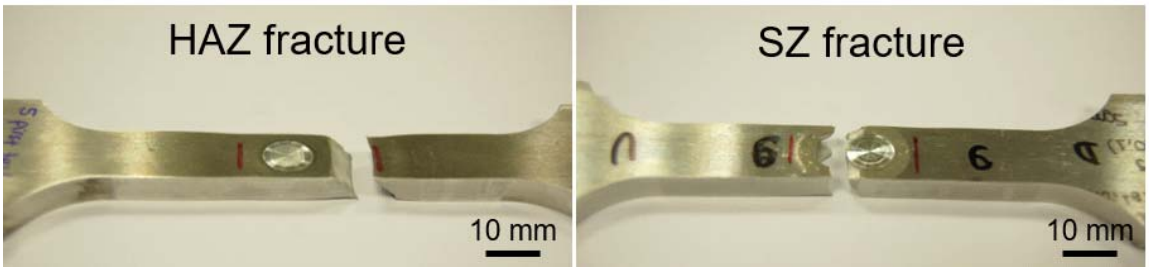

Figure 6.12 Characteristic fracture modes with failure in the HAZ and in the SZ in 6 mm-thick sheets of AA 7075-T651 welded using the medium size tool.

The two fracture modes were analyzed in coupons of 6 mm-thick sheets of AA 7075-T651 welded using the medium size tool to refill keyholes with a diameter of 7.5 mm. The HAZ fracture shows typical microvoid coalescence fracture with transgranular and intergranular fractions and a 45° fracture. The fracture surface shown in Figure 6.13 (a) exhibits large 10 - 50 µm-diameter dimples nucleated at large second-phase particles as well as broad intergranular fractions originating from the shear along the grain boundaries of the large pancake-shaped grains. At higher magnification, Figure 6.13 (A) displays additional small dimples, indicating fracture at fine dispersion phases in a typical slip plane.

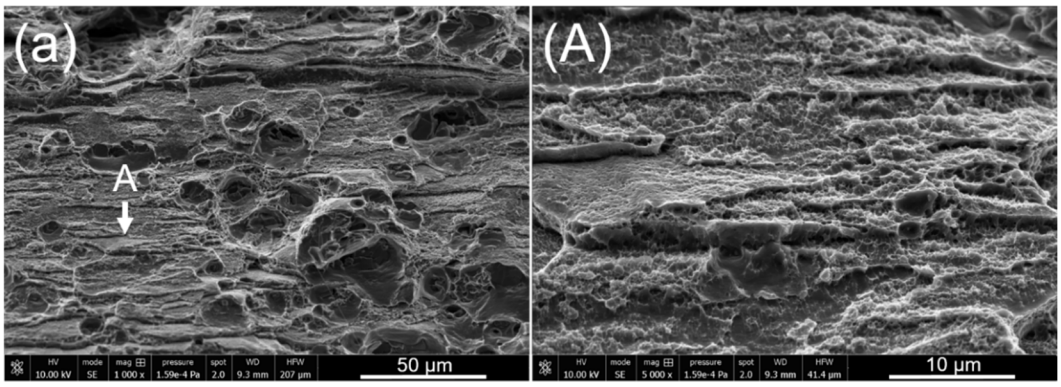

Figure 6.13 Scanning electron micrographs of (a) HAZ-type fracture mode from the center of the fracture surface and (A) magnified view of region A marked in (a). Adapted from [31].

A scanning electron micrograph of the SZ fracture is presented in Figure 6.14 (a), and higher magnification views of the regions marked A, B and C in Figure 6.14 (a) are shown in Figure 6.14 (A), (B) and (C), respectively. Additionally, higher magnifications of the marked regions in Figure 6.14 (A) and (B) are shown in Figure 6.14 (A_1), (A_2), (B_1) and (B_2). The fracture initiates at a weak bonded area in the region of the initial interface between the plug and surrounding workpiece,

which experienced insufficient stirring in the undermost region of the welded plate, as shown in Figure 6.14 (A). A description of the formation mechanism of this interface remnant is given in Chapter 5.3. Figure 6.14 (A_1) shows small dimples indicating low plastic deformation. From this point, the crack propagates upwards, passing the region shown in Figure 6.14 (A_2) with larger and deeper dimple features, which indicate that plasticity increases and that metallurgical combination becomes preferable. Subsequently, the crack propagates upwards with an outward tendency away from the center of the weld. As the crack passes the welded interface described in Chapter 5.3.1, inhomogeneity appears, as shown in Figure 6.14 (B). The region shown in Figure 6.14 (B_1) is characterized by a flat fracture surface with shallow and equiaxed dimples indicating a low deformation level and is assumed to originate from weak bonding in the welded interface. However, the transition zone from the welded interface to the outer regions of the SZ in Figure 6.14 (B_2) shows certain intergranular fracture shares with small dimples on the surface of the SZ grains. In the upper sections of the fracture surface, the crack follows a more outward-bending angle and ends in the interface between the SZ and TMAZ on the surface of the welded plate. Figure 6.14 (C) shows a fracture surface with a combination of shallow dimples and tearing edges as the crack propagates into the TMAZ, with the fracture path indicating larger grains elongated in the rotational direction, as shown in Figure 6.4 (d).

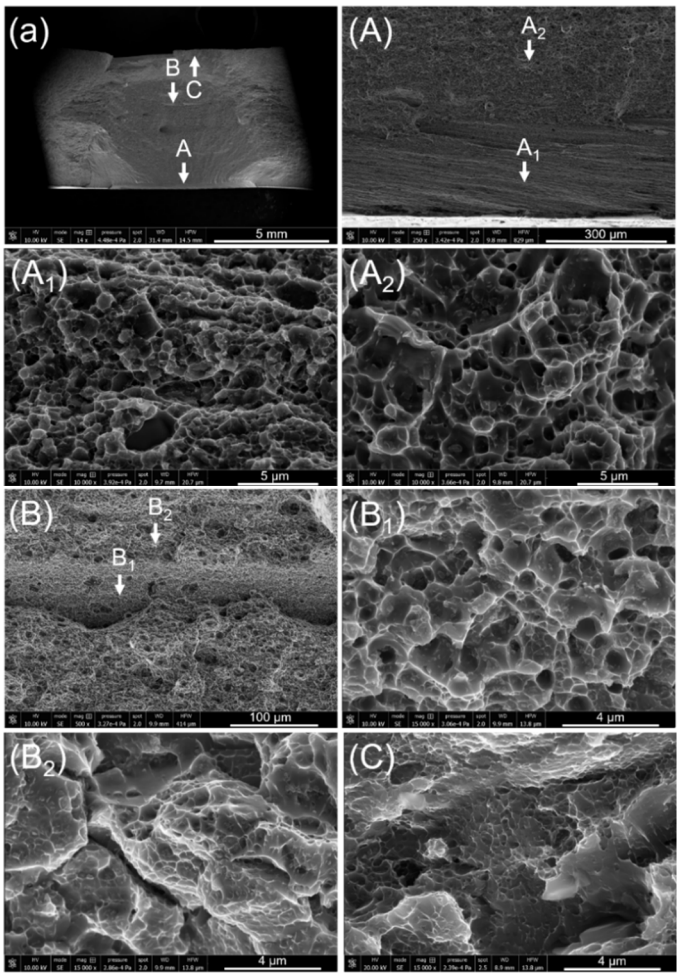

Figure 6.14 Scanning electron micrographs of a) SZ fracture type; A), B) and C) magnified views of regions A, B and C marked in (a); (A_1) and (A_2) magnified views of regions A_1 and A_2 in (A), and (B_1) and (B_2) magnified views of regions B_1 and B_2 in (B). Adapted from [31].

Influence of post-weld natural aging

The yield strength increases significantly during post-weld natural aging, as shown in Figure 6.15. The increase in yield strength correlates with the increase in the hardness in the area of lowest strength in the HAZ because this is the region where yielding begins.

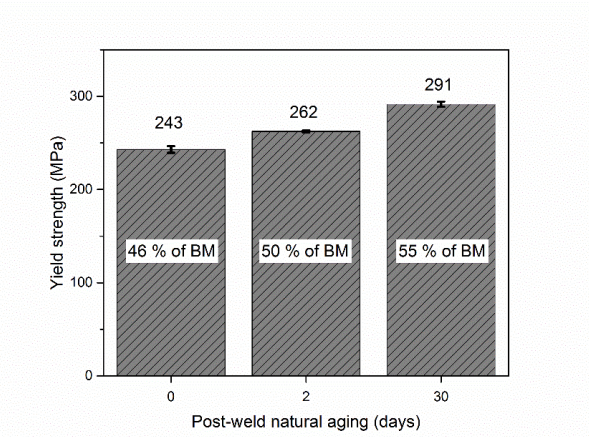

Figure 6.15 Effect of post-weld natural aging on the yield strength of welded samples in 6 mm-thick sheets of AA 7075-T651. [31]

Influence of dwell time

Application of dwell time during welding decreases the mechanical properties of the welds. The influence of dwell time on the yield strength in fully post-weld aged samples is shown in Figure 6.16. Prolonged dwell time increases the energy input during welding, and therefore, the temperature exposure in the HAZ increases, which in turn decreases the strength. Therefore, because flawless welds are achievable without dwell time, the use of dwell time for keyhole closure welding of AA 7075-T6 using RFSSW is not recommended.

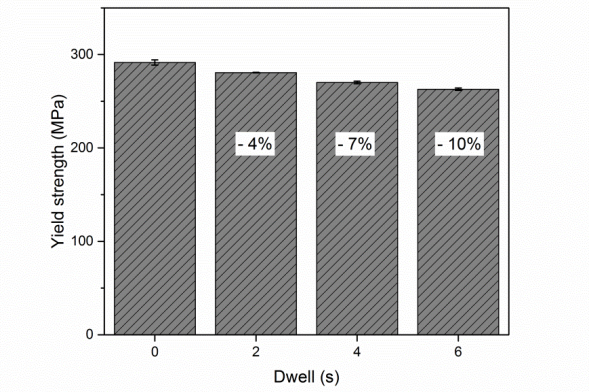

Figure 6.16 Influence of dwell time on the yield strength of welded samples in 6 mm-thick sheets of AA 7075-T651. [31]

6.2.4 Discussion

The thermal cycle causes severe changes in precipitation morphology in the different weld zones compared to the peak-aged BM. In the SZ and surrounding regions, the peak temperature was found to be significantly higher than 500°C. As the dissolution of strengthening precipitates in this alloy starts at temperatures as low as 300°C, dissolution phenomena are inevitable in and around the SZ. Within the region where dissolution phenomena occur during the welding process, the resulting microstructure depends considerably on the heating rate in AA 7075-T651. The heating rate and the peak temperature are highest in the weld center, leading to severe particle dissolution during the weld. With increasing distance from the center of the weld, the heating rate and peak temperature decrease. The lower heating rate allows some preexisting phases to grow and thus become more stable at elevated temperatures. In addition to the lower peak temperature, this leads to less dissolution and thus less solute in the solution in the as-welded condition, which then causes a lower strength increase compared to the weld center due to post-weld natural aging. In general, with increasing distance from the weld center, dissolution of the strengthening phases decreases, whereas overaging phenomena increase. Simultaneously, it is apparent that with increasing distance from the weld center and thus decreasing heating rate and peak temperature, less overaging occurs. For both the weld center and surrounding regions, some phase formation in the cooling stage of the thermal cycle occurs, limiting the post-weld natural aging capability. In the outer regions of the HAZ, overaging phenomena dominate, which reduces the strength and does not allow post-weld natural aging.

The strength in the SZ is higher than that in the adjacent regions because of the greater particle dissolution during the welding thermal cycle and the greater strengthening GP-zone formation during post-weld natural aging. The resulting hardness distribution features a W-shape with constant hardness in the SZ and the lowest hardness at approximately 10 mm from the center of the weld. As discussed in Chapter 5.3.3, the precipitation morphology is mainly responsible for the resulting strength distribution, as the effects of grain size and dislocation density neutralize each other when different weld zones are compared. The region of lowest strength forms in a position at which the combination of overaging and dissolution phenomena is the most unfavorable for this alloy. During post-weld natural aging, the hardness increases in all weld zones, thereby confirming the observed dissolution of preexisting precipitates far into the HAZ.

During tensile testing, the samples were found to start yielding in the areas of lowest hardness and fracture either in that region or in the outer areas of the SZ. For both the hardness and tensile properties, no influence of the process parameters on the strength values were found. The changes in the thermal cycle caused by different process parameters do not alter the lowest hardness or yield strength. Nevertheless, a change in the thermal cycle is thought to cause a different precipitation evolution, which in turn causes different local mechanical properties. As a result, the values of the lowest hardness and yield strength change at a specific position on the welded specimen. Still, a similar lowest strength occurs at a different distance from the center of the weld, resulting in similar global mechanical properties. A higher heat input causes a similar lowest strength at a larger distance from the center of the weld, as the most unfavorable thermal cycle occurs further away from the weld center. Closer to the center of the weld, the higher heat input increases the peak temperature, leading to more dissolution and thus more post-weld natural aging, which in turn increases the strength at this position compared to that of a weld with a lower energy input. In the SZ, process parameters do not change the local mechanical properties, as full dissolution of the strengthening precipitates is assumed to occur in all tested samples.

When the repair welds are conducted in thicker sheets, the yield strength and ultimate tensile strength decrease according to the different thermal cycles with longer exposure times and increased peak temperatures. Employing different tool sizes in the same sheet thickness does not vary the mechanical properties because a similar thermal cycle occurs at a different distance from the center of the respective weld, which results in similar local mechanical properties. The mechanism of the similar hardness and YS at different positions from the center of the weld is similar when comparing welds with different process parameters or welds with different tool sizes but similar process parameters.

The fracture in the SZ was found to initiate at weak bonded interface remnants in the lower parts of the SZ. If these interface remnants do not occur or are strongly bonded, the fracture occurs in the HAZ, as the welded interface in the outer regions of the SZ was found to be stronger than the areas of lowest hardness in the HAZ.

A significant increase in mechanical properties compared to the reported values in AA 7075-T651 using the discussed repair procedure is not assumed to be achievable. Within the developed process parameter window, flawless welds can be achieved, and no significant variation in mechanical properties occurred. As yielding in uniaxial quasi-static testing starts in the region of lowest strength in the HAZ and as the process parameters cause only a slight variation in the position of lowest strength, the overall mechanical properties depend solely on the welded sheet thickness.

Only the UTS of the repair welds can be increased by preventing the plug-workpiece interface remnants. This is achievable by employing a higher plunge depth. Still, increasing the plunge depth increases the possibility of a collision of the sleeve into the backing structure. This damages the sleeve, which might cause the weld quality to suffer or tool fracture to occur.

6.3 Aluminum alloy 6061-T6

6.3.1 Temperature analysis

The peak temperatures measured in the different weld zones are shown in Table 6.2 for repair welds using the center point process parameters in AA 6061-T6. An analysis of the thermal cycle can be found in Chapter 5.2 for this alloy.

Table 6.2 Peak temperatures in the SZ and HAZ in a 3 mm sheet of AA 6061-T6 welded using the medium size tool at a 2350 rpm rotational speed and 0.95 mm/s plunge and retract speeds.

Alloy	SZ (°C)	HAZ at 9 mm from weld center (°C)	HAZ at 17 mm from weld center (°C)
AA 6061-T6	610	382	271

6.3.2 Precipitate evolution

The basic precipitation sequence for AlMgSiCu alloys is given as [25, 76, 116, 117]:

$$SSSS \rightarrow atomic\ clusters \rightarrow GP(I)\ zones \rightarrow \beta'', L, QP, QC \rightarrow \beta', Q' \rightarrow Q$$

Starting from a super saturated solid solution, a complex sequence of cluster formation mechanisms occur [76, 116]. GP(I) zones are reported to have near-spherical shapes, and GP(II) (also referred as to β'') are reported to have needle-like shapes. Both precipitates are at least partially coherent with the matrix [118]. Historically, all the precipitates were assumed to have the equilibrium Mg_2Si

composition. It is now thought that precipitates with the β'' structure can have several compositions, most likely those similar to $Mg_5Al_2Si_4$ [119] or Mg_5Si_6 [117]. Similar to β'', β' is rod-shaped because the β'' needles have grown to rods [76], and the composition is assumed to be $Mg_{1.8}Si$ [117].

Commercial alloys such as AA 6061 often contain varying amounts of Cu, leading to several other possible phases coexisting with β, such as the equilibrium phase Q, which is reported to have a composition close to $Al_3Cu_2Mg_9Si_7$ [117]. The sequence of precipitation leading to the stable equilibrium phase Q was reported as QP→QC→Q'→Q with the hexagonal QP found at peak age, the hexagonal QC at overaging and the hexagonal Q' at prolonged overaging. The lath-shaped L phase is also present at the peak-aged condition and was characterized as a precursor phase for Q that is different from the Q' precursor phase [25]. The Q' precipitate, the coherent precursor of the equilibrium Q phase, is assumed to be essentially the same as Q but with slightly different lattice parameters [117, 120, 121]. The lath morphology distinguishes the Q' phase from the needle-shaped β' precursor of β [25].

Neither Q' nor Q is thought to have significant strengthening potential [25]. At the peak-aged condition, β'' precipitates, precursors of Q' and pre-β''-type precipitates are the dominant strengthening phases [117].

The DSC curves of the as-received base material in the T6 temper and of solution heat-treated base material are shown in Figure 6.17. The BM was solution heat treated at 550°C for 60 min and quenched in water to RT in order to obtain an SSSS prior to DSC analysis. The obtained calorimetric curves are in reasonable accordance with the precipitation sequences reported in the literature [76, 116, 118, 122].

Solution heat-treated base material

For the solution-treated sample, four exothermic formation peaks and three endothermic peaks related to dissolution are found. Figure 6.17 indicates the presence of an exothermic peak centered at 86°C related to Si/Mg co-cluster formation (peak A). Starting from an SSSS, Si and Mg atoms rapidly diffuse due to quenched-in vacancies, forming small Si- and Mg-clusters [76], which occurs during or directly after quenching [116]. A small endothermic reaction at approximately 70°C was reported to be associated with dissolving Mg, which will further combine with the clusters of Si atoms to form co-clusters. These co-clusters might contain Al as well. This small endothermic reaction is not visible in the DSC curve because of the large exothermic reaction in the same temperature range.

A weak and broad exothermic reaction occurs in the temperature range of RT-180°C (peak B). Although this has been referred to as GP(I) zone formation, e.g., in [76] and [123], the GP(I) zones were later found to form at higher temperatures. Currently, it is assumed that in the temperature range of peak B, small precipitates of unknown structure form [116]. These small precipitates were found to be of similar composition to the co-clusters that precede them in the precipitation sequence. Edwards et al. [116] reported that the exothermic reaction reflected in peak B involved ordering processes and possibly the release of Al atoms and/or vacancies from the co-clusters.

The endothermic dissolution peak at 217°C (peak C) indicates the dissolution of previously formed clusters and precipitates [76]. The presence of this endothermic reaction suggests that the transition from previously formed precipitates to GP zones occurs at least partially by dissolution and re-precipitation.

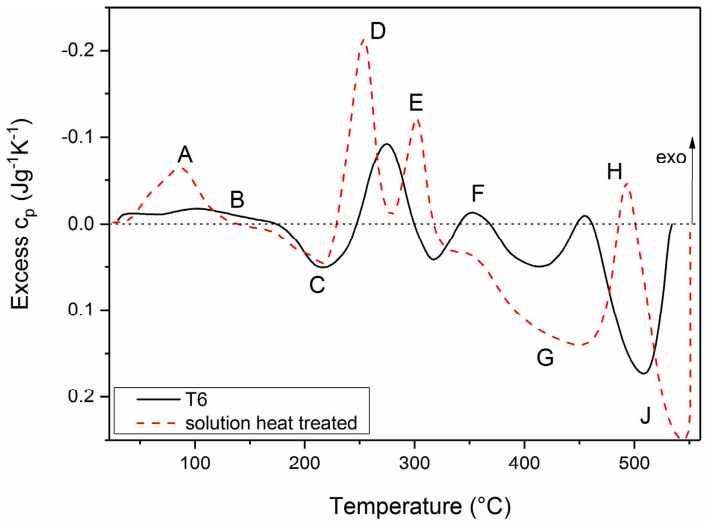

Figure 6.17 DSC curves of AA 6061-T6 in the as-received and solution heat-treated conditions.

The exothermic peak at 252°C (peak D) is assumed to include GP(I) and GP(II) zone (β") formation. I. Dutta [118] reported that pre-aging favors the formation of β" precipitates over GP(I) zones. Pre-aging the samples for 1.5 h at RT was sufficient to suppress the GP(I) zone formation peak in the DSC analysis. The authors concluded that pre-aging supports the formation of β" precipitates directly from previously formed phases without intermediate GP(I) zone formation. For this study, DSC measurements were carried out approximately 0.5 to 1 h after quenching. The single peak D might therefore include some GP(I) zone formation as well. Additionally, it is assumed that precursors of Q' formation form in this temperature range, such as the L and QP phases [117].

The following two exothermic peaks at 302°C (peak E) and at 350°C (peak F) are related to β', QC and Q' formation. Peak F is not extensively pronounced: it shows a local maximum in a larger endothermic peak. Peak E is known from ternary AlMgSi alloys with and without an excess amount of Si or Mg, as reported by [122] or [124], whereas peak F seems to occur because of the addition of Cu. Matsuda et al. [120] found that the β' precipitates nucleate before the Q' phase appears. Thus, exothermic peak E relates to β' and QC precipitation and that the subsequent peak, peak F, relates to Q' formation.

The large endothermic peak at temperatures of approximately 400-450°C (peak G) is attributable to the dissolution of previously formed phases. Most likely, it is mainly linked to the dissolution of the β' phase, as this peak appears in ternary AlMgSi alloys in a similar shape, as reported in [122].

The exothermic peak at 494°C (peak H) is related to equilibrium phase Q precipitation. Above 500°C, an endothermic reaction (peak J), associated with the dissolution of all previously formed phases, predominantly Q [76], appears.

Gupta et al. [125] observed the precipitation of free Si that is not required to form stoichiometric Mg_2Si to follow at least partial dissolution of the β'' particles. The precipitation of free Si might be included in peak E, F or H as well.

As-received base material

In the DSC curve of the as-received BM in the T6 temper shown in Figure 6.17, the first exothermic peak observed in the solution-treated sample, peak A, is not present. The following weak and large peak, peak B, is more pronounced. Furthermore, peak D, the β'' formation peak, is not observed, as the height of this peak is known to decrease with artificial aging time. Peak E, associated with β' precipitation, is shifted to lower temperatures, whereas peak F, the Q' formation peak, is located at similar temperatures but is more strongly pronounced. The dissolution reaction G as well as the Q phase precipitation and ultimate dissolution J are shifted to lower temperatures. During the treatment to T6 temper, precipitates associated with precipitation peaks A, B and D are formed. Therefore, no further cluster formation or β'' precipitation occurs during heating in the DSC analysis. Apparently, the as-received BM still contains particles capable of forming peak B when exposed to temperatures above RT. Despite the shift in the formation temperatures, the precipitation sequence at higher temperatures is merely altered.

Before welding, the BM consists mainly of precipitates associated with peak D, such as β'' precipitates and precursors for Q', as well as additional particles in solution capable of precipitation at lower temperatures to form peak B.

Weld zones

Most studies found in the literature do not sufficiently describe the precipitation evolution in AA 6061 for RFSSW. Maisonnette et al. [126] applied low heating rates of 15 K/s to study the influence of the thermal cycle on precipitation morphology. Additionally, AA 6061 was considered an AlMgSi alloy instead of an AlMgSiCu alloy, a common misinterpretation seen in other studies as well, e.g., [127, 128]. The addition of copper to ternary AlMgSi alloys enhances the precipitation hardening kinetics and significantly changes the highly complex precipitation sequence [117]. In addition to several clustering phases and different metastable precursors of the ternary Q phase, confusion arises from the use of different nomenclatures by different researchers for the same phases [25].

Analysis of weld thermal cycles affecting the precipitation morphology was found for AlMgSi alloys. Myhr et al. [129] developed a model based on the Kampmann and Wagner framework to study the precipitation sequence in AlMgSi alloys during welding. The authors reported that in AlMgSi alloys, the smallest β'' precipitates will dissolve as the larger ones start to grow, leading to β' formation in the temperature range from 250 to 470°C. Above a peak temperature of 470°C, full dissolution of the β'' precipitates was reported. However, this model has been developed for AlMgSi without Cu and considers the metastable β'' and β' precipitates as small equilibrium particles. Uniform thermodynamic properties and fixed composition without differentiation between the various metastable phases are assumed.

Sato et al. [96] applied FSW as well as artificial thermal cycles with a 12 s heating time and a 20 s cooling time to less than 150°C with various peak temperatures to AlMgSi alloy 6063. They observed softening at peak temperatures above 230°C and total dissolution above 350°C. The formation of β at higher temperatures was suppressed by performing high-temperature exposure for insufficient time, leading to a fully dissolved microstructure at high peak temperatures. In the HAZ, at peak temperatures of approximately 300°C, some of the remaining β'' precipitates were reported to grow into β' precipitates.

For FSW in AlMgSiCu alloys, Murr et al. [130] indicated that some of the strengthening precipitates in AA 6061-T6 are not dissolved at peak temperatures of approximately 400°C. Olea et al. [131] reported complete dissolution of the strengthening needle-type precipitates present in the AA 6056-T6 base material in the SZ.

The DSC curves of samples taken from the respective weld zones after complete post-weld natural aging are shown in Figure 6.18. The samples are taken from welds repairing keyholes with a diameter of 7.5 mm in 3 mm-thick sheets at a 2350 rpm rotational speed and 0.95 mm/s plunge and retract speeds.

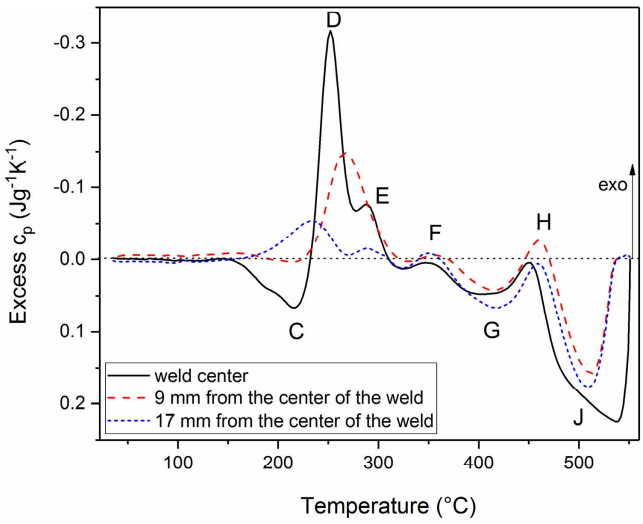

Figure 6.18 DSC curves of the SZ and HAZ at 9 and 17 mm from the center of the weld of a 3 mm sheet of AA 6061-T6 welded using the medium size tool

Stirred zone

The weld center experiences high temperatures of around 600°C during the welding process. The DSC curve of a sample extracted from the center of the weld is shown in Figure 6.18. Neither of exothermic formation peaks at lower temperatures, peaks A and B, form. In addition to exothermic reaction peak E, which is significantly smaller, all of the following peaks appear similar to those in the curve of the base material.

Most of the strengthening precipitates dissolve during the weld thermal cycle, leading to the presence of a large amount of solute in the solution in the as-welded condition. During subsequent natural aging, clusters and precipitates form. These clusters and precipitates dissolve in an endothermic reaction (peak C) during DSC analysis.

The fact that peak E decreased in size compared to the corresponding peak in the solution heat-treated sample indicates that more precipitates associated with this reaction were present before the DSC analysis. Without further analysis of the precipitate evolution during heating and exposure to peak temperature during RFSSW, it is not certain whether the β’ and QC phases withstand the heating and

peak temperatures or whether those form during the cooling phase of the weld. Based on the reported behavior of AlMgSi found in the literature and the DSC curve of the base material, it is assumed that during the welding process, all the precipitates dissolve, and some solute recombines to form β' or QC precipitates during cooling.

Similar to the findings of Sato et al. [96], the temperature in this region passes through the range needed to form the equilibrium phase, but no evidence of precipitation is observed, as indicated by lack of significant change in peak H formation in the curve. It is assumed that the exposure time to temperatures associated with Q formation is insufficient for its precipitation.

The SZ of AA 6061-T6 after RFSSW therefore consists of remaining β' precipitates and large amounts of solute in the solution, allowing post-weld natural aging.

At 9 mm from the center of the weld

In the HAZ, at 9 mm from the center of the weld, a peak temperature of 382°C and significantly longer thermal cycles with lower heating and cooling rates than those in the SZ were measured. The DSC curve in Figure 6.18 indicates significant differences in the precipitation morphology compared to the SZ. No significant precipitation or dissolution reaction occurs until approximately 240°C during the measurement. The exothermic reaction at peak E occurs, and the following peaks appear similar to the behavior seen in the base material.

The dissolution reaction denoted by peak C is indicated marginally, suggesting that a very small amount of solute was present in the solution in the as-welded condition. Very little precipitate dissolution occurred during the welding thermal cycle. Additionally, the particles capable of peak B formation in the unwelded BM do not remain in the solution but evolve during the weld.

Small precipitates associated with peak D, such as β'', are assumed to dissolve as larger ones coarsen, similar to the findings of Myhr et al. [129] for AlMgSi. The absence of the exothermic reaction denoted by peak D proves that no pre-phases for precipitates associated with that reaction are present after welding. Exothermic peak E, associated with β' and QC formation, is pronounced similar to the base material, indicating that coarse precipitates associated with peak D were still present in the microstructure after the welding process.

The strength loss in this region is thus assumed to be mainly caused by the loss of clusters and pre-β'' precipitates and by the coarsening of the strengthening precipitates associated with peak D, such as β''.

At 17 mm from the center of the weld

In the HAZ, at 17 mm from the center of the weld, a peak temperature of 271°C, as well as slowest heating and cooling rates, were measured. The DSC curve in Figure 6.18 exhibits small endothermic peaks D and E, followed by precipitation and dissolution reactions similar to the base material.

Similar to the measurement at 9 mm from the center of the weld, no dissolution occurred during the welding process. It is assumed that the precipitates associated with peak D evolve to form β' and QC precipitates during welding. In contrast to the measurement at 9 mm from the center of the weld, some precipitates are present in the matrix to form precipitates associated with peak D during the DSC measurement. Those precipitates evolve at higher temperatures, and exothermic peak E occurs

in the DSC curve. The very small size of peak E indicates that almost no pre-β' precipitates were present in the as-welded condition.

The region at 17 mm from the center of the weld consist of precipitates associated with peak E, such as β' and QC, in combination with residual pre-β'' precipitates.

6.3.3 Mechanical properties

Microhardness

The microhardness distribution over the cross-section at mid-height at different durations of post-weld natural aging is presented in Figure 6.19 for 6 mm-thick sheets of AA 6061-T6 welded using the medium size tool. The welds form a typical W-shaped hardness distribution with the region of lowest hardness located in the HAZ. For the welds shown, the hardness in the SZ is approximately 46 % lower than that in the BM, and the lowest hardness is 54 % lower than that in the BM in the as-welded condition. During post-weld natural aging, the hardness increases, reaching 82 $HV_{0.2}$ in the SZ and 59 $HV_{0.2}$ in the areas of lowest hardness. These values are 25 % and 45 % lower than that in the BM, respectively. On average, the region of lowest hardness was measured at 8 mm from the center of the weld in 3 mm-thick sheets and at 10 mm from the center of the weld in 6 mm-thick sheets. The thermal cycles at 9 mm from the center of the weld in Figure 5.6 therefore approximately represent the most unfavorable case for the BM.

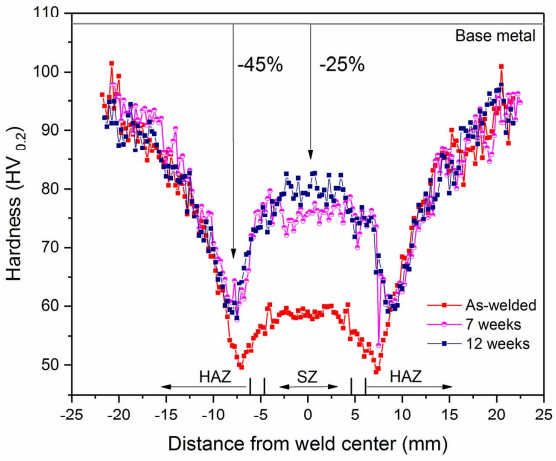

Figure 6.19 Hardness profile of the RFSSW keyhole repair weld in 6 mm-thick sheets of AA 6061-T6 at different post-weld natural aging durations welded at a 2350 rpm rotational speed and 0.875 mm/s sleeve plunge and retract speeds.

Influence of process parameters

No significant influence of the process parameters on the absolute values of microhardness could be observed. Inside the process parameter range tested using the medium size tool in 6 mm-thick sheets, the standard deviation of the average hardness values reported above is 4.4 % in the SZ and 3.5 % for the measurements of lowest hardness in the HAZ. No significant influence of the process parameters was found in welds using the medium size tool in 3 mm-thick sheets of AA 7075-T651

either. Within the tested process parameter range, the standard deviation of the average hardness is 2.4 % in the SZ and 3.35 % for the measurements of lowest hardness.

Similar to the findings for welds in AA 7075-T651, the distance from the lowest hardness to the center of the weld tends to increase with increasing sleeve revolutions per mm during welding, as shown in Appendix F for welds in 6 mm-thick sheets using the medium size tool as an example. A process parameter variation thus changes the position of the thermal cycle, which causes the most unfavorable precipitate evolution in the HAZ, leading to lowest strength.

Influence of sheet thickness and tool size

The tool size significantly influences the hardness profile, as shown in Figure 6.20 for welds in 3 mm-thick sheets of AA 6061-T6. The W-shape of the hardness profile narrows with decreasing tool size because of the changes in thermal cycle characteristics, as described above. The values of the lowest hardness in the HAZ and the average hardness in the SZ were found to be similar. In contrast to AA 7075-T615, a trend of increasing hardness in the SZ with decreasing tool size was not found.

An increase in sheet thickness was found to slightly decrease the hardness over the cross-section. On average, the hardness was 86.2 $HV_{0.2}$ in the SZ and 63.3 $HV_{0.2}$ in the region of lowest hardness in the HAZ in 3 mm-thick sheets welded using the medium size tool. In 6 mm-thick sheets, the hardness measured was slightly lower: 81.5 $HV_{0.2}$ in the SZ and 58.5 $HV_{0.2}$ in the region of lowest hardness.

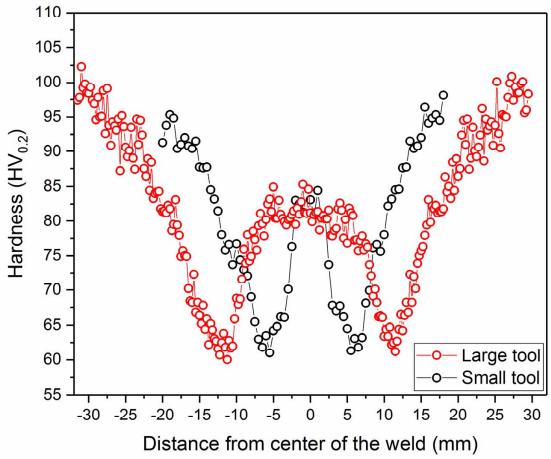

Figure 6.20 Hardness profile of RFSSW keyhole closure welds in 3 mm-thick sheets of AA 6061-T6 using the large and small tools welded at 1700 rpm and 0.6 mm/s.

Analysis of tensile characteristics

Representative stress-strain curves of keyhole repair welds using RFSSW in AA 6061-T6 are presented in Figure 6.21. The BM results are in accordance with the literature data. Under monotonic uniaxial loading, the welded spots display characteristic behavior in this alloy, exhibiting one fracture mode. In AA 6061-T6, welded coupons fractured in the region of lowest hardness in the HAZ. Compared to the BM, the elongation is limited because of the strain concentration in and around the weld spot, as described in Chapter 5.3.3.

The characteristic remnants from the initial plug-workpiece interface that appear in the outer parts of the SZ in this alloy – for comparison, see Figure 6.5 (C) – do not influence the tensile behavior.

Influence of process parameters

In both 3 and 6 mm-thick sheets welded using the medium size tool, no influence of the process parameter on the YS and UTS was found. The tested coupons in 6 mm-thick sheets featured standard deviations of the values of YS and UTS of 2.9 % and 3.1 %, respectively. Similarly, in 3 mm-thick sheets, the corresponding values of standard deviation were 2.4 % and 1.8 %. Nevertheless, it is assumed that the distance from the fracture in the HAZ to the center of the weld varies according to the position of lowest hardness relative to the center of the weld, as reported above.

Influence of sheet thickness and tool size

The sheet thickness significantly influences the tensile characteristic of the welded coupons, Figure 6.21. In 6 mm-thick sheets, samples welded with the medium size tool begin to yield at 131 MPa (46 % of the BM YS), and the UTS is 205 MPa (63 % of the BM UTS). Decreasing the sheet thickness increases the YS and UTS as shown in Figure 6.21. In 3 mm-thick sheets, the average YS is 143 MPa (54 % of the BM YS), and the UTS is 213 MPa (67 % of the BM UTS).

Employing the small, medium and large tools in welding 3 mm-thick sheets of AA 6061-T6 was found to not have a significant influence on the YS and UTS. Coupons welded using the small tool featured a slightly increased YS of 183 MPa, but the UTS was found to be similar to the strength reported above of the medium tool welds at 212 MPa. Samples welded with the large tool were found to start yielding at 151 MPa and to fracture at 157 MPa in the outer region of the SZ due to insufficient bonding in the outer regions, which is thought to be avoidable by weld process optimization.

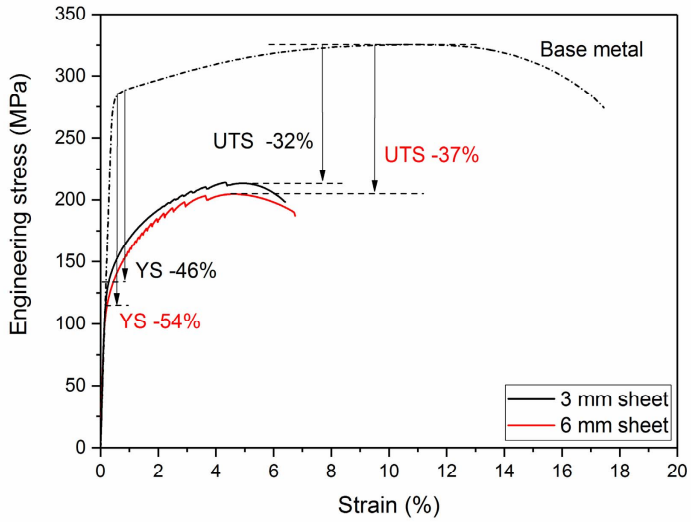

Figure 6.21 Comparison of stress-strain diagrams of keyhole repair welds to those of the BM in 3 and 6 mm-thick sheets of AA 6061-T6 welded using the medium size tool at a 2350 rpm rotational speed and 0.875 mm/s sleeve plunge and retract speeds.

Fracture mode

The welded coupons of AA 6061-T6 typically failed in the HAZ following a 45° path to the applied load. Similar to the HAZ fracture in AA 7075-T651 described below, the fracture occurred approximately at the region of lowest hardness. Employing different tool revolutions per mm plunge and retract is thought to influence the position of lowest hardness in the HAZ and consequently the position of the fracture.

6.3.4 Discussion

The precipitation sequence in this alloy is complex, as several precipitates contribute to the strength in the peak-aged condition. In the SZ of welded samples of AA 6061-T6, dissolution of all strengthening particles was found to occur during welding. During subsequent post-weld natural aging, the hardness was thus found to increase significantly in that region. The strength in the SZ is higher than that in the directly adjacent regions because of the greater particle dissolution during the welding thermal cycle and the greater strengthening GP-zone formation during post-weld natural aging. Very little dissolution was observed at 9 mm from the center of the weld. At 8 mm from the center of the weld, in the position of lowest hardness, an increase in hardness during post-weld natural aging was nevertheless observed. Thus, small amounts of dissolved precipitates causing re-precipitation during post-weld aging at RT are assumed to cause the increase in strength at this position, as the overall ability of AA 6061 to increase in strength during natural aging was found to be higher than those of the other alloys of interest. The analysis of the precipitate evolution indicated that the lowest hardness is caused by the loss of clusters and pre- β'' precipitates and by the coarsening of the strengthening precipitates β'' and precursors for the Q' phase.

Under tensile load, the samples were found to start yielding in the areas of lowest hardness and fracture occurred in the same region. Similar to the findings for AA 7075-T651, as discussed in detail in Chapter 6.2.4, no influence of the process parameter on the strength was found. Instead, the position of lowest strength in the HAZ was found to vary as a function of the thermal cycle. Thicker sheets lead to a longer welding thermal cycle and have thus a negative effect on the mechanical properties. Different tool sizes affect the position of the lowest hardness similar to a change in process parameters.

In repair welds of 3 mm-thick sheets, the plug-workpiece interface remnants were found in an uncharacteristic large extent of the outer regions of the SZ. Still, these remnants did not affect the mechanical properties, and in 6 mm-thick sheets, no interface remnants were observed in general.

The welds in AA 6061-T6 feature an area of lowest strength in the HAZ in which lowest values of hardness and the onset of plastic deformation and fracture were observed. To increase the mechanical properties in this alloy, attention should be focused on reducing the thermal impact, as the local properties in the region are determined by the precipitate evolution.

6.4 Aluminum alloy 2219-T851

This chapter is based on [105] with slight variations.

6.4.1 Temperature analysis

The peak temperatures measured in the different weld zones are shown in Table 6.3 for repair welds using the center point process parameters in AA 2219-T851. An analysis of the thermal cycle can be found in Chapter 5.2 and Appendix B for this alloy.

Table 6.3 Peak temperatures in the SZ and HAZ in a 6 mm sheet of AA 2219-T851 welded using the medium size tool at 1350 rpm rotational speed and 0.6 mm/s plunge and retract speeds.

Alloy	SZ (°C)	HAZ at 9 mm from weld center (°C)	HAZ at 17 mm from weld center (°C)
AA 2219-T851	546	396	305

6.4.2 Precipitate evolution

The generally accepted [79, 132] precipitation sequence of AA 2219 is given as:

$$SSSS \rightarrow GP(I)\ zones \rightarrow \theta'', \theta' \rightarrow \theta$$

The GP(I) zones are disc-shaped Cu mono- or bilayers, whereas θ'' precipitates (also referred to as GP(II) zones) are described as regularly spaced arrays of Cu monolayers [71, 133]. The intermediate θ' phase is platelet shaped and semicoherent and either forms from the coherent θ'' phase or nucleates directly at dislocations in the SSSS [71]. The θ' phase has the composition Al_2Cu [132]. The equilibrium θ (Al_2Cu) phase tends to nucleate heterogeneously at grain boundaries in the aluminum matrix or form from metastable θ' precipitates [26, 132].

The θ'' and θ' precipitates are known to have the highest contribution to strength, whereas the coarse and heterogeneously distributed θ particles do not have strengthening properties [24, 26].

The DSC curves of the as-received base material in the T851 temper and the solution heat-treated base material are shown in Figure 6.22. The BM was solution heat treated at 535°C for 60 min and quenched in water to RT in order to obtain an SSSS prior to DSC analysis.

Solution heat-treated base material

The solution heat-treated sample shows an exothermic peak (peak A) at 75°C associated with GP(I) zone formation. Previously formed GP(I) zones dissolve completely at 156°C (peak B), and θ' forms at 327°C (peak D) without any indication of precursor θ'' formation. Papazian [79] reported that θ'' formation is a not required transitional step in the aging sequence and is consistent with the concept of θ'' as an array of GP(I) zones that evolve slowly during long-term aging. During the relatively rapid heating of the DSC run (10 K/min), θ'' formation does not occur. Papazian [79], for example, reported the occurrence of θ'' formation only at aging times above 15 min at 190°C.

Above 370°C, a large endothermic dissolution reaction occurs, including dissolution peaks E and G and the superimposed formation reaction in peak F. The reaction in peak E at 440°C is related to θ' dissolution. At 470°C (peak F), the equilibrium θ phase forms, and above 486°C, the dissolution of all previously formed phases occurs. [79]

The precipitation sequence of the base material is in agreement with the generally accepted sequence except for the absence of θ'' formation, which does not occur during the DSC thermal cycle.

As-received base material

In the as-received base material, no reaction is observed below 200°C, indicating that the BM contained no significant amounts of GP(I) zones or particles capable of GP(I) zone formation. The endothermic dissolution reaction at 230°C (peak C) indicates the dissolution of θ'' precipitates that were formed during the artificial aging treatment (T851 temper). Slight θ' formation occurs at 270°C (peak D), and θ formation occurs at 454°C (peak F). The shift in the θ and θ' formation peaks to lower temperatures compared to the solution heat-treated base material was reported previously and is related to prior deformation during heat treatment (T851). It is assumed to be caused by the effect of dislocations on the reaction kinetics [79].

The DSC curve indicates that the as-received base material consisted mainly of θ' with low amounts of θ'' that dissolved and re-precipitated as θ' during the DSC run.

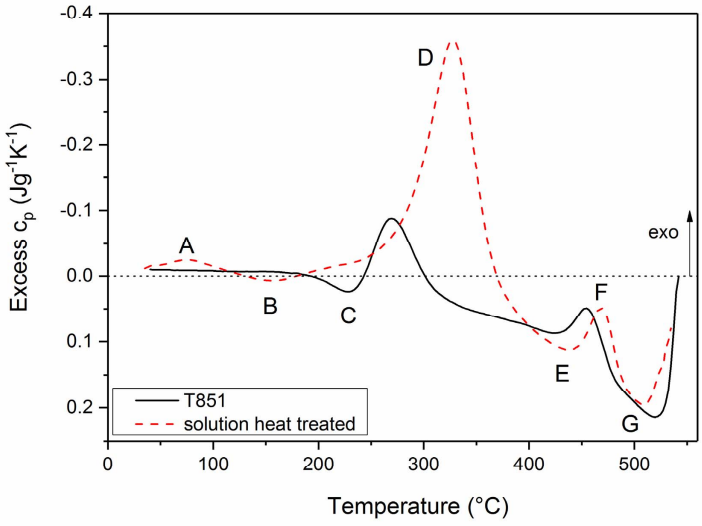

Figure 6.22 DSC curves of AA 2219-T851 in the as-received and solution heat-treated conditions. [105]

Weld zones

Analysis of the precipitation behavior of 2xxx series alloys exposed to thermal cycles of various friction welding processes can be found in the literature. Several works [5, 67, 134] performed FSW in AA 2219-T6, and in each case, some precipitates present in the BM were reported to evolve into equilibrium phases, whereas others dissolved in both the SZ and TMAZ. Feng et al. [70] reported peak temperatures of 450°C in the SZ and 400-450°C in the TMAZ. The level of dissolution was reported to be higher in the SZ. In the HAZ, at peak temperatures below 400°C, only coarsening of the θ' phase was observed. Kang et al. [24] performed FSW in AA 2219-T8 and found similar results but misinterpreted the DSC curves as indicating complete dissolution of θ'' and θ' and partial dissolution of θ in the SZ, complete dissolution of θ'' and θ' in the TMAZ and complete θ'' and partial θ' dissolution in the HAZ. However, the typical thermal cycles during FSW exhibit lower

heating and cooling rates than those during RFSSW, leading to longer exposure to higher temperatures. Very similar results have been reported for the precipitation evolution in the high-temperature frictional zone of friction plug welded AA 2219-T87 [69]. In one study, the authors found coarse θ in the SZ instead of the initial θ' phases and assumed that the majority of particles evolved into θ instead of dissolving, as post-process artificial aging did not improve the strength [135]. However, the thermal cycles leading to these changes in precipitation morphology were not reported.

Shercliff et al. [136] applied the softening model of [129] to AlCu(Mg) alloys to predict microstructural changes in FSW. The model predicts the softening of peak-aged AA 2014 based on the assumption of a single mechanism that is the kinetics of precipitate dissolution. Although the precipitation evolution was not analyzed in detail, the results of the isothermal salt bath tests used to validate the model can be transferred to the AA 2219 used in this study. Below 350°C, no dissolution was observed, and softening is purely due to overaging, as no subsequent natural aging occurred.

The DSC curves of samples taken from the respective weld zones after complete post-weld natural aging are shown in Figure 6.23. The samples are taken from 6 mm-thick sheets welded using a medium size tool at a 1350 rpm rotational speed and 0.6 mm/s plunge and retract speeds.

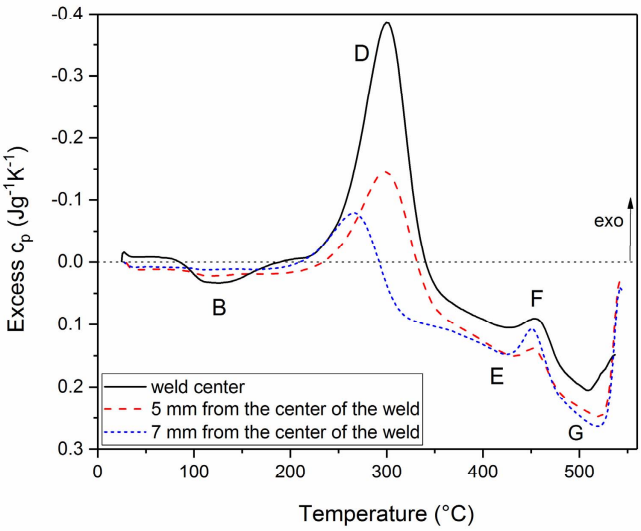

Figure 6.23 DSC curves of the SZ and HAZ at 5 and 7 mm from the center of the weld in 6 mm sheets of AA 2219-T851 welded using the medium size tool. [105]

Stirred zone

The weld center experiences peak temperatures of 546°C during the welding process with very high heating and cooling rates. The DSC curve of a sample taken from the weld center is shown in Figure 6.23. Except for the absence of peak A, all the following peaks appear similar to those in the curve of the solution heat-treated base material. Most of the strengthening precipitates dissolve during the weld thermal cycle, leading to the presence of a large amount of solute in the solution in the as-welded condition. During subsequent natural aging, GP(I) zones form, which dissolve during the

DSC analysis, as seen in the endothermic reaction denoted by peak B. The decreased size of θ phase formation (peak F) compared to the BM indicates that some equilibrium phases have formed.

The SZ of AA 2219-T6 after RFSSW therefore consists mainly of large amounts of solute in the solution, allowing post-weld natural aging as well as some equilibrium θ precipitates. The equilibrium phases formed either during the weld process or during the cooling phase following the weld.

At 5 mm from the center of the weld

The base material experiences high peak temperatures during RFSSW at 5 mm from the center of the weld. Based on the measurements shown in Chapter 5.2 and 6.4.1 as well as in Appendix B, the peak temperature is estimated to be close to 500°C, as the position of interest is very close to the SZ. The heating and cooling rates are assumed to be slightly lower than those in the measurement of the weld center.

The red DSC curve in Figure 6.23 indicates similar precipitation characteristics as the SZ, albeit with less dissolution during welding. The small dissolution peak (B) appears in the DSC curves, indicating that some dissolution occurs during welding, leading to re-precipitation of the GP(I) zones during post-weld natural aging. The absence of dissolution peak C indicates that most θ'' precipitates have dissolved or evolved during welding. Based on the relatively small amount of GP(I) zone dissolution, it is assumed that smaller particles dissolve, whereas the majority of the particles evolved.

Compared to the SZ, peak D was observed to be smaller, indicating a significantly lower amount of particles present for θ' formation. Because of the lower heating rate, it is assumed that most of the preexisting θ' precipitates coarsen and evolve instead of dissolving as seen in the SZ. Similar to the SZ, the size of the θ phase formation peak decreased compared to that of the BM, indicating that some equilibrium phases have formed at this position during RFSSW.

At 5 mm from the center of the weld, some solute was present in the solution in the as-welded condition, leading to the re-precipitation of GP zones during post-weld natural aging. Additionally, the strengthening precipitates coarsen and evolve into the equilibrium θ phase during welding.

At 7 mm from the center of the weld

At 7 mm from the center of the weld, the thermal cycle exhibits lower heating and cooling rates than in the weld center and peak temperatures above 396°C; compare values reported in Chapter 6.4.1.

The DSC thermogram is shown in Figure 6.23. The absence of the dissolution reaction denoted by peak B indicates that no significant amount of solute was present in the solution in the as-welded condition. No precipitate dissolution occurred during the welding thermal cycle. The absence of peak C indicates that most θ'' particles evolved during the weld. Further away from the center of the weld, θ'' particles withstand the thermal cycle, in accordance with the findings of [24]. The small θ' formation peak (D) indicates that a significant volume fraction of the θ' phase was already present in the as-welded condition. The subsequent equilibrium phase formation peak (F) is more pronounced than those in the other regions, indicating that no θ formation occurred during the welding process. No equilibrium phases were assumed to form in this region, as the peak temperature is below the formation temperature.

At 7 mm from the center of the weld, mainly overaged θ' particles were formed, and no dissolution occurred. The strength loss in this region is caused by the coarsening of strengthening precipitates.

6.4.3 Mechanical properties

Microhardness

The microhardness distribution over the cross-section at mid-height at different durations of post-weld natural aging is presented in Figure 6.24 for 6 mm-thick sheets of AA 2219-T851 welded using the medium size tool. The welds show a narrow W-shape hardness distribution with the region of lowest hardness in the TMAZ. The region of lowest hardness is closer to the center of the weld than those in the other two alloys of interest. On average, the region of lowest hardness was measured at approximately 5 mm from the center of the weld in 3 and 6 mm-thick sheets. The thermal cycle at 9 mm from the center of the weld in the HAZ shown in Figure 8.4 thus is not responsible for the highest strength reduction as in the other two alloys of interest.

For the welds in 6 mm-thick sheets shown, the as-welded hardness in the SZ and in the region of lowest hardness is approximately 43 % and 49 % lower than that in the BM, respectively. During post-weld natural aging, the hardness increases mainly in the SZ, reaching 93 $HV_{0.2}$ in the SZ and 80 $HV_{0.2}$ in the areas of lowest hardness on average. These values are 33 % and 43 % lower than those in the BM, respectively.

Influence of sheet thickness

Decreasing the sheet thickness was found to not significantly influence the average hardness values. Welding using the medium size tool in 3 mm-thick sheets yields an average hardness of 97 $HV_{0.2}$ in the SZ and 80 $HV_{0.2}$ in the regions of lowest hardness.

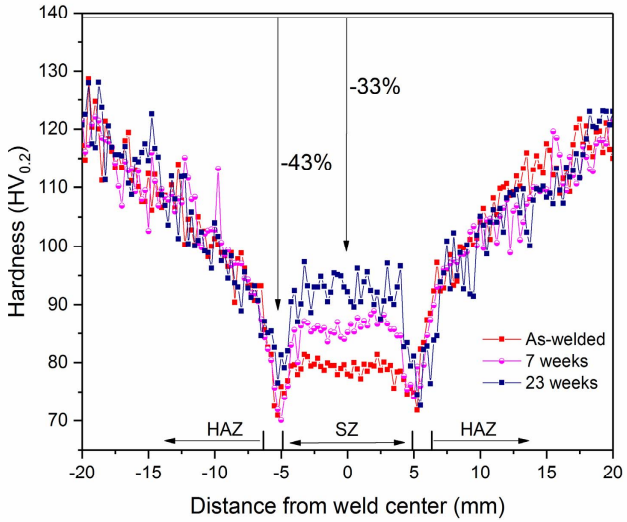

Figure 6.24 Hardness profile of the RFSSW keyhole repair weld in AA 2219-T851 at different post-weld natural aging durations welded at a 1350 rpm rotational speed and 0.6 mm/s sleeve plunge and retract speeds. [105]

Analysis of tensile characteristics

Representative stress-strain curves of keyhole repair welds using RFSSW in AA 2219-T851 are presented in Figure 6.25. Under monotonic uniaxial loading, the welded spots display characteristic behavior, exhibiting one typical fracture mode. Welded coupons fractured in the outer regions of the SZ. The elongation is limited because of the strain concentration in and around the weld spot compared to the BM, as described in Chapter 5.3.3.

Influence of sheet thickness

The sheet thickness was found to slightly influence the tensile characteristic of the welded coupons, Figure 6.25. In 6 mm-thick sheets, samples welded with the medium size tool begin to yield at 191 MPa (54 % of the BM YS), and the UTS is 339 MPa (75 % of the BM UTS). Decreasing the sheet thickness increases the YS, whereas the UTS is similar. In 3 mm-thick sheets, the average YS is 213 MPa (60 % of the BM YS), and the UTS is 325 MPa (72 % of the BM UTS).

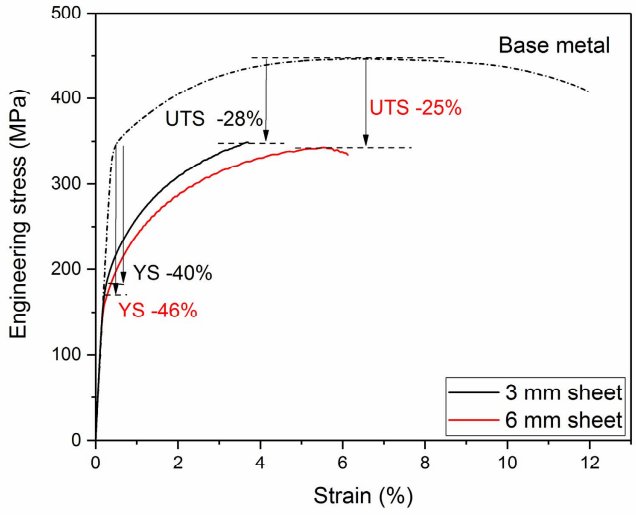

Figure 6.25 Comparison of stress-strain curves of keyhole repair welds to those of the BM in 3 and 6 mm-thick sheets of AA 2219-T851 welded using the medium size tool at a 1350 rpm rotational speed and 0.6 mm/s sleeve plunge and retract speeds. [105]

6.4.4 Discussion

In AA 2219-T8, the weld thermal cycle caused mainly dissolution and minor equilibrium phase formation in the SZ. In the HAZ, overaging of the strengthening precipitates dominates with minor dissolution and equilibrium phase formation only in areas in direct proximity to the SZ. In the region of lowest strength, very little dissolution occurred, and mainly overaging effects were found to decrease the strength. Consequently, very little increase in hardness during post-weld natural aging was observed at this position, and no increase in hardness was found in regions further from the center of the weld.

The typical W-shaped hardness distribution is narrow with the position of lowest hardness closer to the SZ than in the other two alloys of interest. In uniaxial tensile testing, welded coupons of AA 2219-T8 start yielding in the regions of lowest strength close to the SZ. As yielding and final fracture occur in very close proximity to the SZ, numerous effects might contribute to the fracture in this region, and separation of the dominant effects is complex. In addition to having the lowest hardness, the area at approximately 5 mm from the center of the weld features a grain size gradient in the SZ, the transition to the TMAZ with significantly larger grains, a steep gradient in local strength and the welded interface. As fracture seems to not be initiated by a plug-workpiece interface remnant, a combination of the effects is assumed to cause the final fracture in this location, most likely dominated by the lowest strength microstructure.

The combination of very little dissolution with overaging effects in the region of lowest hardness does not lead to a significant strength increase during post-weld natural aging. If an optimization of the mechanical properties is desired, decreasing the peak temperatures in the weld zones surrounding the SZ is suggested, as it might suppress the particle dissolution entirely, leading to an increase in strength. In the SZ, on the other hand, an increase in peak temperature or extension of exposure time might dissolve all precipitates, including the equilibrium phases, which is assumed to cause a slight strength increase during post-weld natural aging.

6.5 Summary and conclusions

The three alloys of interest were successfully welded using the developed repair process. For each alloy, a process parameter window resulting in defect-free welds was developed. Within the respective process parameter window, the resulting thermal cycles, microstructural changes and mechanical properties were analyzed.

When the alloys of interest are welded employing the respective process parameters, very similar thermal cycles with characteristically high heating and cooling rates and short exposure times to the highest temperatures were recorded. Microstructural analysis revealed typical microstructural zone formation in the alloys of interest. Larger deformed grains occurred in the lower central parts of the SZ mainly in AA 2219-T8 and AA 7075-T651, indicating partial recrystallization caused by the high plunge depth used during the repair process. Welds in AA 2219-T8 and AA 7075-T651 also featured a highly inhomogeneous grain size distribution in the SZ with a grain size gradient in the peripheral regions and concave shear layer formation. Remnants of the plug-workpiece interface were observed in the lower parts of the SZ in AA 7075-T651, whereas welds in 3 mm-thick sheets of AA 6061-T6 feature typical remnant formation throughout the entire thickness. In contrast to the behavior of AA 7075-T651, the remnants in AA 6061-T6 did not have any influence on the mechanical performance.

The influence of the grain size and dislocation density on the microhardness compensate each other when different weld zones are compared, as discussed in Chapter 5.3.3. The resulting local mechanical properties thus depend mainly on the precipitation morphology in the alloys of interest. For all the alloys of interest, the thermal cycles induced by the RFSSW process employing the respective process parameters caused complete or almost complete particle dissolution in the SZ during the weld. Thus, a large amount of solute is present in the solution in the as-welded condition, causing re-precipitation of strengthening phases during post-weld natural aging. The final microhardness in the SZ is similar to the respective hardness found for the solution heat-treated and

naturally aged (-T4) tempered material. Slight differences are caused by particle precipitation during the cooling phase of the thermal cycle, as observed in AA 7075-T651 and AA 6061-T6, or by particles that formed at high temperatures during the weld process, as proposed for AA 2219-T8.

The typical thermal cycle in the areas surrounding the SZ causes decreasing dissolution of strengthening particles and increasing overaging phenomena with increasing distance from the SZ. Nevertheless, the overaging phenomena weaken with increasing distance from the weld center because both the heating rate and peak temperature decrease. The ratio of overaging to dissolution mechanisms at a certain distance from the weld center depends on the initial precipitation morphology and precipitation evolution kinetics in the different alloys. This distribution and the strength contribution of the different phases determine the resulting local mechanical properties in the different weld zones.

The point of lowest hardness forms typically at the position where the developed precipitation morphology causes the highest decrease in strength compared to the BM. Any position further away from the weld center features a precipitation morphology in which the strength contribution of the less overaged particles exceeds the one in the point of lowest strength. In all the regions closer to the SZ, the strength contribution of the re-precipitated particles during post-weld natural aging is higher. This causes a hardness increase up to the SZ, where the highest amount of particle dissolution occurred during welding and consequently where the highest strength possible due to re-precipitated particles was measured.

A W-shaped microhardness distribution featuring a weld center with a constant medium strength and a position of lowest strength in the HAZ (AA 6061-T6 and AA 7075-T651) or TMAZ (AA 2219-T8) occurred. Welds in AA 2219-T8 feature a narrow hardness distribution, whereas the shape of the hardness distribution in the radial direction for welds in AA 6061-T6 and AA 7075-T651 is similar. The hardness increase during post-weld natural aging in the SZ is significantly higher in AA 6061-T6 with 21 % of the BM hardness than in AA 2219-T8 with 10 % of BM hardness and in AA 7075-T651 with 14 % of the BM hardness. This indicates a high strength contribution of the re-precipitated particles in this alloy. In AA 7075-T651, dissolution phenomena were found far into the HAZ, whereas welds in the other two alloys feature dissolution phenomena in close proximity to the SZ only. This leads to a strength increase during post-weld natural aging in the HAZ in AA 7075-T651 including the region of lowest hardness. In contrast, welds in AA 2219-T8 show no increase in strength in this region. Welded samples of AA 6061-T6 feature a moderate increase in the point of lowest hardness, although only small amounts of solute were present in the solution in the as-welded condition due to the alloy's strong ability to increase its strength by re-precipitation. The strength reductions in and around the SZ differ significantly among the alloys of interest and depend on the final precipitation morphology in the different weld zones, as discussed above.

Yielding in quasi-static testing at RT started in the region of lowest hardness in the HAZ or TMAZ. Fracture occurred at the same position or in the peripheral areas of the SZ. For both AA 6061-T6 and AA 7075-T651, the strength of the welded interface was found to exceed the strength of the region of lowest hardness in the HAZ. Still, welded samples of AA 7075-T651 fractured in the peripheral areas of the SZ. This caused by crack initiation in the plug-workpiece interface remnants found in this alloy. In welded AA 2219-T8, the area of lowest hardness is located very close to the SZ, and the analysis of the effects leading to failure is complex.

The influence of the process parameters on the mechanical properties was analyzed in AA 6061-T6 and AA 7075-T651. No significant variation in the hardness, YS or UTS was found in either alloy. The position of the point of lowest strength in the HAZ was found to vary with different heat input rates for both alloys, causing similar values of strength and hardness at slightly different positions. Similar results were reported in the work of Pieta et al. [99] for conventional RFSSW of AA 2198-T8.

The discussed precipitate evolution in the alloys of interest demonstrates the essential difference in the thermal cycles of the repair welds compared to thermal cycles that feature long exposure times at a constant temperature. The thermal cycles must be analyzed regarding the peak temperature, the heating/cooling rates and the exposure time to elevated temperature to assess the thermal impact on the observed microstructure. If only the peak temperature was considered, then the precipitate evolution kinetics are neglected, resulting in fundamentally different results. The difference between the microstructural evolution induced by thermal cycles involving long exposure at constant temperatures and that induced by the thermal cycles associated with friction welding processes is discussed in Chapter 7.4.2 for the alloys of interest.

Process optimization

Tailoring the heat input characteristics to the desired profile of mechanical properties is the only option to improve the mechanical properties for a specific application. The thermal cycle experienced by the HAZ or TMAZ can be modified by changing the thermal boundary conditions of the weld to decrease the thermal impact in the areas of lowest strength. Nevertheless, this is assumed to influence the thermal cycle in the weld center as well. Reducing the thermal impact in the weld center will eventually lead to reduced or non-existent dissolution phenomena, which will in turn reduce the final strength in the SZ because of the lower strength increase during post-weld natural aging. An increase in strength in the HAZ might thus be achievable only to the detriment of the SZ strength. Still, for applications such as through-hole repair processes in which large parts of the SZ are removed after the welding process to recover the original geometry, this improvement strategy might be worth considering.

In AA 6061-T6, the discussed repair process using RFSSW is sufficient to produce efficient welds with fractures solely in the HAZ far from the weld center. In the other two alloys of interest, fractures also occurred in the peripheral regions of the SZ, as crack initiation points such as plug-workpiece interface remnants or surface imprints from the sleeve occur in this zone. This was found to decrease the UTS of the respective coupons. Strengthening of the welded interface is assumed to increase the final toughness. For this, a different RFSSW process with force control instead of position control during the second part of the welding process might be of advantage. If the probe moves downwards in a force-controlled mode, pressing the sleeve upwards instead of using self-performed sleeve movement might increase the pressure at the welded interface significantly, resulting in a stronger welded interface.

7 Material behavior during high-shear-rate plastic deformation

7.1 Introduction

In friction welding processes like RFSSW or FSW, a rotating tool introduces frictional heat to a workpiece. The temperature increase due to frictional heat input softens the workpiece material, whereas the movement of the tool causes material flow.

During RFSSW of the alloys investigated in this work, different levels of energy input were assumed, mainly because of the observation of significant thermal cycle differences; for example, see Chapters 5.1 and 5.2. The energy input and the peak temperatures in the HAZ in AA 6061 were found to be higher than those in AA 2219, which in turn are higher than those in AA 7075 when employing the same process parameters. The thermal cycle causes precipitation evolution in and around the weld spot, leading to a reduction in mechanical properties. This is mainly caused by the peak-aged initial condition of the alloys and cannot be avoided. As the alloys of interest exhibit different material properties, they react differently when exposed to friction welding conditions. This results in the utilization of different process parameter ranges for different alloys to obtain the desired mechanical response in the respective alloys.

Understanding the friction condition during welding and the base material behavior during plastic deformation at high temperatures and high strain rates is key for developing an understanding of the underlying mechanisms that yield significant advantages in terms of weld process optimization and mechanical property improvements. Until now, how the energy input and the resulting thermal cycle are affected by material properties in RFSSW has been uncertain. Furthermore, which common features can be seen as boundary conditions during RFSSW and which in turn directly influences the energy input is not clear. Different energy inputs for different aluminum alloys have been reported before for other friction welding processes, for example, by Jonckheere et al. [137] for FSW. A higher heat input in AA 6061-T6 than in AA 2014-T6 was reported. The cause was assumed to be related to material strength differences in the weld zone, but no further analysis was conducted. Similarly, Yang et al. [138] reported higher torque and hence heat input in AA 6061-T6 than in AA 2219-T851 during friction stir spot welding but did not investigate this phenomenon further.

During the RFSSW process, large parts of the frictional resistance originate from the mutual friction of the tool parts. The probe, sleeve and clamping ring are indirectly connected by material from previous welds that fills the cavities between the tool parts. Therefore, force and torque can be transmitted between them. The measurement of process parameters is thus highly influenced by the aluminum intrusion level of the tool. As discussed in Chapter 5.1, measuring the effect of the base material on the force and torque is remarkably difficult. Additionally, it is unclear at which position the frictional resistance is dominant, as the front surface of the tool parts and the outer/inner surface of the sleeve are in contact with the base material. An easy and reproducible setup is needed to study the behavior of individual alloys under conditions similar to RFSSW.

Solid-state friction welding experiments performed to investigate the friction conditions and plastic behavior of the alloys of interest under conditions similar to RFSSW are presented in this chapter. The aim is to investigate the influence of alloying elements and material properties on metallurgical reactions during friction welding and the resulting energy input. Additionally, a deeper understanding

of the underlying friction condition in the tool-steel/aluminum interface is developed. Furthermore, this might support the understanding of the general process parameter–alloy relationship and rapid process optimization by guiding the appropriate choice of processing parameters for a given alloy.

For this, the three alloys of interest have been examined using simple and reproducible friction experiments. From microstructural observations and process monitoring, the material behavior during plastic deformation is analyzed. The energy input and the friction conditions are analyzed by observing the shear stress development during the experiments. These results are used to develop a general systematization of the alloy-dependent behavior for the conditions experienced in friction welding.

Shear stress due to friction

Many models for the shear stress due to friction at the interface of two contacting bodies exist. At low applied pressures, the contact condition is often described by the Amonton-Coulomb friction law, which relates the shear stress τ linearly to the applied contact pressure p using a friction coefficient μ:

$$\tau = \mu p \tag{7}$$

The model assumes that two contacting surfaces touch only at their highest asperities, creating a load-carrying contact area that is smaller than the apparent area of contact. For sliding motion between the contacting surfaces, the material of the contacting asperities has to be sheared off. The force needed to shear off the material is proportional to the shear strength of the softer material and the size of the junctions. Coulomb's friction model assumes that the load-carrying area increases proportionally with the load [139].

It has been suggested that Coulomb's friction model controls the interface stresses at low loads. As loads grow to the point where the real area of contact is equal to the apparent area of contact, the shear stress becomes independent of pressure. At higher pressures, the Tresca friction model is often used to model metal forming processes, relating the shear stress due to friction τ to the yield stress of the deformed material in pure shear k using a friction factor m to avoid overestimation of the friction stress [140]:

$$\tau = mk \tag{8}$$

where $0 \leq m \leq 1$. At $m = 1$, full sticking between the surfaces of the friction partners occurs. The shear stress is equal to the flow stress of the material in pure shear in this condition. A combination of the two models was suggested by Orowan [141]. Wanheim and Bay [142] reported that the real area of contact no longer increases proportionally to the pressure at relatively high contact pressures. They introduced a friction model that provides a smooth transition between a shear stress that is proportional to the load at low pressures and proportional to the material strength at high pressures. They suggested that the Coulomb friction law is valid up to $^{p}/_{k} = 2.6$. At higher pressures, the coefficient of friction becomes pressure dependent and is therefore meaningless. Figure 7.1 summarizes shear stress development over pressure for the mentioned friction models.

The limit for sticking friction to occur between contacting surfaces of tool steel and AA 6060 was analyzed by Wideroe and Welo [139] at elevated temperatures. They reported that sticking friction

condition occurs at a much lower ratio of pressure to material shear strength. For an aluminum disc under shear and compression, the $^{p}/_{\tau_{nom}}$ limit for sticking condition was reported as 0.6 for temperatures above 300°C compared to 0.7 for 250°C.

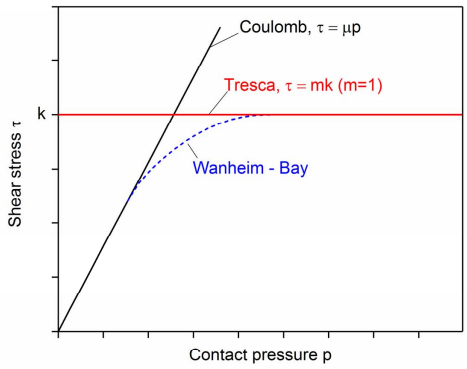

Figure 7.1 The Coulomb, Tresca and Wanheim-Bay friction models.

In friction welding, determination of the contact condition of the workpiece and welding tool is a major issue. Both results supporting and contradicting the assumption of sticking friction have been reported for various friction welding techniques and similar processes.

Buffa et al. [143] found sticking friction above 350°C during linear friction welding of similar AA 2011-T3 in a pressure range from 13 to 30 MPa. For an aluminum extrusion process employing AA 6063, which shows similarities in friction welding regarding material conditions, Ma et al. [144] concluded that both sticking and slipping friction are present simultaneously. The friction condition was reported to be dependent on the contact pressure at different parts of the bearing channel.

Long et al. [145] performed FSW of AA 5082-O, AA 2219-T87 and AA 7050-T7 but found the flow stress not to be consistent with the assumption of both the sticking friction condition and complete solid-state processing at higher rotational speeds. Schmidt et al. [146] attempted to assess whether sticking, slipping or both occur at the tool-workpiece interface during FSW of AA 2024-T3 at 400 rpm and a welding speed of 120 mm/min. They reported that the heat generation and torque are nearly constant during the dwell and weld period and concluded that sticking or close to sticking contact condition must be present. Liechty and Webb [147] concluded that both sticking at higher contact pressures and sliding at lower contact pressures might occur in FSW, as a model containing both friction conditions appeared to predict the welding results much better than a pure stick model for FSW using plasticine as the workpiece.

The use of different alloys, initial conditions, pressures and temperature ranges in studies analyzing the friction condition in friction welding or similar processes makes it difficult to predict the friction condition and behavior for the alloys and boundary conditions used in this work.

To model friction welding processes, a common simplification is to employ a constant friction coefficient. Often, $\mu = 0.5$ is used to model the friction between steel and aluminum, for example, by Essa et al. [148] and Midling and Grong [149]. Frigaard et al. [150] employed a constant friction

coefficient of 0.4 for modeling FSW of AA 6082-T6 and AA 7108-T79. Zhao et al. [64] utilized a friction coefficient of 0.32 below 475°C and employed a linear decrease to 0 above that temperature to account for the expected incipient melting to simulate RFSSW of AA 7075. As solid-state welding is a highly dynamic process with many process parameters, whether the utilization of a constant friction coefficient is satisfactory for aluminum alloys processed under the boundary conditions of interest must be analyzed.

7.2 Experimental setup and procedure

The friction experiments were performed using a tool consisting of only a probe and a clamping ring, Figure 7.2. A three–step sequence was applied. The clamping ring is deployed to apply pressure on the workpiece in the initial step as the retracted probe accelerates to a pre-set rotational speed. The measurements of the friction phase begin when the probe reaches the surface of the sheet. The friction phase was set to 4 s, during which the probe was set to rotate at a pre-set speed on the surface of the workpiece without transversal movement. After 4 s, the probe was retracted from the surface of the base material, and the measurement was ended. As the front surfaces of the probe and clamping ring were aligned, the probe applies a certain amount of pressure on the workpiece during the friction phase. Applying this setup allows the effects of the workpiece material on the force and torque to be analyzed because the measured values are needed only to rotate the probe at its position on the surface of the workpiece at a constant rotational speed. This configuration was chosen to resemble the RFSSW boundary conditions of shear under compression at elevated temperature.

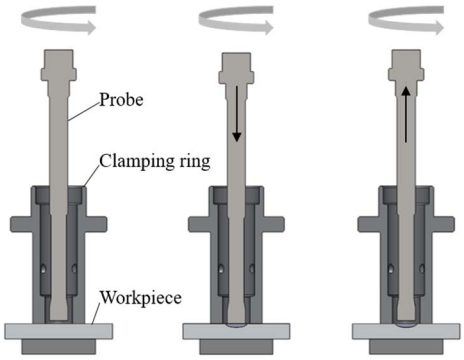

Figure 7.2 Experimental setup to analyze the material behavior during high-shear-rate plastic deformation.

Plates with a thickness of 8 mm of AA 6061-T6, AA 2219-T851 and AA 7075-T651 were used as the base material. The rotational speed was pre-set at 1500 rpm, and the experiments were conducted employing clamping pressures of 4 kN, 7 kN and 10 kN to analyze the response of the alloys in different pressure ranges. The probe diameter was 8 mm, whereas the clamping ring featured a 12 mm inner and 20 mm outer diameter. The tool was made of molybdenum-vanadium alloyed hot-work tool steel. A total of 54 experiments with a minimum of 3 replicates per set of process parameters were conducted to characterize the material behavior.

A constant torque of $M_{inner} = 8.85 \pm 1.68$ Nm is needed to rotate the probe, including the attached parts of the welding equipment, at 1500 rpm without contacting any workpiece in the abovementioned setup. Hence, to exclusively measure the torque caused by frictional resistance at

the tool-workpiece interface, the torque was determined by subtracting 8.85 Nm from the measured value.

It is relatively difficult to measure the temperature close to the rotating tool during friction welding operations. The most effective means of measuring the temperature is by inserting the thermocouples within the tool itself. However, even if this method would be employed, the measured values would be lower than the actual temperature at the contact interface of the tool and workpiece [151]. As a direct tool temperature measurement was not possible with the welding equipment used, K-type thermocouples were embedded in the aluminum plates to record the thermal cycle in the frictional interface. The thermocouples were inserted from the lower part of the plate and positioned as close as possible to the upper surface in the weld center while maintaining a thin layer of aluminum between the thermocouple and rotating probe. As displacement of the thermocouple caused by the material flow constantly affected the measurement, measurements of the material that was extruded from the SZ were simultaneously conducted using an infrared thermographic camera to confirm the measured values.

7.3 Experimental results

The basic results of the friction experiments are expected to resemble the RFSSW characteristics, as the experimental procedure was chosen to obtain similar conditions in the SZ of the base material as in RFSSW. Consequently, it is expected that the differences between the alloys of interest in terms of characteristic microstructural features or energy input remain comparable to those in RFSSW.

Figure 7.3 shows the typical surface appearance after the friction experiments. The probe extrudes some workpiece material from the friction zone, which then forms a characteristic ring on the surface. The clamping ring leaves a visible mark on the surface of the workpieces but was not found to deform the material plastically.

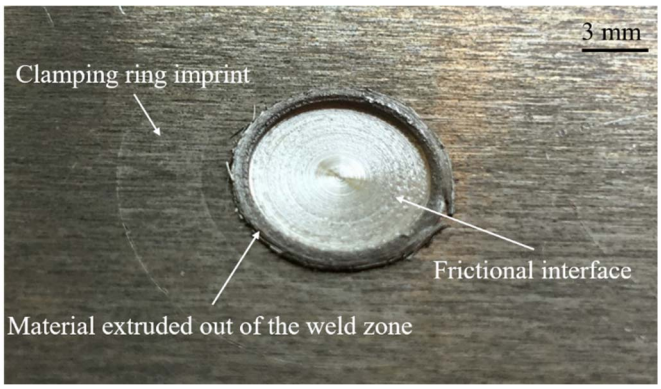

Figure 7.3 Typical surface appearance in AA 7075-T651 after the friction experiments.

In all tested cases, the probe front surface was covered in aluminum after the experiment. It is believed that the oxide layer on the surface of the sheet was broken up in the beginning of the experiment, enabling oxide-free aluminum to come in contact with the tool steel surface and creating a strong contact.

7.3.1 Microstructural features

The hard asperities of the tool plunge into the relatively soft aluminum. The constant rotation of the probe introduces shear stress into the workpiece. The shear stress transmitted into the workpiece is related to either the pressure if sliding friction occurred or the material strength if sticking friction occurred. As soon as the local yield stress is exceeded, the base material underneath the probe starts to deform plastically. The increased deformation and elevated temperature yield recrystallization processes, forming a typical SZ exhibiting small grains. Figure 7.4 (a) shows a typical cross-section in AA 7075-T651 after the friction experiments. The typical weld zones of friction welding processes include a SZ surrounded by a TMAZ that in turn is surrounded by a HAZ without plastic deformation. The SZ features typically a W-shape that is defined by the characteristic of the TMAZ. The depth of the SZ midway from the center of the weld to the outer boundary of the SZ was measured at 916 µm for AA 6061, 742 µm for AA 7075 and 547 µm for AA 2219. The clamping pressure was found to have no influence on the SZ depth. A higher clamping pressure in the beginning of the experiments results in more material extrusion from the SZ, which reduces the pressure. This effect leads to the similar SZ depths obtained at the end of the experiments conducted with different clamping pressures. The TMAZ is thin in the outer regions, Figure 7.4 (A), and thickens towards the center, where it reaches its largest diameter, Figure 7.4 (B). The depth of the TMAZ in the weld center was measured at 273 ± 17 µm for AA 7075, at 173 ± 16 µm for AA 2219 and at 113 ± 6 µm for AA 6061.

Figure 7.4 (C) shows a characteristic processed region, as observed in the friction experiments. A gap appears between the protruding material that was extruded from the frictional interface and the beginning of the SZ. This gap is assumed to be formed by eccentric rotation of the probe, which is not supported by a sleeve in these experiments. This gap appears in AA 7075, Figure 7.4 (a), and in AA 2219 but not in AA 6061, Figure 7.4 (C).

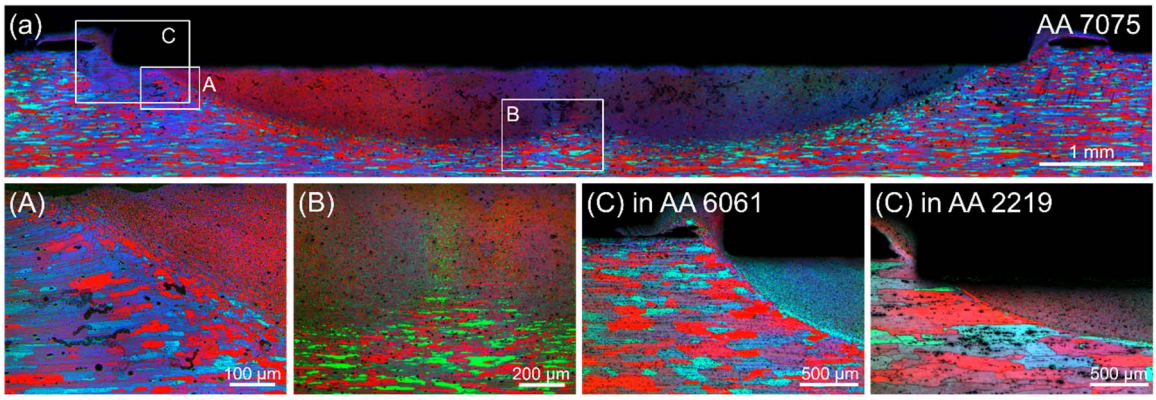

Figure 7.4 Low-magnification overview of a typical sample processed at a 7 kN initial clamping pressure (a) and magnified views of regions (A), (B) and region (C) for AA 6061 and AA 2219

A reasonable comparison of the recrystallization behavior of the alloys was not within the scope of the experiments discussed in this chapter. The base material will deform plastically if the strength is exceeded by the stress at a certain position. Higher strain will lead to recrystallization, whereas areas of lower strain form the TMAZ. The temperature distribution in the workpiece is unknown, and the amount of shear stress that is transmitted in the viscous SZ during the friction phase is uncertain. Therefore, the material strength as well as the stress state at the interface between deformed and non-

deformed material is uncertain. A sole increase in temperature, for example, would lead to an increase in the amount of plastically deformed material, as the material's strength would be reduced, assuming that the shear stress transmission in the viscous material does not change. The measured shear stress during sticking friction would simultaneously be reduced because of the reduction in the material flow stress. This would lead to reduced shear stress while deforming a higher volume of material. The shear stress measured in the frictional interface is representative of the pressure if sliding friction appears or of the material's flow stress if sticking friction predominates. It cannot be used as a measure of the volume of flowing material underneath the probe. The size of the recrystallized zone is an alloy-dependent effect of the boundary conditions of the experiments. Conclusions drawn from comparing the size of the zones to the respective alloy's strength are not reasonable, as the temperature distribution and the shear stress transmitted in the viscous SZ are not known.

Estimated shear rate

If it is assumed that a sticking condition exists at the contact interface between the tool and workpiece and that the material flow velocity features a quadratic regime, then the shear strain rate decreases linearly with increasing distance from the tool. For this, the strain rate midway across a 900 µm SZ under the probe (for AA 6061, see above) midway across the 8 mm diameter tool should be approximately 350 s^{-1}. For the smaller stirred zones in the other two alloys, the strain rate midway across the tool and respective SZ should be approximately 408 s^{-1} (AA 7075) and 571 s^{-1} (AA 2219).

7.3.2 Process monitoring

Typical force and torque development and the typical thermal cycle during the conducted experiments are shown in Figure 7.5 (a) and (b) for AA 7075-T651. Both the force and torque show a strong increase during initial contact between the tool and base material followed by a steady decrease during the friction phase. The torque correction (see section 7.2) decreases the torque values from approximately 15 Nm to approximately 5 Nm.

The force measurement represents a boundary condition for shear loading under compression. The decrease in the force indicates that the pressure condition for the material affected by the rotating tool changes. It is assumed that the material loss caused by the extrusion of aluminum to the sides is mainly responsible for the decrease in the force, whereas softening of the workpiece is accounted for in the measurement of the torque.

The typical thermal cycle in Figure 7.5 (b) features a high heating rate of approximately 600°C/s at initial contact between the tool and workpiece in the frictional interface. During the friction phase, the temperature is constant at approximately 400°C. Temperature measurements in the other alloys revealed similar thermal cycle characteristics with similar peak temperature of approximately 400°C. Through the use of an infrared thermographic camera, the temperature of the material extruded from the tool-workpiece interface to the sides was measured at slightly higher temperatures with similar characteristics. Similar to the measurement of the thermal cycle in the SZ during RFSSW, no trend in peak temperatures was measured. It is therefore assumed that the temperature during the experiments in the frictional interface was constant at approximately 400°C or slightly higher with the peak temperature attained in less than half a second.

The rapid increase in the interface temperature followed by an almost constant temperature during the friction phase sets the constant temperature as a boundary condition of the measurements during

the friction phase. The cooling phase starts with the retraction of the rotating probe and is therefore not included in the analysis of the friction phase.

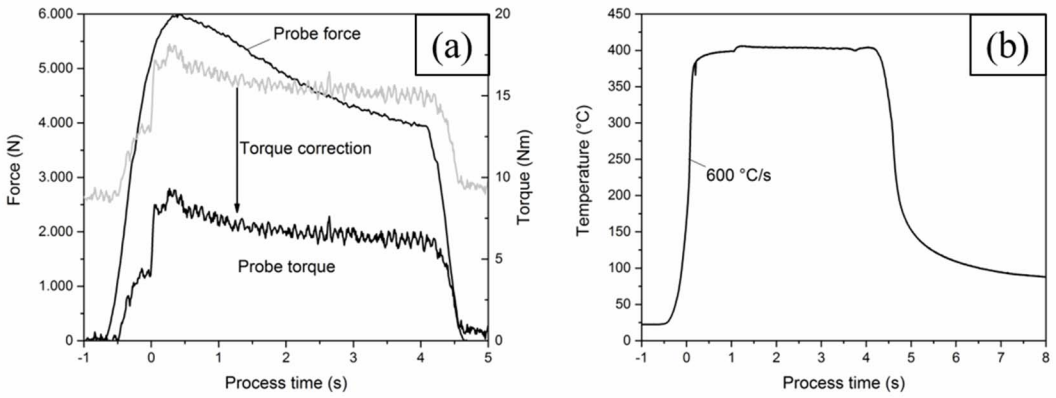

Figure 7.5 Typical torque and force development (a) and the typical thermal cycle (b) in AA 7075-T651 during frictional experiments with a 7 kN initial clamping force.

The energy input for the experiments was calculated by applying the same method as for the welds using RFSSW; see Chapter 4.1.4. As the probe rotates only at the surface of the aluminum sheet without any transversal movement in this experiment, the force part of Equation (2) does not contribute to the calculated energy input.

The energy input is highest in AA 6061-T6, followed by AA 2219-T851 and AA 7075-T651, Figure 7.6. As differences in the measured values are solely caused by the different base materials in this setup, this observation confirms the assumption of similar conditions in RFSSW discussed in Chapter 5.2. The higher energy input can be attributed to different torque levels in the alloys of interest. Additionally, a trend of increasing energy input with increasing clamping force can be observed.

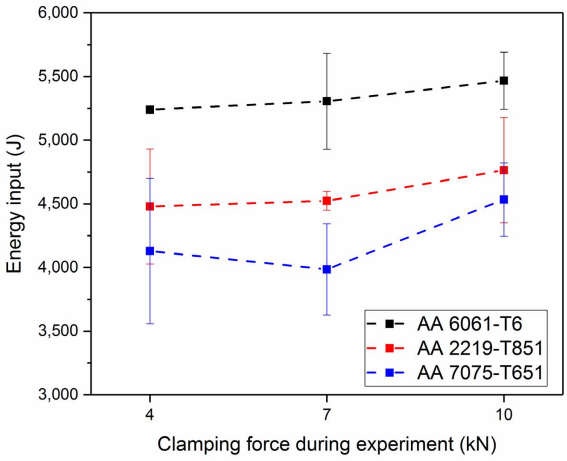

Figure 7.6 Applied heat during the experiments conducted at different clamping forces and with different alloys.

7.3.3 Analysis of the shear stress development

The shear stress at the interface of the rotating probe and aluminum sheet's surface is calculated using the torque measurement of the welding equipment. The torque at the interface M can be expressed by integrating the shear stress τ over the front surface of the probe according to:

$$M = \int_{R_i}^{R_o} (\tau r)(2\pi r)\, dr = \frac{2}{3}\pi r^3 \tau\,(r, \theta) \tag{9}$$

The shear strength is expected to be a function of the radius r and the rotation angle θ, as shown by Stelt [84]. This dependency can be neglected by assuming that a uniform nominal shear stress τ_{nom} occurred, which represents the average shear stresses at the interface. The nominal shear stress can be expressed using the torque as:

$$\tau_{nom} = \frac{3M}{2\pi r^3} \tag{10}$$

where r = 4 mm is the radius of the probe. The shear stress is related to either the pressure if sliding friction occurred or the material strength if sticking friction occurred. For further analysis of the nominal shear stress, the pressure at the probe-workpiece interface and the flow stress of the material in contact with the tool are assumed to be uniform.

Onset of plastic deformation

At a certain shear stress, the base material will start to deform plastically. Similar to the approach employed by Stelt [84], the onset of plastic deformation can be calculated using the von Mises yield criterion. Plastic deformation starts as soon as the von Mises stress σ_{VM} surpasses the yield stress. For a compressed disc under torsion, the yield criterion holds:

$$\sigma_{VM}^2 = p^2 + 3\tau^2 \tag{11}$$

The shear stress τ_{YS} required for plastic deformation can be obtained by substitution of the yield stress into the von Mises yield criterion:

$$\tau_{YS} = \sqrt{\frac{\sigma_{YS}^2 - p^2}{3}} \tag{12}$$

This equation is used to estimate the approximate onset of plastic deformation underneath the rotating probe knowing that the stress state is not in agreement with an ideal compressed disc under torsion.

Shear stress development

The rotating probe presses downwards on the surface of the sheet, and shear stresses arise in the workpiece from the friction between the tool and base material. The stress state in the workpiece underneath the probe changes to shear under compression. The torque represents the frictional resistance and can be used to calculate the shear stress in the workpiece using Equation (10). The development of the nominal shear stress at the interface is analyzed in the following paragraphs.

Expected shear stress

If sliding friction occurs, the measured nominal shear stress is expected to be linearly related to the contact pressure for a base material with constant strength, see Figure 7.1. If sticking friction occurs, the shear stress is expected to be constant and independent of the pressure.

Observed shear stress

The measured nominal shear stress as a function of the pressure at the frictional interface is presented in Figure 7.7 for AA 6061-T6, in Figure 7.8 for AA 2219-T851 and in Figure 7.9 for AA 7075-T651. Typical measurements at the three tested clamping pressure levels are shown. As the pressure decreases during the friction phase, the measurements have to be analyzed from the highest to lower pressure values. One second of friction time during the friction phase of the 10 kN – measurement is indicated in Figure 7.8 for orientation.

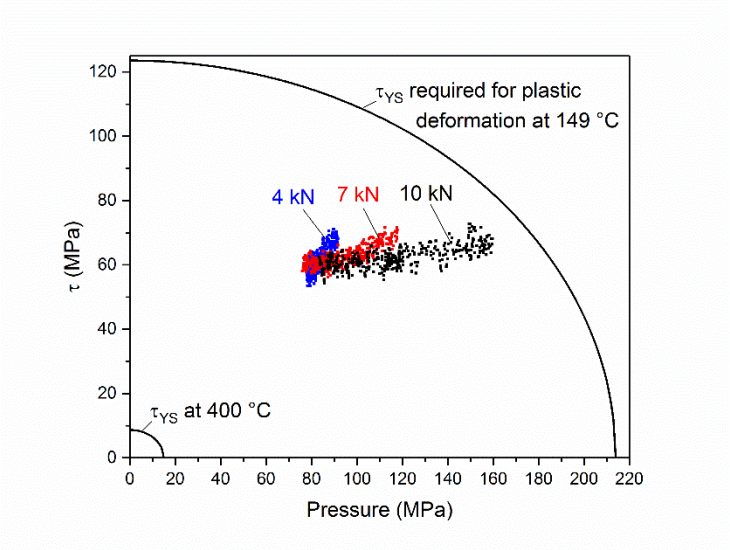

Figure 7.7 Typical shear stress development in AA 6061-T6 for experiments conducted with 4, 7 and 10 kN initial clamping pressure.

The shear stresses occur in a range of 45 to 70 MPa and the pressure varies from approximately 80 to 160 MPa. The shear stress decreases during the friction phase for all alloys, and the clamping pressure levels off. The decrease in the measured nominal shear stress is faster in the beginning of the experiments and flattens towards a constant value with increasing friction time, leading to a curved shape of the shear stress measurements.

The shear stress development for the experiments conducted with different clamping pressure levels shows similar characteristics. More material is pressed out from the SZ to the sides of the probe at higher levels of initial clamping pressure, thereby reducing the pressure underneath the probe. For lower clamping pressure, less material is extruded from the SZ, limiting the decrease in pressure. This results in similar values of pressure with increasing frictional time for experiments with different initial values of clamping pressure.

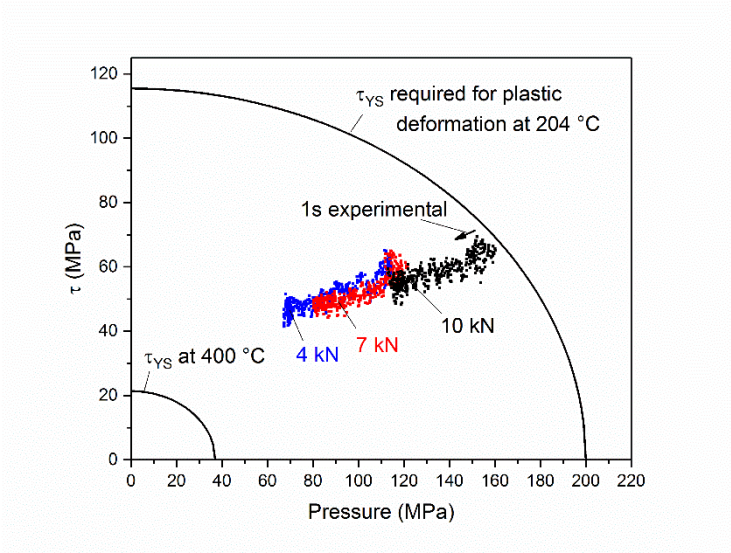

Figure 7.8 Typical shear stress development in AA 2219-T851 for experiments conducted with 4, 7 and 10 kN initial clamping pressure.

The quasi-static yield criterion τ_{YS} for the respective alloys at different temperatures and pressures is indicated in Figure 7.7, Figure 7.8 and Figure 7.9. For example, the yield criterion for AA 6061 at 149°C and 400°C is presented in Figure 7.7. The curved line represents the maximum shear stress expected without plastic deformation at the respective temperature. The yield envelopes for the alloys of interest are calculated using the respective alloy's strength at a certain temperature according to Equation (12) by employing the values of quasi-static YS reported below. These envelopes thus represent the respective alloy's quasi-static strength at elevated temperatures in an equilibrium state. The base material's condition was found to be rather different; a detailed discussion of the different material conditions is given in Chapter 7.4. The yield envelopes are intended to provide an assessment of the order of shear stress during the experiments.

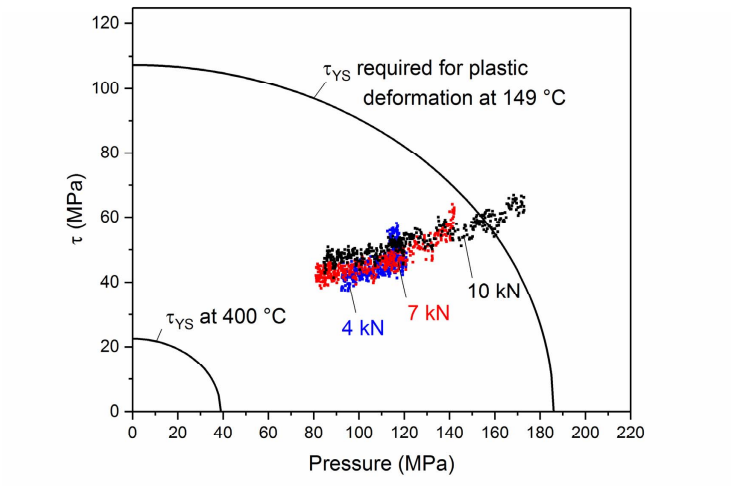

Figure 7.9 Typical shear stress development in AA 7075-T651 for experiments conducted with 4, 7 and 10 kN initial clamping pressure.

The measured nominal shear stresses as a function of the pressure for the three tested alloys are shown in Figure 7.10. The experiments conducted at different initial clamping pressures are averaged to obtain a single curve for each alloy. On average, the measured nominal shear stress decreases from approximately 70 to 60 MPa in AA 6061, from approximately 64 to 46 MPa in AA 2219 and from 64 to 45 MPa in AA 7075. The stronger decreases in shear stress for AA 2219 and AA 7075 indicate stronger softening of these materials during the friction phase than AA 6061. For all pressures, the average flow stress in AA 6061 is higher than that in AA 2219 and is lowest in AA 7075. The typical curved shape approaching a constant value appears. The curvature is reduced by averaging all values over the pressure compared to the shear stress development of the single experiments.

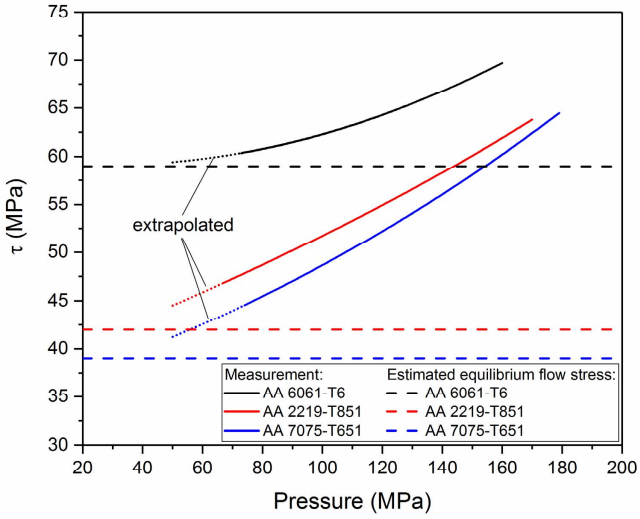

Figure 7.10 Average nominal shear stress pressure diagram for the tested alloys. The solid line represents the averaged measurements, whereas the dashed line represents extrapolation to lower values of pressure.

As the measured shear stress does not show a linear relationship with the pressure, sticking friction seems to occur. This assumption is confirmed by the analysis of the apparent friction coefficient, see below. As the measured nominal shear stress is directly related to the material's flow stress for sticking friction condition, the material's strength seems to approach an equilibrium. This equilibrium flow stress in pure shear would occur if the respective alloy would be exposed to the boundary conditions of the friction phase long enough. For the three tested alloys, the shear stress did not reach a constant level during the four seconds of frictional time. In Figure 7.10, the measured shear stresses are extrapolated to lower levels of pressure to indicate further softening towards the equilibrium strength. From the obtained data, the estimation of the equilibrium flow stress in pure shear is 59 MPa for AA 6061, approximately 42 MPa for AA 2219 and approximately 39 MPa for AA 7075, as indicated in Figure 7.10. The flow stress can be calculated by multiplying the shear strength by $\sqrt{3}$ [145]. This yields an estimated equilibrium flow stress of 102 MPa for AA 6061, 73 MPa for AA 2219 and 68 MPa for AA 7075.

The calculated flow stress values and the order of strength differs significantly from the quasi-static YS of these alloys, which is lowest for AA 6061-T6 at 14.7 MPa, followed by AA 2219-T851 at 37 MPa and AA 7075-T651 at 39 MPa. These values were calculated based on the strength reductions reported by [152] for exposure to 400°C for 0.5 h using the measured BM yield strength at RT (see Chapter 4.2) as a baseline. In AA 6061-T6 and AA 2219-T851, the strength is reported to further decrease to 13.6 MPa and 21 MPa, respectively, when the exposure time increases to 10 h. For AA 7075-T651, no further softening due to longer exposure is reported [152]. The calculated quasi-static YS values are in reasonable accordance with the strength of AA 6061-T6 reported by [153], of AA 2219-T851 reported by [154] and of AA 7075-T651 reported by [155, 156] considering hot deformation employing low strain rates and long holding times at elevated temperature before testing.

The measured shear stress is highest in AA 6061 and lowest in AA 7075 for all pressure levels. This correlates with the applied heat presented above in Figure 7.6. Higher flow stress indicates higher resistance to rotational movement; therefore, higher torque is needed to rotate the probe with the pre-set rotational speed, which increases the energy input. As the friction condition is equal in all three tested alloys, the higher heat input in the order AA 6061 > AA 2219 >AA 7075 is caused by higher flow stress during the friction phase.

Apparent friction coefficient

The apparent friction coefficients for the three tested alloys based on the average shear stress development reported in Figure 7.10 are shown in Figure 7.11. The curvature is slightly reduced because of the averaging, similar to the average shear stress development curves in Figure 7.10. The apparent friction coefficients vary significantly from approximately 0.4 to 0.8. As the friction coefficients are derived from the measured shear stresses and pressures, the values for AA 6061 were already expected to be higher than those for AA 2219 and AA 7075.

The solid curves in Figure 7.11 represent the measured values, whereas the dashed curves represent the apparent friction coefficients that would occur if the alloys exhibited the estimated equilibrium strength during the entire friction phase. With a constant strength during the friction phase, the apparent friction coefficient curve follows a hyperbola. The difference in curvature of the two curves for one alloy is caused by the base material softening towards an equilibrium flow stress during the experiment, as reported above. With increasing frictional time, the measured values approach the equilibrium hyperbola.

Sliding friction would result in a constant friction coefficient. This does not occur in the tested range of the averaged curves and was not observed for single measurements either. Thus, sticking friction occurs in the frictional interface between the rotating probe and base material. Additionally, the measured $^{p}/_{\tau_{nom}}$ values are in the range from 1.3 to 2.6 and thus are significantly higher than the sticking friction limit of 0.6 at temperatures > 300°C reported by Wideroe and Welo [139] for AA 6060/tool steel. A transition to sliding friction cannot be predicted at this point and is assumed to occur suddenly in regions of lower pressure.

As the shear stress equals the flow stress in the observed sticking friction condition, the friction coefficient becomes pressure dependent and meaningless for the description of the shear stress. The reported apparent friction coefficient must be distinguished from the constant friction coefficient in Equation (7).

To model a friction welding process under sticking friction conditions, the base material's velocity close to the tool must be set to the tool's circumferential speed at the respective position. The shear stress in the tool-workpiece interface should represent the material's flow stress at this condition. The commonly used constant friction coefficient is inadequate to simulate the abovementioned friction phase, as it would overestimate the shear stresses at higher pressure levels.

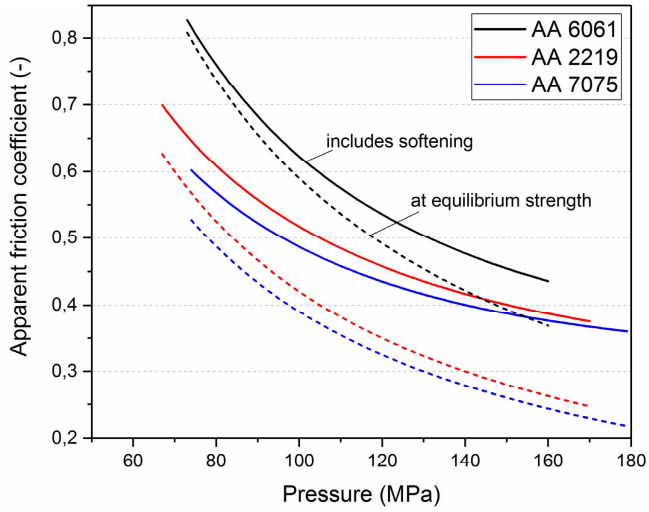

Figure 7.11 Apparent friction coefficient for the tested aluminum alloys. The solid curves represent the measured values, whereas the dashed curves represent the apparent friction coefficient that would occur if the alloys exhibited the estimated equilibrium strength during the entire friction phase.

7.3.4 Summary and conclusions

Different friction experiments employing process parameters and boundary conditions similar to RFSSW were conducted to analyze the material behavior during high-shear-rate plastic deformation and the resulting energy input. Based on the shear stress development during the frictional phase of the experiments, the friction condition was found to be sticking friction in all tested alloys. The measured shear stresses approach a constant value independent of the pressure, which is in agreement with the generally accepted sticking friction models. The calculated apparent friction coefficient is thus approaching a sticking friction hyperbola instead of a constant value, which would indicate a sliding friction condition.

For sticking friction conditions, the measured nominal shear stress equals the flow stress in pure shear of the deformed base material in the experimental setup. Softening of the alloys during the friction phase causes the curvature of the flow stress development towards a constant equilibrium value, which was not reached in the relatively short friction phase for the observed alloys. Similar softening behavior occurs in all the alloys, but the flow stress in AA 6061 was found to be higher than that in AA 2219, which in turn was higher than that in AA 7075 in the tested pressure range. This was not expected, as the order of yield strength is AA 7075-T651 > AA 2219-T8 > AA 6061-T6 at both RT and 400°C under quasi-static testing conditions when employing a low heating rate. Additionally, the

observed flow stresses are significantly higher than the quasi-static YS values of these alloys at similar temperatures.

The energy input is defined and thus limited by the material's flow stress during plastic deformation because the flow stress determines the resistance to the rotational movement of the tool. Increasing the flow stress causes a higher torque to be needed to rotate the tool, which in return increases the energy input. The AA 6061-T6 > AA 2219-T851 > AA 7075-T651 order of the energy input in the experimental setup is caused by the flow stresses following the same order.

7.4 Analysis of the flow stress distribution

In the previous sections of this work, the aluminum alloys of interest were found to soften during the friction phase of the conducted experiments. Furthermore, the flow stress was found to be significantly higher than the quasi-static YS of these alloys at elevated temperatures. The estimated equilibrium flow stresses observed during the frictional experiments and the quasi-static YS at similar temperatures are summarized in Table 7.1; a detailed explanation is given in Chapter 7.3.3. Contrary to the order of quasi-static YS of these alloys at RT and at 400°C, the flow stress during frictional processing was found to follow the sequence AA 6061-T6 > AA 2219-T851 > AA 7075-T651, explaining why the energy input follows the same order.

Table 7.1 Comparison of the estimated equilibrium flow stresses observed during the frictional experiments and the quasi-static YS at 400°C

	AA 6061-T6 (MPa)	AA 2219-T851 (MPa)	AA 7075-T851 (MPa)
Estimated equilibrium flow stress	102	73	68
Quasi-static yield strength	15	37	39

The conditions during the frictional experiments differ substantially from the quasi-static testing conditions employed to generate the yield strength values listed in Table 7.1. During the frictional phase, the thermal cycle features a significantly higher heating rate and shorter exposure times to the peak temperature. Additionally, the shear rates are significantly higher than those during quasi-static testing.

In this chapter, the mechanisms of precipitate evolution, incipient melting and strain rate sensitivity are analyzed in detail to discuss the flow stress observations and to explain the difference to the quasi-static YS of the base materials. The knowledge gained in this fundamental analysis is finally used to draw conclusions for the RFSSW process.

7.4.1 Strain rate sensitivity

For a given aluminum alloy, the flow stress is a function of strain rate, among other factors such as temperature and strain [6, 157-159]. The strain rate sensitivity of aluminum alloys within a wide range of high-strain-rate deformation is a complex multi-mechanism process that has not yet been fully understood, but it was reported to vary significantly from low to high strain rates [160]. For the alloys of interest, the strain rate sensitivity is not relevant at RT but is reported to increase with temperature [6, 157]. Additionally, the ability to work hardening decreases at increasing temperature and increases with the strain rate because of the decrease in the time for restoration processes causing the release of work-hardening factors (e.g., dislocation annihilations). For the alloys of interest, strain

hardening at elevated temperatures was reported to be low compared to deformation at RT [3, 6, 157, 158].

Strain rate-dependent overstress increases the flow stress during the frictional phase of the conducted experiments compared to that under quasi-static testing conditions. Evaluating the overstress caused by the deformation during the frictional phase based on published studies is extremely difficult, as the tested strain rates, base materials, thermal cycles and load conditions are mostly different [3, 6, 157, 158, 161]. To estimate the quasi-static equilibrium flow stress without the velocity-dependent overstress, additional experiments were conducted. The experimental procedure was similar to the one reported in Chapter 7.2, but the probe was not lifted from the surface of the sheet after the frictional phase. Instead, the rotation of the probe was stopped as fast as possible while maintaining the probe at its position pressing on the surface of the sheet. As the reaction force was continuously monitored, the decrease in pressure was used to assess the reduction in the material's strength.

Stopping the rotational movement decreases the strain rate to zero instantaneously, which causes an immediate decrease in the flow stress. Additionally, relaxation and creep processes occur, reducing the work-hardening content continuously. Creep and relaxation curves were found to cross the loading curve for the corresponding plastic material loaded at an infinitely slow strain rate. The remaining difference between the equilibrium after creep or relaxation and the plastic response at a very slow loading rate was reported to increase with increasing overstress applied during loading but remains small for usual structural metals [162].

The decreasing pressure values for the alloys of interest thus represent the degradation of the velocity-dependent overstress with regard to the quasi-static deformation behavior at the same thermal cycle exposure. The velocity-dependent overstress at the end of the frictional phase is assumed to be similar to that under the theoretical equilibrium condition, which is not reached during the experiments. The decrease in probe pressure following the frictional phase can thus be used as an estimate of the difference between the estimated equilibrium flow stress and the estimated quasi-static equilibrium flow stress.

The average force reduction following the frictional phase is shown in Figure 7.12. At least 4 experiments were conducted at a 7 kN initial clamping pressure for each alloy. In the diagram, the timeline starts at the moment when the rotational movement of the probe starts to decrease. The rotation stopped completely in less than 0.3 s. The average pressure at the end of the frictional phase was different for each alloy: 80 MPa for AA 6061-T6, 63 MPa for AA 2219-T851 and 81 MPa for AA 7075-T651. As the magnitude of pressure reduction is relevant, the data were rescaled so that the baseline of 0 MPa indicates the pressure at the beginning of the decrease of the rotational movement for each alloy. Thus, the absolute strength reduction following the end of the rotation is indicated as negative values on the y-axis in Figure 7.12. Interpreting the data requires consideration of the reduction in temperature, which was not monitored for the additional experiments. As heat conduction is a rather sluggish process, it is assumed that for each of the three alloys, the temperature will remain at approximately 400°C for a certain time and then start to decrease continuously.

The pressure decreases similarly in each alloy: the major decrease occurs during the first 5 to 10 s, followed by a relatively low decrease in the subsequent time span. After 30 s, the values of the pressure decrease approach - 22.7 MPa for AA 6061-T6, - 20.8 MPa for AA 2219-T851 and

- 22.5 MPa for AA 7075-T651. These values are expected not to change significantly with additional time, as indicated by the creep curves reported by Huber and Tyulyukovskiy [162].

Anticipating the precipitate evolution of AA 7075-T651 discussed in the subsequent chapter leads to the assumption that almost full dissolution occurs when the equilibrium flow stress is reached after the frictional phase. The estimated quasi-static equilibrium flow stress and the quasi-static YS reported in Table 7.1 are assumed to be similar for AA 7075 because the different thermal cycles cause similar precipitation morphology (complete dissolution) and because the strain hardening ability was reported to be very small at 400°C. The difference between the estimated equilibrium flow stress and the quasi-static YS is thus mainly caused by the strain rate-dependent overstress for AA 7075-T651, which can be estimated by the pressure reduction following the frictional phase.

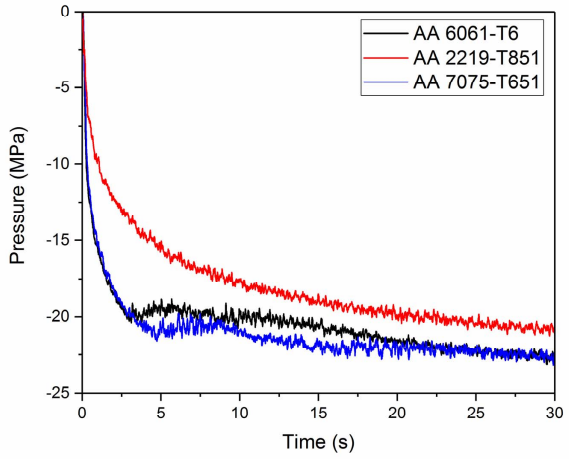

Figure 7.12 Pressure decrease following the frictional phase for the alloys of interest.

As AA 7075-T651 exhibits an estimated equilibrium flow stress of 68 MPa (a detailed description is provided in Chapter 7.3.3), the difference of 29 MPa from the quasi-static YS of 39 MPa can be described by the pressure reduction of 22.3 MPa. The overstress in AA 6061-T6 is thus estimated to be similar to 29 MPa, whereas it is less in AA 2219-T851 because the pressure reduction in this alloy is smaller. This gives an estimated quasi-static equilibrium flow stress of approximately 73 MPa for AA 6061-T6 and approximately 39 MPa for AA 7075-T651. The value for AA 2219-T851 can be predicted to be above 44 MPa. The estimated quasi-static equilibrium flow stresses are summarized and compared to the quasi-static YS in Table 7.2

Table 7.2 Comparison of the estimated quasi-static equilibrium flow stresses observed during the frictional experiments and the quasi-static YS at 400°C.

	AA 6061-T6 (MPa)	**AA 2219-T851 (MPa)**	**AA 7075-T851 (MPa)**
Estimated quasi-static equilibrium flow stress	≈ 73	> 44	≈ 39
Quasi-static yield strength	15	37	39

Summarizing, the higher rate of deformation in the frictional experiments was found to increase the flow stress significantly compared to quasi-static testing conditions. However, the estimated quasi-

static equilibrium flow stress of the base materials, that does not include the overstress caused by higher strain rate, is still higher than the quasi-static YS in AA 6061-T6 and AA 2219-T851 indicating that other mechanisms increase the strength in these alloys.

7.4.2 Precipitate evolution

In the previous chapter, the estimated quasi-static equilibrium flow stress in the SZ during the frictional experiments and the yield strength of the BM during quasi-static testing are compared. The estimated quasi-static equilibrium flow stresses of the alloys AA 6061-T6 and AA 2219-T851 are higher than the quasi-static YS of these alloys after long-term exposure to 400°C. This is thought to result from the different thermal cycles, as the unstable microstructure in heat-treatable aluminum alloys suggests that the constitutive response during hot deformation is affected by the internal state of the microstructure.

The thermal cycle directly under the rotating probe during the frictional experiments shows similarities to the thermal cycles during RFSSW as reported in Chapter 5.2, including high heating rates, relatively short exposure times to peak temperatures and high cooling rates. The main differences are the peak temperature of approximately 400°C compared to more than 500°C during welding and the higher heating rate due to the small distance from the area of interest to the rotating tool. In contrast, the BM was exposed to 400°C for 0.5 h before testing to obtain the quasi-static YS at this temperature, as analyzed in Chapter 7.3.3 and summarized in Table 7.1.

The precipitation morphology during the frictional experiments and during RFSSW differs significantly from that during quasi-static testing. To characterize the difference in flow stress during the frictional experiments compared to that during quasi-static testing, the precipitate evolution of the alloys of interest is discussed with regard to the different precipitate evolution mechanisms discussed in Chapter 6.3.2, 6.2.2 and 6.4.2.

Aluminum alloy 7075-T651

In AA 7075, the temperature of 300°C needed for dissolution of all present precipitates is exceeded during the frictional experiments. A peak temperature of 364°C and lower heating rates were found to cause the dissolution and coarsening of strengthening precipitates in the HAZ during RFSSW, as shown in the description of the precipitation evolution during welding in Chapter 6.2.2. Additionally to the higher peak temperature, the heating rate is significantly higher during the frictional experiments; thus, the precipitates have even less time to coarsen to increase their thermal stability. Large amounts of the predominant precipitates dissolve during the early stages of the thermal cycle. This is in agreement with the findings of Kamp et al. [114] during ramp heating of AA 7449 to approximately 430°C. Kamp et al. [115] also reported complete dissolution of all precipitates in AA 7050 upon rapid heating to 350°C. Compared to the conditions employed in this study, a thermal cycle with a significantly lower heating rate, in addition to the lower peak temperature, was used. Nevertheless, the preexisting η’ precipitates and some small η precipitates that formed during heating were reported to dissolve due to exposure to temperatures above 300°C.

During the exposure to the peak temperature during the frictional experiments, only very small amounts of precipitates are assumed to be present in the material subjected to subsurface flow, similar to the conditions in the SZ during RFSSW. After slow heating and long exposure to 400°C for quasi-

static testing, a very similar precipitate morphology results. Thus, the estimated quasi-static equilibrium flow stress is similar to the quasi-static yield strength for this alloy.

Aluminum alloy 6061-T6

The thermal cycle during the frictional experiments is similar to the thermal cycle at 9 mm from the center of the weld in the HAZ during RFSSW but features significantly higher heating rates. At this position, loss of clusters and pre-β" precipitates as well as primarily coarsening of the strengthening precipitates associated with peak D in Figure 6.17 was observed during the calorimetric analysis of the precipitate evolution in Chapter 6.3.2

It is assumed that a similar precipitate evolution with very little dissolution occurs during the frictional experiments. Importantly, the calorimetric analysis in Chapter 6.3.2 was conducted post-welding. The effect of the cooling phase is therefore included in the analysis. Still, the precipitate evolution in the SZ during the frictional experiments can be explained in a similar manner to the analysis of the HAZ after RFSSW when the phase formation mechanisms occurring in the cooling phase after the actual welding are neglected.

When AA 6061-T6 is exposed to 400°C for a longer period of time (e.g., 0.5 h for quasi-static testing), based on the precipitate evolution shown in Figure 6.17, the strengthening precipitates evolve towards the Q' and equilibrium Q phase. Those phases are known not to have a significant strengthening potential [25]. In contrast, strengthening precipitates are present during the frictional experiments, as the time at maximum temperature is insufficient for full precipitate evolution towards the equilibrium phase or for phase dissolution. This explains the significantly higher flow stress.

Aluminum alloy 2219-T851

A similar thermal cycle with a peak temperature of approximately 400°C featuring a lower heating rate was measured at 7 mm from the center of the weld during RFSSW. Calorimetric analysis revealed that mainly overaged θ' precipitates formed and that no dissolution occurred; compare with Chapter 6.4.2. The strength loss is caused mainly by coarsening of the strengthening precipitates.

During the frictional experiments, similar overaging phenomena are expected. Similar to AA 6061, AA 2219-T851 exposed to 400°C for longer times is predominantly evolving towards the equilibrium phase. In contrast, strengthening precipitates are still present in the SZ during the frictional experiments because of the insufficient time for precipitate evolution towards the equilibrium state. This disequilibrium state during precipitate evolution is assumed to cause the estimated quasi-static equilibrium flow stress, which is above 44 MPa, higher than the quasi-static YS of 37 MPa.

Discussion

Based on the calorimetric analysis, precipitate evolution towards the equilibrium phase was found to occur in the SZ in AA 6061-T6 and AA 2219-T851 during the frictional experiments. For both alloys, the time is insufficient to evolve the entire microstructure to the stable equilibrium state. The flow stress during plastic deformation is therefore different from the quasi-static YS at 400°C, even when the strain rate-dependent overstress is not considered. The microstructure in AA 7075-T651 in turn reaches a close-to-equilibrium state, which is characterized by dissolution of almost all of the strengthening precipitates. The estimated quasi-static flow stress of AA 7075-T651 is therefore similar to the quasi-static YS when the effect of the strain rate-dependent overstress is not considered.

For the flow stress of AA 6061-T6 and AA 2219-T851, the extent to which the strengthening precipitates evolve during the overaging process is critical. In AA 2219, the strengthening θ'' and θ' precipitates evolve, and primarily coarsened θ' precipitates prevail during the frictional phase. For AA 6061, β'' precipitates, precursors for Q' and pre-β'' type precipitates are the dominant phases at the peak-aged condition. During plastic deformation, the pre-β''-type precipitates evolve, whereas coarsened β'' precipitates and precursors for Q' are still present in the microstructure during the deformation. The resulting particle distribution causes the estimated quasi-static flow stress to be higher than the quasi-static YS, particularly in AA 6061-T6. The precipitate evolution of these two alloys at 400°C is a continuous process that causes softening up to 10,000 h of exposure [152].

The softening during the frictional phase observed in Chapter 7.3.3 is mainly driven by the precipitate evolution. For AA 7075-T651, the softening towards an equilibrium strength results from particle dissolution towards the lowest possible strength. In AA 6061-T651 and AA 2219-T851, overaging and coarsening of the strengthening precipitates occur. As longer exposure will cause further precipitate evolution towards the respective equilibrium phase, further softening towards the abovementioned values of quasi-static YS is expected to occur at 400°C. The estimated equilibrium strengths reported above, if occurring, can be considered metastable events. The concept of the estimated equilibrium strength was predicted from the flow stress development during the frictional phase towards a steady value that was not reached in the experiments. At this point, whether a steady value of strength is actually reached for these two alloys or whether further continuous softening will occur during longer frictional experiments cannot be predicted.

7.4.3 Incipient melting

The heating of an aluminum alloy can induce one or a range of endothermic melting effects depending on the alloying composition, heating rate and thermal history of the base material. The DSC trace of melting of 99.999 % pure aluminum shows a single peak in the temperature range of 660 – 700°C due to melting of the aluminum-rich phase. In aluminum alloys, the melting of the aluminum-rich phase is often preceded by the melting of one or more intermetallic phases [77]. This incipient melting phenomenon occurs when an aluminum alloy is rapidly heated to elevated temperatures and when the secondary phase particles do not dissolve before their melting temperature is reached. Therefore, incipient melting can occur at temperatures far below the solidus for certain alloys [111, 163]. During subsequent quenching, the molten phases typically solidify as a eutectic phase [111]. The liquid phase is mostly found to spread along the grain boundaries [111, 164, 165], thereby promoting grain boundary sliding during plastic deformation [166]. The magnitude of these incipient melting effects increases as the amount of intermetallic phases increases [77].

Since the heating rates are high in the conducted experiments and in RFSSW in general, secondary phase particles might have insufficient time to dissolve during heating and melt spontaneously when their melting point is attained. If present, this phenomenon must be considered when characterizing the plastic behavior of the alloys of interest because it is possible that incipient melting affects the material's response during high-strain-rate plastic deformation.

For the alloys analyzed in this study, investigations on incipient melting have been conducted in the past. Incipient melting and subsequent slippage were found to be an issue during friction welding processes by a number of investigators. A detailed literature review and analysis of the melting behavior of the alloys regarded in this study can be found in Appendix H. Incipient melting is rarely

reported for linear welding processes such as FSW but is more likely to occur during spot welds where the heat input dwells [138]. However, finding supporting metallographic evidence is the key issue as it was reported that local melted droplets formed during welding would completely dissolve during the cooling phase of the thermal cycle, removing all evidence indicating that incipient melting had occurred [100, 167].

During the exposure to peak temperatures of approximately 400°C during the frictional experiments, incipient melting is not believed to occur in the alloys of interest because the peak temperature is too low, see the analysis of the melting behavior in Appendix H. Moreover, no metallographic evidence of incipient melting was found. The flow stresses analyzed in this chapter are thus not affected by incipient melting.

The center of the SZ during RFSSW experiences a heating rate of approximately 100°C/s to high peak temperatures above 520°C; see Chapter 5.2. If the weld thermal cycle induced melting reactions, microstructural evidence should be present as long as the molten phases did not dissolve during the welds or during the cooling phase. Compared to those in the BM, the secondary particles in the SZ are significantly smaller and more homogeneously distributed after RFSSW in all alloys of interest. Figure 7.13 (a) and (b) compares a typical distribution in the SZ and BM region in AA 2219. Large secondary particles are broken up and distributed in the SZ during plastic deformation. In AA 7075 and AA 2219, several linear accumulations of secondary phases occur, appearing as horizontal black lines mostly in the upper half of the SZ in the micrographs, denoted in Figure 7.13 (b). Most of these particle accumulations are distributed along the grain boundaries, as shown in Figure 7.13 (c). Additionally, linear secondary phase distributions that are not formed along grain boundaries appear in AA 2219, Figure 7.13 (d), indicating a formation mechanism other than incipient melting.

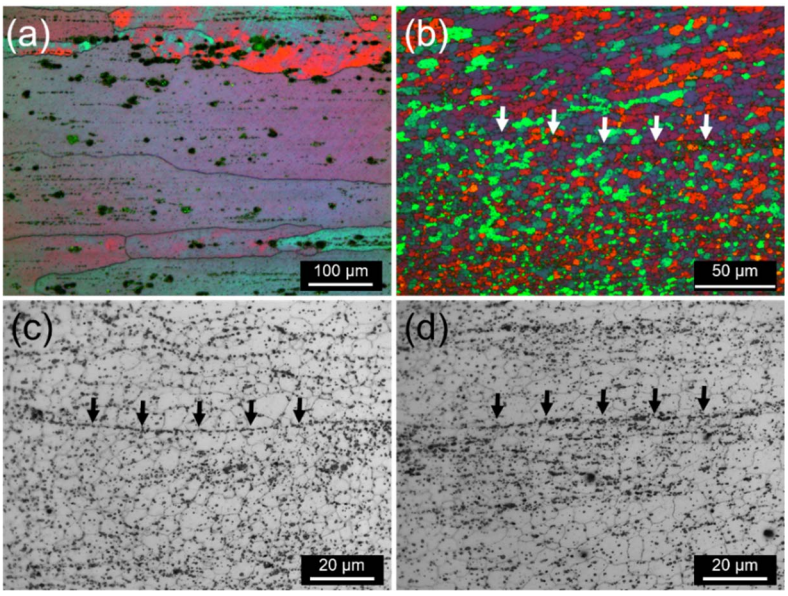

Figure 7.13 Overview of secondary the phase distribution in AA 2219-T851 (a) BM and (b) SZ. Details of the secondary phases in the SZ (c) distributed along the GB and (d) linear formation not along the GB.

In SEM analysis at higher magnification, the black lines observed in the micrographs of the SZ after RFSSW are assumed to be secondary phase accumulations on the grain boundaries. Figure 7.14 (a) shows a typical micrograph of AA 7075. Globular secondary phase particles were found concentrated

not only at the grain boundaries but also within the grains. Additionally, larger continuous films with a different morphology from the globular particles appear. The film was found to be rich in Cu and Mg, which is in agreement with the findings of [151, 168] in the SZ of friction stir welds and FSSW in 7xxx series alloys. In the SZ of AA 2219, such films were not observed at the grain boundaries, Figure 7.14 (b). Secondary particles were found to be concentrated at the grain boundaries, which causes the black lines in the micrographs. The black lines shown in Figure 7.13 (d) that did not occur at the grain boundaries result from a linear particle distribution in the direction of plastic deformation.

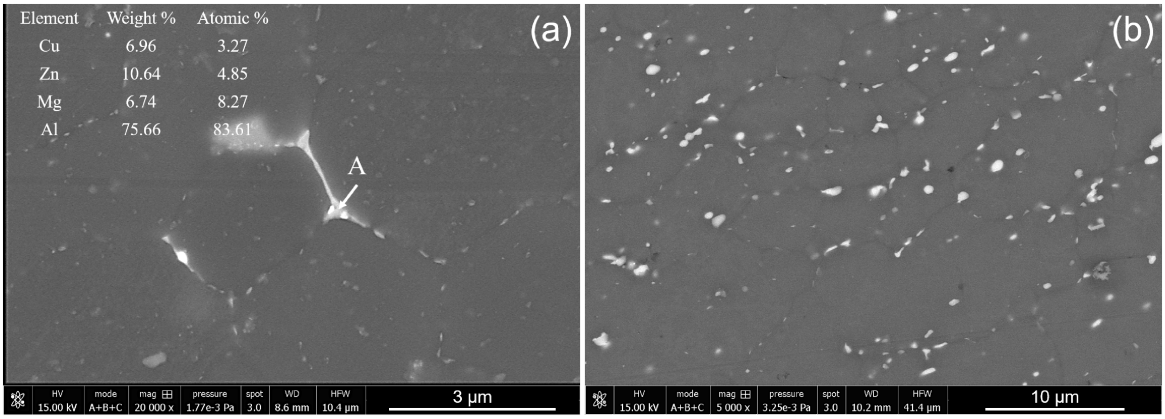

Figure 7.14 SEM micrographs (a) showing the secondary phase accumulation at the grain boundaries in AA 7075 and EDX chemical analysis at location A and (b) showing the particle distribution in the SZ of AA 2219.

The formation of Cu- and Mg-rich films at grain boundaries during the solidification of molten structures has been associated with incipient melting in 7xxx series alloys in several studies [64, 151, 163, 168]. Although the observed film formation might indicate incipient melting, it is not presumed to be explicit evidence, as grain boundary segregation of alloy components is known for 7xxx series alloys [169, 170] and especially for AA 7075 [171]. Metallographic evidence of molten structures in AA 2219 were only reported by [138] in the SZ of FSSW. In their study, large molten structures formed that were not reported by other investigators and did neither occur in this study.

Conclusions

Metallographic traces indicating incipient melting were found in the SZ of AA 7075 after RFSSW. The similar black lines occurring in the SZ of AA 2219 after RFSSW form due to secondary phase particle distribution, whereas no film formation at the grain boundaries was observed in this alloy. In the experiments conducted to analyze the material behavior during high-shear-rate plastic deformation, no black lines or film-like formations at the grain boundaries occurred. In AA 6061, no metallographic evidence of incipient melting was observed.

7.5 Summary and discussion

Frictional experiments suggested that sticking friction occurs between the rotating tool and the respective workpiece. According to friction theory, the calculated nominal shear stress on the tool-workpiece interface equals the flow stress in pure shear of the processed aluminum alloy for the chosen experimental setup. The flow stress was found to continuously decrease towards a constant

equilibrium flow stress, which was not reached during the friction phase for the alloys of interest. Contrary to the order of quasi-static YS at RT and at 400°C, the equilibrium flow stress was estimated to be 102 MPa for AA 6061-T6 > 73 MPa for AA 2219-T851 > 68 MPa for AA 7075-T651, explaining why the energy input follows the same order. The thermal cycle features a significantly higher heating rate and shorter exposure times at the peak temperature, and the shear rates are estimated to be significantly higher than those under the testing conditions used to obtain the quasi-static YS. The quasi-static YS at 400°C was reported to be relatively similar in AA 7075-T651 and AA 2219-T8 at 39 MPa and 37 MPa, respectively, whereas AA 6061-T6 was reported to be significantly softer at 15 MPa.

Based on the assumption of almost complete precipitate dissolution in AA 7075-T651 at equilibrium flow stress, the strain rate-dependent increase in the flow stress of the alloys was estimated. The increase was found to be very similar at approximately 29 MPa for AA 7075-T651 and AA 6061-T6, whereas AA 2219-T8 features smaller strain rate-dependent overstress. The fact that the equilibrium flow stress is higher than the quasi-static YS in AA 7075-T651 is caused by the higher strain rate. In AA 2219-T851 and AA 6061-T6, the time for precipitate evolution is insufficient to allow the entire microstructure to evolve to the stable equilibrium state. The strength of these alloys during plastic deformation is thus higher than the respective quasi-static YS, even when the strain rate-dependent overstress is not considered. This effect is particularly strong in AA 6061-T6, where precipitates associated with the highest strength contributions are still present during the friction phase. As further softening of AA 2219-T851 and AA 6061-T6 is reported to occur at longer processing times, it remains uncertain whether a constant equilibrium flow stress actually occurs and, if so, how long it persists. In case the concept of a constant equilibrium flow stress is wrong, the discussion of the reported values of the estimated equilibrium flow stress is still valid for describing the different material state compared to that under quasi-static testing conditions. The values can also be interpreted as the material strength at the end of frictional experiments conducted for slightly longer than those in this study. Incipient melting does not affect the flow stress during the frictional experiments because the peak temperatures of approximately 400°C are too low.

Conclusions for RFSSW

The fundamental analysis in this chapter is a general systematization of the alloy-dependent behavior for the conditions experienced in friction welding. This investigation is an initial approach to knowledge based process analysis and not a holistic approach to analyze RFSSW. Still, some essential findings can be applied to RFSSW. Additionally, the knowledge gained by this fundamental process analysis is key to enabling process optimization by guiding the appropriate choice of process parameters for a given alloy.

Sticking friction occurs at the interface of the tool and the alloys of interest above a contact pressure of approximately 80 MPa and a peak temperature of 400°C. The general observation of flow stress in the order AA 6061-T6 > AA 2219-T851 > AA 7075-T651, which explains the energy input following the same order can be applied to RFSSW.

The strain rate-dependent overstress in the SZ during RFSSW cannot be predicted at this point, as the strain rate estimation is complicated by material flow complexities. Generally, it is found that the flow stress distribution in the SZ during RFSSW is quite inhomogeneous, as stress concentrations and partial recrystallization are commonly observed. Still, from the estimations during the frictional experiments in this chapter, the overstress is found to be similar in the alloys of interest, especially

in AA 6061-T6 and AA 7075-T651. Differences in flow stress due to the velocity dependent overstress are thus assumed to not cause the higher energy input in AA 6061-T6 during RFSSW.

The precipitate evolution during RFSSW was analyzed in Chapter 6.3.2, 6.2.2 and 6.4.2. In the weld center, high peak temperatures above 500°C were found, which were observed to cause almost complete dissolution in the alloys of interest. Still, it is expected that the thermal cycle underneath the front surface of the plunging sleeve differs, as the weld center is isolated by the sleeve during the weld, thereby impeding heat dissipation. Additionally, slower precipitate evolution towards full dissolution occurs in AA 6061-T6 and AA 2219-T851 compared to AA 7075-T651. In particular, the lower heating rate causes precipitates to grow and become more stable at higher temperatures. Still, it is assumed that the quasi-static flow stress during RFSSW is lower than the quasi-static flow stresses observed during the frictional experiments for AA 2219 and AA 6061 and similar for AA 7075.

As the temperature is significantly higher than 500°C in the SZ during RFSSW, incipient melting affects the hot deformation behavior in AA 7075-T651. If melting occurs, it is thought to contribute to flow stress reduction due to grain boundary sliding.

Process parameter

The energy input during friction welding at similar boundary conditions is defined and therefore limited by the material's flow stress. Increasing the pressure at the tool-workpiece interface will not lead to a higher energy input, as the transferable shear stress from the tool into the workpiece is independent of the pressure. An increase in rotational speed will increase the energy input according to Equation (2) and increase the flow stress due to higher shear rates, but the expected increase in temperature reduces the material's strength, which then reduces the torque. This will in turn limit the energy input.

The suitable clamping pressure is affected by the flow stress of the base material during welding and by the strength in the HAZ. At higher flow stresses, using a higher clamping pressure is advised to prevent rotation of the welded sample. The strength of the base material has to be considered because it limits the settable clamping pressure in order to prevent plunging of the clamping ring during welding.

The quasi-static YS of an alloy at RT or at elevated temperature is not decisive for the flow stress during friction welding. The crucial factors are the initial temper state, thermal cycle, precipitate evolution behavior and strength contribution of the various precipitate phases. If an alloy exhibits high flow stress during deformation, the energy input will inevitably be high. The overall mechanical properties are then dependent on the precipitate evolution in the different weld zones during welding and the ability to increase the strength during post-weld natural aging.

As AA 7075-T651 is prone to incipient melting, the temperature during welding should be kept below 475°C if possible. Alternatively, process parameters causing a lower heating rate should be employed during friction welding to enable the dissolution of secondary phase particles prior to reaching the eutectic temperature.

8 Conclusions

In accordance with the objectives of this work, a keyhole repair method employing RFSSW was successfully developed. RFSSW was proven to be a promising method for sealing through holes in various precipitation hardening aluminum alloys. To characterize the repair procedure, a fundamental analysis of the process and resulting material properties, including the alloy-dependent differences in welds in AA 2219-T851, AA 6061-T6 and AA 7075-T651, was conducted. A fundamental characterization of the base material behavior under the conditions of friction welding operations was performed to investigate the differences in energy input during RFSSW. The influence of the base material composition and material properties on the energy input during friction welding was determined, and the friction condition and flow stress development were comprehensively analyzed.

The key observations and conclusions were as follows:

Fundamental process development

The developed keyhole repair method seals through holes by applying a similar plug as filler material and using RFSSW to weld the plug to the surrounding workpiece. Keyhole repair using RFSSW was demonstrated as a universal through-hole closure method that offers advantages such as defect-free welds and superior surface appearance on both sides of the weld. The repair method does not require any surface preparation before or after the welding process, seals the keyhole in a single step and can be performed using conventional RFSSW equipment.For each of the three precipitation hardening aluminum alloys of interest, process parameter windows for achieving defect-free welds were developed. The process was successfully conducted using different tool sizes to repair 5 mm, 7.5 mm and 10 mm diameter keyholes in 3 mm-thick sheets and 7.5 mm diameter keyholes in 6 mm thick sheets.

As a proof-of-concept in a feasibility study, the knowledge generated in this work was successfully applied to perform keyhole repair welds of SSuBT-FSW exit holes in the Al-Cu-Li alloy AA 2198-T8. The study was published separately by the author [30] and proved the ability of RFSSW to be applied as a termination hole repair technique for BT-FSW welds.

Process analysis

When AA 2219-T851, AA 6061-T6 and AA 7075-T651 are processed by the developed repair procedure, the resulting thermal cycles feature similar characteristics including high heating and cooling rates and short exposure times at peak temperature. Metallographic analysis revealed similar microstructural zone formation to that in conventional RFSSW. A microstructure featuring partial recrystallization and inhomogeneous grain size distribution were typically found in the SZ mainly caused by the high plunge depth.

The thermal cycles induced by the RFSSW process caused complete or almost complete dissolution of the strengthening precipitates in the SZ during the weld in all alloys of interest. In the areas surrounding the SZ, decreasing dissolution of strengthening particles and increasing overaging phenomena with increasing distance from the weld center were found. The resulting precipitate distribution mainly determines the local mechanical properties in the different weld zones. In the SZ of all the processed alloys, a large amount of solute was found to be present in the solution in the as-welded condition, causing re-precipitation of strengthening precipitates during post-weld natural aging. This re-precipitation significantly increased the strength in and around the weld.

A W-shaped microhardness distribution featuring a weld center of medium strength and a position of lowest hardness in the HAZ (AA 6061-T6 and AA 7075-T651) or TMAZ (AA 2219-T8) was observed and yielding in tensile tests at RT started in this region of lowest hardness. For repair welds of 7.5 mm diameter keyholes in 3 mm-thick sheets, the weld efficiency is 60 % in YS and 72 % in UTS for AA 2219-T851, 54 % in YS and 67 % in UTS for AA 6061-T6 as well as 64 % in YS, 80 % in UTS for fracture in the HAZ and 77 % in UTS for fracture in the SZ for AA 7075-T651.

Material behavior during high-shear-rate plastic deformation

Solid-state friction welding experiments were performed to investigate the friction condition and plastic behavior of the alloys of interest under conditions similar to RFSSW. The results suggested that sticking friction occurs above a contact pressure of 80 MPa and a temperature of 400°C in the alloys of interest processed with the tools used in this work. Contrary to the order of the quasi-static YS at RT and at 400°C, the flow stress was estimated to be highest in AA 6061-T6, followed by AA 2219-T851 and then AA 7075-T651, explaining why the energy input follows the same order. Additionally, the observed values of equilibrium flow stress, 102 MPa for AA 6061-T6, 73 MPa for AA 2219-T851 and 68 MPa for AA 7075-T651, were found to be significantly higher than the quasi-static YS of 15 MPa for AA 6061-T6, 37 MPa for AA 2219-T851 and 39 MPa for AA 7075-T651 at similar temperatures.

The thermal cycle featured a significantly higher heating rate and shorter exposure time to the peak temperature, and the strain rates are significantly higher than those under quasi-static testing conditions. The findings of this study suggested that these differences in strain rate and thermal cycle are sufficient to explain the difference between the measured flow stress and the quasi-static YS.

During high-shear-rate plastic deformation at thermal cycles typical for friction welding operations, the precipitate evolution was found to primarily determine the difference in material properties. For AA 2219-T851 and AA 6061-T6, the time for precipitate evolution is insufficient to allow the entire microstructure to evolve to a stable equilibrium state. The flow stress during high-shear-rate plastic deformation was found to be 58 MPa and more than 7 MPa higher in AA 6061-T6 and AA 2219-T851, respectively, than the respective quasi-static yield strength, even when the strain rate-dependent overstress is not considered. In AA 7075-T651, the higher flow stress than quasi-static YS is caused solely by the higher rate of deformation, as complete particle dissolution occurs both in the frictional experiments and under quasi-static testing conditions.

The investigation revealed that the knowledge of mechanical properties obtained under quasi-static testing conditions is not sufficient to understand or predict the material properties under the conditions of friction welding operations for precipitation hardening aluminum alloys. The alloy composition, initial condition and general precipitation evolution characteristics during the specific thermal cycles associated with friction welding operations were found to determine the different material properties at the tested rates of deformation.

Based on the insight into material behavior provided by this fundamental analysis, a general systematization of the alloy-dependent behavior during various friction welding operations might arise. Initial recommendations for the developed repair process employing RFSSW were derived in this work to enable process optimization.

References

[1] J. Chen, E. Costan, M. Van Huis, Q. Xu, H. Zandbergen, Atomic pillar-based nanoprecipitates strengthen AlMgSi alloys, Science 312 (2006) 416-419.

[2] G. Çam, G. İpekoğlu, Recent developments in joining of aluminum alloys, The International Journal of Advanced Manufacturing Technology 91 (2017) 1851-1866.

[3] W.-S. Lee, W.-C. Sue, C.-F. Lin, C.-J. Wu, The strain rate and temperature dependence of the dynamic impact properties of 7075 aluminum alloy, Journal of Materials Processing Technology 100 (2000) 116-122.

[4] X. Fan, D. Jiang, Q. Meng, Z. Lai, X. Zhang, Characterization of precipitation microstructure and properties of 7150 aluminium alloy, Materials Science and Engineering: A 427 (2006) 130-135.

[5] K.S. Arora, S. Pandey, M. Schaper, R. Kumar, Microstructure Evolution during Friction Stir Welding of Aluminum Alloy AA2219, Journal of Materials Science & Technology 26 (2010) 747-753.

[6] A. Dorbane, G. Ayoub, B. Mansoor, R. Hamade, G. Kridli, A. Imad, Observations of the mechanical response and evolution of damage of AA 6061-T6 under different strain rates and temperatures, Materials Science and Engineering: A 624 (2015) 239-249.

[7] J.C. Williams, E.A. Starke, Progress in structural materials for aerospace systems, Acta Materialia 51 (2003) 5775-5799.

[8] A.C. Okafor, N. Singh, U.E. Enemuoh, S.V. Rao, Design, analysis and performance of adhesively bonded composite patch repair of cracked aluminum aircraft panels, Composite Structures 71 (2005) 258-270.

[9] T. Dursun, C. Soutis, Recent developments in advanced aircraft aluminium alloys, Materials & Design 56 (2014) 862-871.

[10] R.S. Mishra, Z.Y. Ma, Friction stir welding and processing, Materials Science and Engineering: R: Reports 50 (2005) 1-78.

[11] G. Çam, S. Mistikoglu, Recent Developments in Friction Stir Welding of Al-alloys, Journal of Materials Engineering and Performance 23 (2014) 1936-1953.

[12] G. Madhusudhan Reddy, A.A. Gokhale, Welding Aspects of Aluminum–Lithium Alloys, in: S. Merken, J. Freeland (Eds.), Aluminum-Lithium Alloys - Processing, Properties, and Applications, Butterworth-Heinemann Oxford, UK, 2014, pp. 259-302.

[13] S. Behmand, S. Mirsalehi, H. Omidvar, M. Safarkhanian, Filling exit holes of friction stir welding lap joints using consumable pin tools, Science and Technology of Welding and Joining 20 (2015) 330-336.

[14] Z. Shen, X. Yang, Z. Zhang, L. Cui, T. Li, Microstructure and failure mechanisms of refill friction stir spot welded 7075-T6 aluminum alloy joints, Materials & Design 44 (2013) 476-486.

[15] M.D. Tier, T.S. Rosendo, J.F. dos Santos, N. Huber, J.A. Mazzaferro, C.P. Mazzaferro, T.R. Strohaecker, The influence of refill FSSW parameters on the microstructure and shear strength of 5042 aluminium welds, Journal of Materials Processing Technology 213 (2013) 997-1005.

[16] U.F.H. Suhuddin, V. Fischer, J.F. dos Santos, The thermal cycle during the dissimilar friction spot welding of aluminum and magnesium alloy, Scripta Materialia 68 (2013) 87-90.

[17] P.S. Effertz, V. Infante, L. Quintino, U. Suhuddin, S. Hanke, J.F. dos Santos, Fatigue life assessment of friction spot welded 7050-T76 aluminium alloy using Weibull distribution, International Journal of Fatigue 87 (2016) 381-390.

[18] L. Cheah, J. Heywood, R. Kirchain, Aluminum Stock and Flows in U.S. Passenger Vehicles and Implications for Energy Use, Journal of Industrial Ecology 13 (2009) 718-734.

[19] M. Bertram, K.J. Martchek, G. Rombach, Material Flow Analysis in the Aluminum Industry, Journal of Industrial Ecology 13 (2009) 650-654.

[20] A.S. Warren, Developments and challenges for aluminum--A boeing perspective, Proceedings of the 9th International Conference on Aluminium Alloys, Institute of Materials Engineering Australasia, 2004, pp. 24-31.

[21] H.J. McQueen, S. Spigarelli, M.E. Kassner, E. Evangelista, Hot deformation and processing of aluminum alloys, CRC Press, Boca Raton, US, 2011.

[22] B. Li, Y. Shen, The investigation of abnormal particle-coarsening phenomena in friction stir repair weld of 2219-T6 aluminum alloy, Materials & Design 32 (2011) 3796-3802.

[23] X. Lei, Y. Deng, Z. Yin, G. Xu, Tungsten Inert Gas and Friction Stir Welding Characteristics of 4-mm-Thick 2219-T87 Plates at Room Temperature and −196 °C, Journal of Materials Engineering and Performance 23 (2014) 2149-2158.

[24] J. Kang, Z.-C. Feng, G.S. Frankel, I.W. Huang, G.-Q. Wang, A.-P. Wu, Friction Stir Welding of Al Alloy 2219-T8: Part I-Evolution of Precipitates and Formation of Abnormal Al2Cu Agglomerates, Metallurgical and Materials Transactions A 47 (2016) 4553-4565.

[25] D.J. Chakrabarti, D.E. Laughlin, Phase relations and precipitation in Al–Mg–Si alloys with Cu additions, Progress in Materials Science 49 (2004) 389-410.

[26] M. Rosen, E. Horowitz, S. Fick, R.C. Reno, R. Mehrabian, An investigation of the precipitation-hardening process in aluminum alloy 2219 by means of sound wave velocity and ultrasonic attenuation, Materials Science and Engineering 53 (1982) 163-177.

[27] R. Ferragut, A. Somoza, A. Dupasquier, On the two-step ageing of a commercial Al - Zn - Mg alloy; a study by positron lifetime spectroscopy, Journal of Physics: Condensed Matter 8 (1996) 8945.

[28] I. Polmear, Light alloys: from traditional alloys to nanocrystals, Butterworth-Heinemann, Oxford, UK, 2005.

[29] M. Reimann, T. Gartner, U. Suhuddin, J. Göbel, J.F. dos Santos, Keyhole closure using friction spot welding in aluminum alloy 6061–T6, Journal of Materials Processing Technology 237 (2016) 12-18.

[30] M. Reimann, J. Goebel, T.M. Gartner, J.F. dos Santos, Refilling termination hole in AA 2198-T851 by refill friction stir spot welding, Journal of Materials Processing Technology 245 (2017) 157-166.

[31] M. Reimann, J. Goebel, J.F. dos Santos, Microstructure and mechanical properties of keyhole repair welds in AA 7075-T651 using refill friction stir spot welding, Materials & Design 132 (2017) 283-294.

[32] B. Du, Z. Sun, X. Yang, L. Cui, J. Song, Z. Zhang, Characteristics of friction plug welding to 10 mm thick AA2219-T87 sheet: Weld formation, microstructure and mechanical property, Materials Science and Engineering A 654 (2016) 21-29.

[33] D.F. Metz, E.R. Weishaupt, M.E. Barkey, B.S. Fairbee, A Microstructure and Microhardness Characterization of a Friction Plug Weld in Friction Stir Welded 2195 Al-Li, Journal of Engineering Materials and Technology 134 (2012) 021005.

[34] D.F. Metz, M.E. Barkey, Fatigue behavior of friction plug welds in 2195 Al–Li alloy, International Journal of Fatigue 43 (2012) 178-187.

[35] Y. Huang, B. Han, Y. Tian, H. Liu, S. Lv, J. Feng, J. Leng, Y. Li, New technique of filling friction stir welding, Science and Technology of Welding and Joining 16 (2011) 497-501.

[36] B. Han, Y.X. Huang, S.X. Lv, L. Wan, J.C. Feng, G.S. Fu, AA7075 bit for repairing AA2219 keyhole by filling friction stir welding, Materials & Design 51 (2013) 25-33.

[37] G.F. Zhang, W.M. Jiao, J.X. Zhang, Filling friction stir weld keyhole using pin free tool and T shaped filler bit, Science and Technology of Welding and Joining 19 (2014) 98-104.

[38] S. Ji, X. Meng, Y. Zeng, L. Ma, S. Gao, New technique for eliminating keyhole by active-passive filling friction stir repairing, Materials & Design 97 (2016) 175-182.

[39] S.D. Ji, X.C. Meng, R.F. Huang, L. Ma, S.S. Gao, Microstructures and mechanical properties of 7N01-T4 aluminum alloy joints by active-passive filling friction stir repairing, Materials Science and Engineering: A 664 (2016) 94-102.

[40] K. Chen, X. Liu, J. Ni, Keyhole Refilled Friction Stir Spot Welding of Aluminum Alloy to Advanced High Strength Steel, Journal of Materials Processing Technology 249 (2017) 452-462.

[41] L. Zhou, D. Liu, K. Nakata, T. Tsumura, H. Fujii, K. Ikeuchi, Y. Michishita, Y. Fujiya, M. Morimoto, New technique of self-refilling friction stir welding to repair keyhole, Science and Technology of Welding and Joining 17 (2012) 649-655.

[42] M. Sajed, Parametric study of two-stage refilled friction stir spot welding, Journal of Manufacturing Processes 24 (2016) 307-317.

[43] Y. Uematsu, K. Tokaji, Y. Tozaki, T. Kurita, S. Murata, Effect of re-filling probe hole on tensile failure and fatigue behaviour of friction stir spot welded joints in Al–Mg–Si alloy, International Journal of Fatigue 30 (2008) 1956-1966.

[44] M.W. Mahoney, N.G. Taylor, W.H. Bingel, F.E. Long, R.A. Spurling, G.S. Steele, Method to repair voids in aluminum alloys, US 5,971,252, Patent, 1999.

[45] S.J. Prakash, S. Muthukumaran, Refilling Probe Hole of Friction Spot Joints by Friction Forming, Materials and Manufacturing Processes 26 (2011) 1539-1545.

[46] S. Venukumar, S. Yalagi, S. Muthukumaran, Comparison of microstructure and mechanical properties of conventional and refilled friction stir spot welds in AA 6061-T6 using filler plate, Transactions of Nonferrous Metals Society of China 23 (2013) 2833-2842.

[47] C. Schilling, J. dos Santos, Method and device for joining at least two adjoining work pieces by friction welding, US Patent 6, 722, 556 B2, 2004.

[48] T. Rosendo, B. Parra, M.A.D. Tier, A.A.M. da Silva, J.F. dos Santos, T.R. Strohaecker, N.G. Alcântara, Mechanical and microstructural investigation of friction spot welded AA6181-T4 aluminium alloy, Materials & Design 32 (2011) 1094-1100.

[49] S.T. Amancio-Filho, A.P.C. Camillo, L. Bergmann, J.F.d. Santos, S.E. Kury, N.G.A. Machado, Preliminary Investigation of the Microstructure and Mechanical Behaviour of 2024 Aluminium Alloy Friction Spot Welds, Materials Transactions 52 (2011) 985-991.

[50] Z. Shen, Y. Chen, J.S.C. Hou, X. Yang, A.P. Gerlich, Influence of processing parameters on microstructure and mechanical performance of refill friction stir spot welded 7075-T6 aluminium alloy, Science and Technology of Welding and Joining 20 (2015) 48-57.

[51] S. Amancio-Filho, S. Sheikhi, J. Dos Santos, C. Bolfarini, Preliminary study on the microstructure and mechanical properties of dissimilar friction stir welds in aircraft aluminium alloys 2024-T351 and 6056-T4, Journal of Materials Processing Technology 206 (2008) 132-142.

[52] U. Suhuddin, V. Fischer, F. Kroeff, J.F. dos Santos, Microstructure and mechanical properties of friction spot welds of dissimilar AA5754 Al and AZ31 Mg alloys, Materials Science and Engineering A 590 (2014) 384-389.

[53] J. Shen, U.F.H. Suhuddin, M.E.B. Cardillo, J.F. dos Santos, Eutectic structures in friction spot welding joint of aluminum alloy to copper, Applied Physics Letters 104 (2014) 191901.

[54] H. Dong, S. Chen, Y. Song, X. Guo, X. Zhang, Z. Sun, Refilled friction stir spot welding of aluminum alloy to galvanized steel sheets, Materials & Design 94 (2016) 457-466.

[55] G.S. Vacchi, A.H. Plaine, R. Silva, V.L. Sordi, U.F.H. Suhuddin, N.G. Alcântara, S.E. Kuri, C.A.D. Rovere, Effect of friction spot welding (FSpW) on the surface corrosion behavior of overlapping AA6181-T4/Ti-6Al-4V joints, Materials & Design 131 (2017) 127-134.

[56] T. Rosendo, M. Tier, J. Mazzaferro, C. Mazzaferro, T. Strohaecker, J. Dos Santos, Mechanical performance of AA6181 refill friction spot welds under Lap shear tensile loading, Fatigue & Fracture of Engineering Materials & Structures 00 (2015) 1-13.

[57] U. Suhuddin, L. Campanelli, M. Bissolatti, H. Wang, R. Verastegui, J.F. dos Santos, A review on microstructural and mechanical properties of friction spot welds in Al-based similar and dissimilar joints, in: H. Fujii (Ed.), Proceedings of the 1st International Joint Symposium on Joining and Welding 2013, pp. 15-21.

[58] C. Allen, W. Arbegast, Evaluation of Friction Spot Welds in Aluminum Alloys, SAE Technical Paper Series 2005-01-1252 (2005).

[59] U. Suhuddin, S. Mironov, H. Krohn, M. Beyer, J.F. Dos Santos, Microstructural Evolution During Friction Surfacing of Dissimilar Aluminum Alloys, Metallurgical and Materials Transactions A 43 (2012) 5224-5231.

[60] Z. Shen, X. Yang, S. Yang, Z. Zhang, Y. Yin, Microstructure and mechanical properties of friction spot welded 6061-T4 aluminum alloy, Materials & Design 54 (2014) 766-778.

[61] A.H. Plaine, A.R. Gonzalez, U.F.H. Suhuddin, J.F. dos Santos, N.G. Alcântara, The optimization of friction spot welding process parameters in AA6181-T4 and Ti6Al4V dissimilar joints, Materials & Design 83 (2015) 36-41.

[62] C. Oberembt, C. Allen, W. Arbegast, A. Patnaik, Screening for process variable sensistivity in refill friction spot welding of 6061 aluminum sheet, Minerals, Metals & Materials Soc, Warrendale, 2007.

[63] J.Y. Cao, M. Wang, L. Kong, H.X. Zhao, P. Chai, Microstructure, texture and mechanical properties during refill friction stir spot welding of 6061-T6 alloy, Materials Characterization 128 (2017) 54-62.

[64] Y. Zhao, H. Liu, T. Yang, Z. Lin, Y. Hu, Study of temperature and material flow during friction spot welding of 7B04-T74 aluminum alloy, The International Journal of Advanced Manufacturing Technology (2015) 1-9.

[65] Y.Q. Zhao, H.J. Liu, Z. Lin, S.X. Chen, J.C. Hou, Microstructures and mechanical properties of friction spot welded Alclad 7B04-T74 aluminium alloy, Science and Technology of Welding and Joining 19 (2014) 617-622.

[66] Y.Q. Zhao, H.J. Liu, S.X. Chen, Z. Lin, J.C. Hou, Effects of sleeve plunge depth on microstructures and mechanical properties of friction spot welded alclad 7B04-T74 aluminum alloy, Materials & Design 62 (2014) 40-46.

[67] Y.C. Chen, J.C. Feng, H.J. Liu, Precipitate evolution in friction stir welding of 2219-T6 aluminum alloys, Materials Characterization 60 (2009) 476-481.

[68] W. Xu, J. Liu, G. Luan, C. Dong, Microstructure and mechanical properties of friction stir welded joints in 2219-T6 aluminum alloy, Materials & Design 30 (2009) 3460-3467.

[69] B. Du, L. Cui, X. Yang, D. Wang, Z. Sun, Weakening mechanism and tensile fracture behavior of AA 2219-T87 friction plug welds, Materials Science and Engineering: A 693 (2017) 129-135.

[70] X. Feng, H. Liu, J.C. Lippold, Microstructure characterization of the stir zone of submerged friction stir processed aluminum alloy 2219, Materials Characterization 82 (2013) 97-102.

[71] F. Ostermann, Anwendungstechnologie Aluminium Springer, Berlin, 2007.

[72] P. Vilaça, W. Thomas, Friction Stir Welding Technology, Advanced Structured Materials 8 (2011) 85-124.

[73] P. Su, A. Gerlich, T.H. North, G.J. Bendzsak, Energy utilisation and generation during friction stir spot welding, Science and Technology of Welding and Joining 11 (2006) 163-169.

[74] N. Kashaev, M. Horstmann, V. Ventzke, S. Riekehr, N. Huber, Comparative study of mechanical properties using standard and micro-specimens of base materials Inconel 625, Inconel 718 and Ti-6Al-4V, Journal of Materials Research and Technology 2 (2013) 43-47.

[75] X.J. Jiang, J. Tafto, B. Noble, B. Holme, G. Waterloo, Differential scanning calorimetry and electron diffraction investigation on low-temperature aging in Al-Zn-Mg alloys, Metallurgical and Materials Transactions A 31 (2000) 339-348.

[76] Z. Liang, J. Banhart, Clustering and Precipitation in Al-Mg-Si Alloys, PhD Thesis, Technische Universität Berlin, 2012.

[77] M.J. Starink, Analysis of aluminium based alloys by calorimetry: quantitative analysis of reactions and reaction kinetics, International Materials Reviews 49 (2004) 191-226.

[78] C.B. Fuller, M.W. Mahoney, M. Calabrese, L. Micona, Evolution of microstructure and mechanical properties in naturally aged 7050 and 7075 Al friction stir welds, Materials Science and Engineering: A 527 (2010) 2233-2240.

[79] J.M. Papazian, A calorimetric study of precipitation in aluminum alloy 2219, Metallurgical Transactions A 12 (1981) 269-280.

[80] J. Osten, B. Milkereit, C. Schick, O. Kessler, Dissolution and Precipitation Behaviour during Continuous Heating of Al–Mg–Si Alloys in a Wide Range of Heating Rates, Materials 8 (2015) 2830-2848.

[81] B. Milkereit, Kontinuierliche Zeit-Temperatur- Ausscheidungs-Diagramme von Al-Mg-Si-Legierungen, PhD Thesis, Universität Rostock, 2011.

[82] B. Milkereit, M.J. Starink, Quench sensitivity of Al–Mg–Si alloys: A model for linear cooling and strengthening, Materials & Design 76 (2015) 117-129.

[83] A. Meyer, Friction Hydro Pillar Processing - Bonding Mechanism and Properties, PhD Thesis, Technische Universität Carolo-Wilhelmina zu Braunschweig, 2003.

[84] A.v.d. Stelt, Friction Surface Cladding - development of a solid state cladding process, PhD Thesis, University of Twente, 2014.

[85] A.S. Zuruzi, H. Li, G. Dong, Effects of surface roughness on the diffusion bonding of Al alloy 6061 in air, Materials Science and Engineering: A 270 (1999) 244-248.

[86] A. Zuruzi, H. Li, G. Dong, Diffusion bonding of aluminium alloy 6061 in air using an interface treatment technique, Materials Science and Engineering-A-Structural Materials 259 (1999) 145-148.

[87] A. Sagai Francis Britto, R.E. Raj, M.C. Mabel, Prediction of shear and tensile strength of the diffusion bonded AA5083 and AA7075 aluminium alloy using ANN, Materials Science and Engineering: A 692 (2017) 1-8.

[88] Y. Huang, N. Ridley, F.J. Humphreys, J.Z. Cui, Diffusion bonding of superplastic 7075 aluminium alloy, Materials Science and Engineering: A 266 (1999) 295-302.

[89] G. Çam, M. Koçak, Progress in joining of advanced materials, International Materials Reviews 43 (1998) 1-44.

[90] C. Gao, Z. Zhu, J. Han, H. Li, Correlation of microstructure and mechanical properties in friction stir welded 2198-T8 Al–Li alloy, Materials Science and Engineering: A 639 (2015) 489-499.

[91] D. Raabe, M. Herbig, S. Sandlöbes, Y. Li, D. Tytko, M. Kuzmina, D. Ponge, P.P. Choi, Grain boundary segregation engineering in metallic alloys: A pathway to the design of interfaces, Current Opinion in Solid State and Materials Science 18 (2014) 253-261.

[92] W. Woo, L. Balogh, T. Ungár, H. Choo, Z. Feng, Grain structure and dislocation density measurements in a friction-stir welded aluminum alloy using X-ray peak profile analysis, Materials Science and Engineering: A 498 (2008) 308-313.

[93] C.G. Rhodes, M.W. Mahoney, W.H. Bingel, R.A. Spurling, C.C. Bampton, Effects of friction stir welding on microstructure of 7075 aluminum, Scripta Materialia 36 (1997) 69-75.

[94] N. Kamp, A. Sullivan, R. Tomasi, J.D. Robson, Modelling of heterogeneous precipitate distribution evolution during friction stir welding process, Acta Materialia 54 (2006) 2003-2014.

[95] S. Rajakumar, C. Muralidharan, V. Balasubramanian, Predicting tensile strength, hardness and corrosion rate of friction stir welded AA6061-T6 aluminium alloy joints, Materials & Design 32 (2011) 2878-2890.

[96] Y. Sato, H. Kokawa, M. Enomoto, S. Jogan, Microstructural evolution of 6063 aluminum during friction-stir welding, Metallurgical and Materials Transactions A 30 (1999) 2429-2437.

[97] G. İpekoğlu, S. Erim, G. Çam, Investigation into the Influence of Post-Weld Heat Treatment on the Friction Stir Welded AA6061 Al-Alloy Plates with Different Temper Conditions, Metallurgical and Materials Transactions A 45 (2013) 864-877.

[98] G. İpekoğlu, S. Erim, G. Çam, Effects of temper condition and post weld heat treatment on the microstructure and mechanical properties of friction stir butt-welded AA7075 Al alloy plates, The International Journal of Advanced Manufacturing Technology 70 (2013) 201-213.

[99] G. Pieta, J. dos Santos, T.R. Strohaecker, T. Clarke, Optimization of Friction Spot Welding Process Parameters for AA2198-T8 Sheets, Materials and Manufacturing Processes 29 (2014) 934-940.

[100] A. Gerlich, G. Avramovic-Cingara, T.H. North, Stir zone microstructure and strain rate during Al 7075-T6 friction stir spot welding, Metallurgical and Materials Transactions a-Physical Metallurgy and Materials Science 37A (2006) 2773-2786.

[101] D.H. Li, Y. Yang, T. Xu, H.G. Zheng, Q.S. Zhu, Q.M. Zhang, Observation of the microstructure in the adiabatic shear band of 7075 aluminum alloy, Materials Science and Engineering: A 527 (2010) 3529-3535.

[102] F.F. Wang, W.Y. Li, J. Shen, S.Y. Hu, J.F. dos Santos, Effect of tool rotational speed on the microstructure and mechanical properties of bobbin tool friction stir welding of Al–Li alloy, Materials & Design 86 (2015) 933-940.

[103] Y.S. Sato, F. Yamashita, Y. Sugiura, S.H.C. Park, H. Kokawa, FIB-assisted TEM study of an oxide array in the root of a friction stir welded aluminium alloy, Scripta Materialia 50 (2004) 365-369.

[104] G.E. Totten, D.S. MacKenzie, Handbook of Aluminum: Vol. 1: Physical Metallurgy and Processes, Marcel Dekker, Inc., New York, NY, USA, 2003.

[105] M. Reimann, J. Goebel, J.F. Dos Santos, Microstructure Evolution and Mechanical Properties of Keyhole Repair Welds in AA 2219-T851 using Refill Friction Stir Spot Welding, Submitted for publication in Journal of Materials Engineering and Performance (2018).

[106] M.J. Starink, X.M. Li, A model for the electrical conductivity of peak-aged and overaged Al-Zn-Mg-Cu alloys, Metallurgical and Materials Transactions A 34 (2003) 899-911.

[107] R. De Iasi, P.N. Adler, Calorimetric studies of 7000 series aluminum alloys: I. Matrix precipitate characterization of 7075, Metallurgical Transactions A 8 (1977) 1177-1183.

[108] F. Viana, A.M.P. Pinto, H.M.C. Santos, A.B. Lopes, Retrogression and re-ageing of 7075 aluminium alloy: microstructural characterization, Journal of Materials Processing Technology 92–93 (1999) 54-59.

[109] M.J. Starink, S.C. Wang, A model for the yield strength of overaged Al–Zn–Mg–Cu alloys, Acta Materialia 51 (2003) 5131-5150.

[110] A. Dupasquier, R. Ferragut, M.M. Iglesias, C.E. Macchi, M. Massazza, P. Mengucci, G. Riontino, A. Somoza, Early Solute Clustering in an AlZnMg Alloy, Materials Science Forum 445-446 (2004) 16-20.

[111] P.-E. Droenen, N. Ryum, Local melting in Al-Mg-Zn-alloys, Metallurgical and Materials Transactions A 25 (1994) 521-530.

[112] P.N. Adler, R. DeIasi, Calorimetric studies of 7000 series aluminum alloys: II. Comparison of 7075, 7050 and RX720 alloys, Metallurgical Transactions A 8 (1977) 1185-1190.

[113] D.J. Lloyd, M.C. Chaturvedi, A calorimetric study of aluminium alloy AA-7075, Journal of Materials Science 17 (1982) 1819-1824.

[114] N. Kamp, A. Sullivan, J.D. Robson, Modelling of friction stir welding of 7xxx aluminium alloys, Materials Science and Engineering: A 466 (2007) 246-255.

[115] N. Kamp, A.P. Reynolds, J.D. Robson, Modelling of 7050 aluminium alloy friction stir welding, Science and Technology of Welding and Joining 14 (2009) 589-596.

[116] G.A. Edwards, K. Stiller, G.L. Dunlop, M.J. Couper, The precipitation sequence in Al–Mg–Si alloys, Acta Materialia 46 (1998) 3893-3904.

[117] C.D. Marioara, S.J. Andersen, T.N. Stene, H. Hasting, J. Walmsley, A.T.J. Van Helvoort, R. Holmestad, The effect of Cu on precipitation in Al–Mg–Si alloys, Philosophical Magazine 87 (2007) 3385-3413.

[118] S.M.A. I. Dutta, A calorimetric study of precipitation in commercial aluminium alloy 6061, Journal of Materials Science Letters 10 (1991) 323 - 326.

[119] H.S. Hasting, A.G. Frøseth, S.J. Andersen, R. Vissers, J.C. Walmsley, C.D. Marioara, F. Danoix, W. Lefebvre, R. Holmestad, Composition of β″ precipitates in Al–Mg–Si alloys by atom probe tomography and first principles calculations, Journal of Applied Physics 106 (2009) 123527.

[120] K. Matsuda, S. Ikeno, Y. Uetani, T. Sato, Metastable phases in an Al-Mg-Si alloy containing copper, Metallurgical and Materials Transactions A 32 (2001) 1293-1299.

[121] C. Ravi, C. Wolverton, First-principles study of crystal structure and stability of Al-Mg-Si-(Cu) precipitates, Acta Materialia 52 (2004) 4213-4227.

[122] M. Takeda, F. Ohkubo, T. Shirai, K. Fukui, Stability of metastable phases and microstructures in the ageing process of Al–Mg–Si ternary alloys, Journal of Materials Science 33 (1998) 2385-2390.

[123] Y. Birol, The effect of sample preparation on the DSC analysis of 6061 alloy, Journal of Materials Science 40 (2005) 6357-6361.

[124] K. Matsuda, S. Ikeno, K. Terayama, H. Matsui, T. Sato, Y. Uetani, Comparison of precipitates between excess Si-type and balanced-type Al-Mg-Si alloys during continuous heating, Metallurgical and Materials Transactions A 36 (2005) 2007-2012.

[125] A.K. Gupta, D.J. Lloyd, S.A. Court, Precipitation hardening in Al–Mg–Si alloys with and without excess Si, Materials Science and Engineering: A 316 (2001) 11-17.

[126] D. Maisonnette, M. Suery, D. Nelias, P. Chaudet, T. Epicier, Effects of heat treatments on the microstructure and mechanical properties of a 6061 aluminium alloy, Materials Science and Engineering A 528 (2011) 2718-2724.

[127] A. Hirose, N. Kurosawa, K. Kobayashi, H. Todaka, H. Yamaoka, Quantitative evaluation of softened regions in weld heat-affected zones of 6061-T6 aluminum alloy—Characterizing of the laser beam welding process, Metallurgical and Materials Transactions A 30 (1999) 2115-2120.

[128] H. Jamshidi Aval, S. Serajzadeh, A study on natural aging behavior and mechanical properties of friction stir-welded AA6061-T6 plates, The International Journal of Advanced Manufacturing Technology 71 (2014) 933-941.

[129] O.R. Myhr, Ø. Grong, H.G. Fjær, C.D. Marioara, Modelling of the microstructure and strength evolution in Al–Mg–Si alloys during multistage thermal processing, Acta Materialia 52 (2004) 4997-5008.

[130] L.E. Murr, G. Liu, J.C. McClure, A TEM study of precipitation and related microstructures in friction-stir-welded 6061 aluminium, Journal of Materials Science 33 (1998) 1243-1251.

[131] C.A.W. Olea, L. Roldo, J.F. dos Santos, T.R. Strohaecker, A sub-structural analysis of friction stir welded joints in an AA6056 Al-alloy in T4 and T6 temper conditions, Materials Science and Engineering: A 454-455 (2007) 52-62.

[132] V.A. Phillips, High resolution electron microscope observations on precipitation in Al-3.0% Cu alloy, Acta Metallurgica 23 (1975) 751-767.

[133] T.J. Konno, M. Kawasaki, K. Hiraga, Guinier-Preston zones observed by high-angle annular detector dark-field scanning transmission electron microscopy, Philosophical Magazine Part B 81 (2001) 1713-1724.

[134] C.-Y. Lee, D.-H. Choi, W.-B. Lee, S.-K. Park, Y.-M. Yeon, S.-B. Jung, Microstructures and Mechanical Properties of Double-Friction Stir Welded 2219 Al Alloy, Materials Transactions 49 (2008) 885-888.

[135] X. Feng, H. Liu, S. Suresh Babu, Effect of grain size refinement and precipitation reactions on strengthening in friction stir processed Al–Cu alloys, Scripta Materialia 65 (2011) 1057-1060.

[136] H.R. Shercliff, M.J. Russell, A. Taylor, T.L. Dickerson, Microstructural modelling in friction stir welding of 2000 series aluminium alloys, Mechanics & Industry 6 (2005) 25-35.

[137] C. Jonckheere, B. de Meester, A. Denquin, A. Simar, Torque, temperature and hardening precipitation evolution in dissimilar friction stir welds between 6061-T6 and 2014-T6 aluminum alloys, Journal of Materials Processing Technology 213 (2013) 826-837.

[138] Y. Yang, H. Dong, S. Kou, Liquation Tendency and Liquid-Film Formation in Friction Stir Spot Welding, Welding Journal 87 (2008) 202s-211s.

[139] F. Wideroe, T. Welo, Conditions for sticking friction between aluminium alloy AA6060 and tool steel in hot forming, Progress in Extrusion Technology and Simulation of Light Metal Alloys 491 (2012) 121-128.

[140] L. Wang, H. Yang, Friction in aluminium extrusion—part 2: A review of friction models for aluminium extrusion, Tribology International 56 (2012) 99-106.

[141] E. Orowan, The calculation of roll pressure in hot and cold flat rolling, Proceedings of the Institution of Mechanical Engineers 150 (1943) 140-167.

[142] T. Wanheim, N. Bay, A model for friction in metal forming processes, CIRP Annals-Manufacturing Technology 27 (1978) 189-194.

[143] G. Buffa, M. Cammalleri, D. Campanella, L. Fratini, Shear coefficient determination in linear friction welding of aluminum alloys, Materials & Design 82 (2015) 238-246.

[144] X. Ma, M.B. de Rooij, D.J. Schipper, Friction conditions in the bearing area of an aluminium extrusion process, Wear 278-279 (2012) 1-8.

[145] T. Long, W. Tang, A.P. Reynolds, Process response parameter relationships in aluminium alloy friction stir welds, Science and Technology of Welding and Joining 12 (2007) 311-317.

[146] H. Schmidt, J. Hattel, J. Wert, An analytical model for the heat generation in friction stir welding, Modelling and Simulation in Materials Science and Engineering 12 (2004) 143.

[147] B.C. Liechty, B.W. Webb, Modeling the frictional boundary condition in friction stir welding, International Journal of Machine Tools and Manufacture 48 (2008) 1474-1485.

[148] A.R.S. Essa, M.M.Z. Ahmed, A.-K.Y.A. Mohamed, A.E. El-Nikhaily, An analytical model of heat generation for eccentric cylindrical pin in friction stir welding, Journal of Materials Research and Technology 5 (2016) 234-240.

[149] O.T. Midling, Ø. Grong, A process model for friction welding of Al-Mg-Si alloys and Al-SiC metal matrix composites—I. Haz temperature and strain rate distribution, Acta Metallurgica et Materialia 42 (1994) 1595-1609.

[150] Ø. Frigaard, Ø. Grong, O.T. Midling, A process model for friction stir welding of age hardening aluminum alloys, Metallurgical and Materials Transactions A 32 (2001) 1189-1200.

[151] A. Gerlich, M. Yamamoto, T.H. North, Local melting and tool slippage during friction stir spot welding of Al-alloys, Journal of Materials Science 43 (2008) 2-11.

[152] MMPDS-06 : Metallic Materials Properties Development and Standardization (MMPDS), Federal Aviation Administration; Battelle Memorial Institute [distributor], Washington, D.C, Columbus, Ohio, 2011.

[153] H. Zhang, L. Li, D. Yuan, D. Peng, Hot deformation behavior of the new Al–Mg–Si–Cu aluminum alloy during compression at elevated temperatures, Materials Characterization 58 (2007) 168-173.

[154] J. Zhang, B. Chen, Z. Baoxiang, Effect of initial microstructure on the hot compression deformation behavior of a 2219 aluminum alloy, Materials & Design 34 (2012) 15-21.

[155] E. Cerri, E. Evangelista, A. Forcellese, H.J. McQueen, Comparative hot workability of 7012 and 7075 alloys after different pretreatments, Materials Science and Engineering: A 197 (1995) 181-198.

[156] M.R. Rokni, A. Zarei-Hanzaki, A.A. Roostaei, A. Abolhasani, Constitutive base analysis of a 7075 aluminum alloy during hot compression testing, Materials & Design 32 (2011) 4955-4960.

[157] M. Taheri-Mandarjani, A. Zarei-Hanzaki, H.R. Abedi, Hot ductility behavior of an extruded 7075 aluminum alloy, Materials Science and Engineering: A 637 (2015) 107-122.

[158] W.-S. Lee, Z.-C. Tang, Relationship between mechanical properties and microstructural response of 6061-T6 aluminum alloy impacted at elevated temperatures, Materials & Design 58 (2014) 116-124.

[159] S. Spigarelli, Study of hot workability of a heat treated AA6082 aluminum alloy, Scripta Materialia 49 (2003) 179-183.

[160] S.L. Yan, H. Yang, H.W. Li, X. Yao, Variation of strain rate sensitivity of an aluminum alloy in a wide strain rate range: Mechanism analysis and modeling, Journal of Alloys and Compounds 688 (2016) 776-786.

[161] G. Chen, J. Jiang, Z. Du, F. Han, H.V. Atkinson, Hot tensile behavior of an extruded Al–Zn–Mg–Cu alloy in the solid and in the semi-solid state, Materials & Design (1980-2015) 54 (2014) 1-5.

[162] N. Huber, E. Tyulyukovskiy, A new loading history for identification of viscoplastic properties by spherical indentation, Journal of Materials Research 19 (2011) 101-113.

[163] B.I. Bjørneklett, Ø. Grong, O.R. Myhr, A.O. Kluken, Modelling of grain boundary liquation in Al–Zn–Mg weldments, Science and Technology of Welding and Joining 4 (1999) 161-169.

[164] O. Reiso, H.-G. Øverlie, N. Ryum, Dissolution and melting of secondary Al2Cu phase particles in an AlCu alloy, Metallurgical Transactions A 21 (1990) 1689-1695.

[165] O. Reiso, N. Ryum, J. Strid, Melting of secondary-phase particles in Al-Mg-Si alloys, Metallurgical Transactions A 24 (1993) 2629-2641.

[166] R. Kaibyshev, F. Musin, D. Gromov, T.G. Nieh, D.R. Lesuer, Effect of liquid phase on superplastic behavior of a modified 6061 aluminum alloy, Scripta Materialia 47 (2002) 569-575.

[167] A. Gerlich, P. Su, M. Yamamoto, T.H. North, Effect of welding parameters on the strain rate and microstructure of friction stir spot welded 2024 aluminum alloy, Journal of Materials Science 42 (2007) 5589-5601.

[168] K.A.A. Hassan, P.B. Prangnell, A.F. Norman, D.A. Price, S.W. Williams, Effect of welding parameters on nugget zone microstructure and properties in high strength aluminium alloy friction stir welds, Science and Technology of Welding and Joining 8 (2003) 257-268.

[169] J.M. Chen, T.S. Sun, R.K. Viswanadham, J.A.S. Green, Grain boundary segregation of an Al-Zn-Mg ternary alloy, Metallurgical Transactions A 8 (1977) 1935-1940.

[170] R.G. Song, M.K. Tseng, B.J. Zhang, J. Liu, Z.H. Jin, K.S. Shin, Grain boundary segregation and hydrogen-induced fracture in 7050 aluminium alloy, Acta Materialia 44 (1996) 3241-3248.

[171] A. Joshi, C.R. Shastry, M. Levy, Effect of Heat Treatment on Solute Concentration at Grain Boundaries in 7075 Aluminum Alloy, Metallurgical Transactions A 12 (1981) 1081-1088.

[172] A. Gerlich, M. Yamamoto, T.H. North, Strain rates and grain growth in Al 5754 and Al 6061 friction stir spot welds, Metallurgical and Materials Transactions a-Physical Metallurgy and Materials Science 38A (2007) 1291-1302.

[173] O. Frigaard, O. Grong, J. Hjelen, S. Gulbrandsen-Dahl, O. Midling, Characterization of the subgrain structure in friction stir welded aluminium alloys using the SEM-EBSD technique, Proceedings of the 1st International Symposium on Friction Stir Welding, June, 1999, pp. 14-16.

[174] M.R. Rokni, A. Zarei-Hanzaki, A.A. Roostaei, H.R. Abedi, An investigation into the hot deformation characteristics of 7075 aluminum alloy, Materials & Design 32 (2011) 2339-2344.

Appendix A

To obtain the amount of energy needed to overcome the frictional resistance in the welding equipment used in this study, experiments have been conducted. For these experiments, no welding tool was installed in the welding equipment, and no workpiece was present. The typical weld procedure was followed to find a rotational speed-dependent amount of energy that has to be subtracted from the measured total energy input to neglect the energy needed to rotate the machine parts at the respective rotational speed.

The welding equipment followed the welding procedure without the tool, moving the machine parts included in the rotation and axial movement of the tool parts. According to this approach, the measured values of torque and force can be used to calculate the energy needed to overcome the frictional resistance in the welding equipment following Equation (2). This approach was followed on several occasions during the implementation of the work, as the measured values are affected by outside temperature, welding history of the equipment, etc.

Figure 8.1 (a) shows a typical measurement of torque and force during the experiments to obtain the energy needed to overcome the frictional resistance in the movable parts of the welding equipment. Both force and torque remain relatively constant at lower values during the procedure. The values of torque depend on the constant rotational speed and determine the calculated energy, as shown in Figure 8.1 (b).

Calculating the energy input according to Equation (2) shows that the energy input during RFSSW process without the welding tool $Q_{equipment}$ is mainly dominated by the energy needed to rotate the tool parts. The low values of force needed to plunge and retract the tool parts do not consume a significant amount of energy. As the torque is essentially constant during the process, the average energy needed to overcome the frictional resistance per second can be calculated from the linear relation shown in Figure 8.1 (b). To obtain the amount of energy consumed by the frictional resistance during an entire weld process $Q_{equipment}$, the result has to be multiplied by the total time of the welding process.

Within the practical rotational speed interval from 1000 to 3000 rpm, the energy needed to overcome the frictional resistance in the welding equipment for an entire weld can be calculated using the total time of the welding process (s) and tool rotational speed (1/min). The amount of energy calculated in this manner was subtracted from the calculated total energy, as discussed in Chapter 4.1.4.

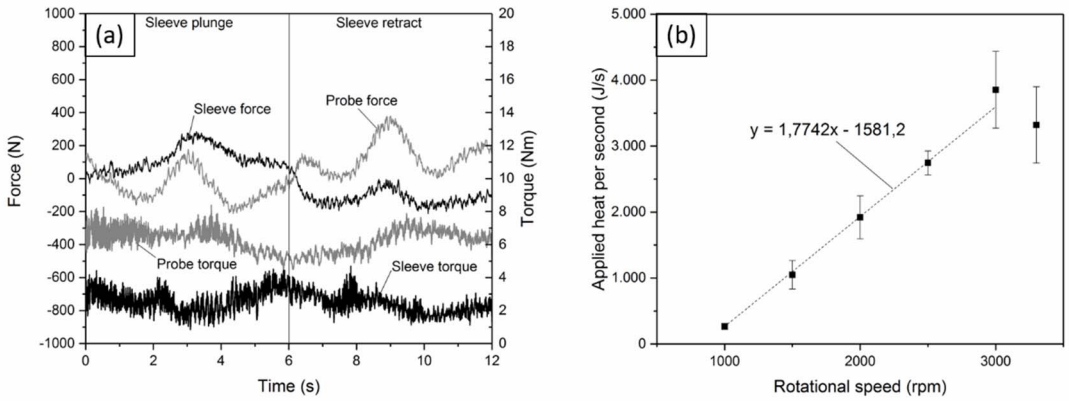

Figure 8.1 Keyhole repair process without a tool: (a) typical force and torque distribution using 2000 rpm and (b) applied energy in RFSSW process without a tool at different rotational speeds.

The measured values of torque and therefore energy vary between different days of measurement, as the measured values are affected by the outside temperature, the welding history of the equipment, etc. The values shown in Figure 8.1 (b) are averaged. Accordingly, it is advised to measure the energy input of one test series in one day. Measurements that have to be compared to tests conducted on several occasions should be averaged by repetition on different days.

Appendix B

This section shows the influence of the process parameters, workpiece thickness and tool size on the thermal cycle characteristics for AA 7075-T651 and AA 2219-T851.

Aluminum alloy 7075-T651

Analysis of the characteristic thermal cycle with high heating and cooling rates and short exposure times to the peak temperature in AA 7075-T651 confirmed the findings in AA 6061-T6 reported in Chapter 5.2 regarding dependence on the process parameters, sheet thickness and tool size.

Figure 8.2 shows the thermal cycle in 3 mm-thick sheets of AA 7075-T651 BM welded using the medium size tool at different rotational speeds and sleeve plunge and retract speeds. The peak temperature in the HAZ in AA 7075-T651 is assumed to follow the same trend as reported for AA 6061-T6, and as illustrated in Figure 6.15 for 3 mm-thick sheets welded using the medium size tool, it increases with increasing tool rotational speed and with decreasing sleeve plunge and retract speeds. As the number of measurements is relatively small, the trend of increasing peak temperature with increasing rotational speed is not strongly pronounced. If the outlier measurement at 1800 rpm is neglected, then at 9 mm from the center of the weld, the highest peak temperature was measured at 373°C, and the lowest peak temperature, at 344°C, depending on the process parameters. At 17 mm from the center of the weld, the highest peak temperature was measured at 277°C, and the lowest peak temperature, at 242°C. Similar to the findings in AA 6061-T6, a relatively linear relationship between the energy input and the peak temperature can be found [31], but consideration of the influence of the individual process parameters is necessary, as described in Chapter 5.2.

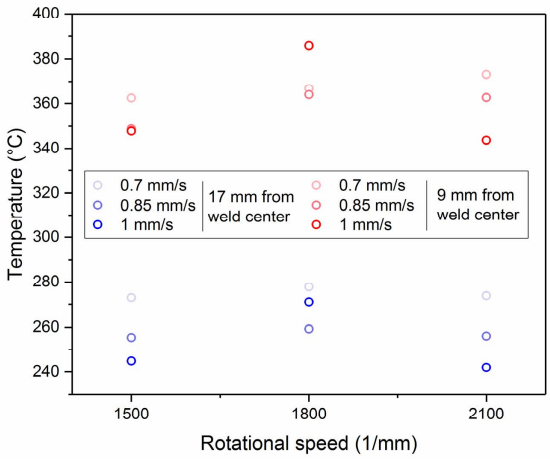

Figure 8.2 Peak temperatures in the HAZ of 3 mm sheets of AA 7075-T651 depending on the rotational speed and sleeve plunge and retract speed. The same test series was used to calculate the energy input depending on the tool revolutions per mm plunge and retract in Figure 5.3.

Figure 8.3 shows the thermal cycle in 3 and 6 mm-thick sheets of AA 7075-T651 BM welded using the medium size tool at a 1800 rpm rotational speed and 0.95 mm/s sleeve plunge and retract speeds.

Similar to the observation in AA 6061-T6 – for comparison, see Chapter 6.3.1 – an increased sheet thickness leads to longer exposure and a higher peak temperature in the HAZ, Figure 8.3. Increasing the sheet thickness from 3 to 6 mm increases the peak temperature in the HAZ by approximately 30°C and doubles the exposure time in the shown measurements. The influence of the tool size follows the characteristic reported for AA 6061-T6 in Chapter 6.3.1. The peak temperature varies from approximately 360 to 380°C at 9 mm from the center of the weld and from approximately 275 to 290°C at 17 mm from the center of the weld in the HAZ depending on the sheet thickness.

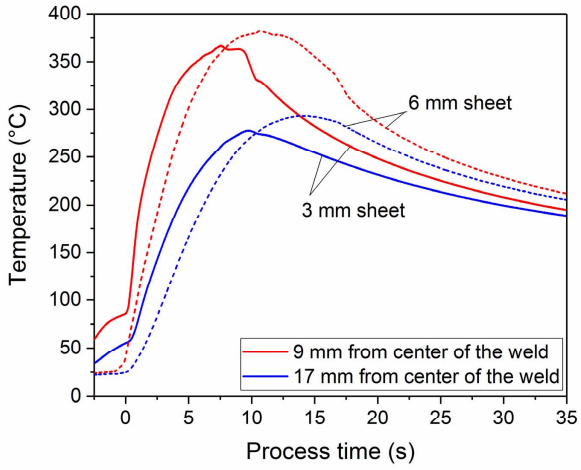

Figure 8.3 Influence of sheet thickness on the typical thermal cycle in AA 7075-T651 welded using the medium size tool at 1800 rpm and 0.95 mm/s.

Aluminum alloy 2219-T851

The weld thermal cycle in AA 2219-T8 features the typical characteristic of repair welds using RFSSW as reported in Chapter 5.2. An increase in sheet thickness was found to increase the exposure time to elevated temperatures and increase the peak temperatures in the HAZ while keeping the peak temperatures in the SZ similar.

Figure 8.4 shows the thermal cycle in 3 and 6 mm-thick sheets of the AA 2219-T851 BM using the medium size tool welded at a 1350 rpm rotational speed and 0.6 mm/s sleeve plunge and retract speeds . Similar to the observations from AA 6061-T6 and AA 7075-T651, an increased sheet thickness leads to longer exposure and a higher peak temperature in the HAZ. Increasing the sheet thickness from 3 to 6 mm increases the peak temperature in the HAZ by approximately 50°C and doubles the exposure time in the measurements shown. The peak temperature in the SZ is measured at approximately 520°C, whereas it varies from approximately 350 to 400°C at 9 mm from the center of the weld and from approximately 250 to 300°C at 17 mm from the center of the weld in the HAZ, depending on the sheet thickness.

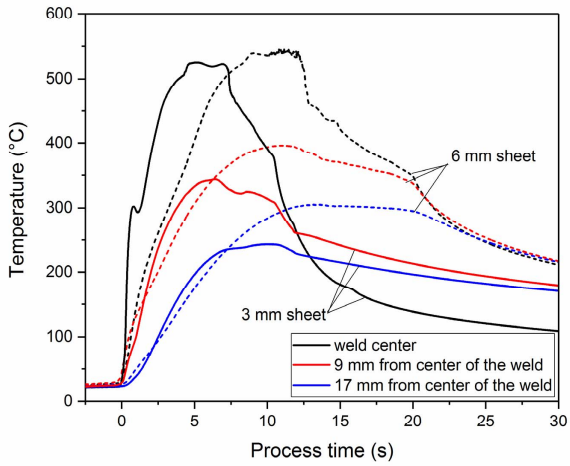

Figure 8.4 Influence of sheet thickness on the typical thermal cycle in AA 2219-T851 welded using the medium size tool at 1350 rpm and 0.6 mm/s. [105]

Appendix C

The device used to measure the pressure at the welded interface during repair welds using RFSSW is shown in Figure 8.5. A rectangular sample is inserted into the rectangular cutout in the center of the device. The sample features a steel rod that connects the position of the welded interface to a piezoelectric force sensor.

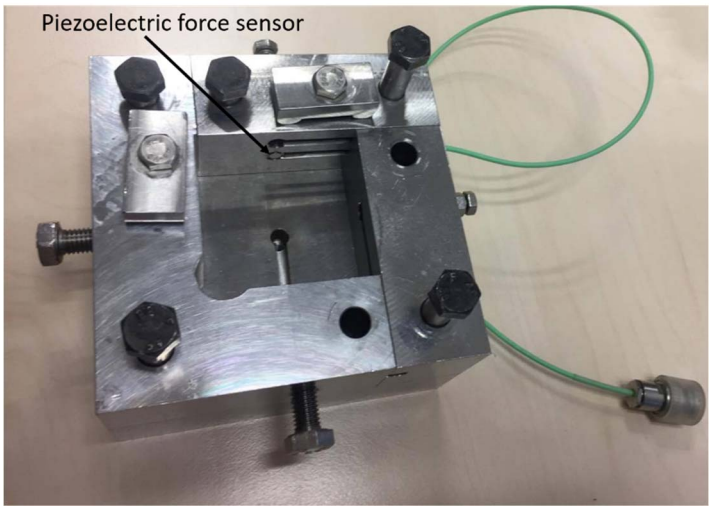

Figure 8.5 Device used to measure the pressure at the welded interface during RFSSW.

The positioning of the steel rod in the welded specimen is indicated in Figure 8.6. A repair weld is conducted using RFSSW in the center of the specimen. During the weld, the sleeve plunges downwards into the aluminum. Since the sleeve is positioned to be as close to the steel rod without contacting it, it exposes the front surface of the steel rod. During the sleeve retraction stage of the RFSSW process, the probe pushes the material in the tool cavity downwards and towards the sides to refill the cavity under the retracting sleeve. At this stage of the process, the steel rod transfers the force of the refilling material sidewards to the piezoelectric force sensor. The sensor data are used to calculate the pressure at the welded interface during the welding process.

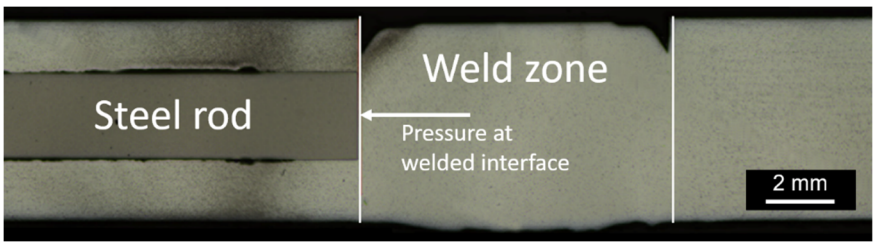

Figure 8.6 Low-magnification overview of a sample of AA 7075-T651 welded using the medium size tool with a steel rod used to transfer the force on the welded interface to a force sensor.

A representative measurement comparing the pressure at the front surface of the steel rod to the pressure at the front surfaces of the sleeve and probe during a repair weld using RFSSW is shown in

Figure 8.7. The dashed lines indicate the beginning and end of the refilling in the front surface area of the steel rod. The pressure at the welded interface reaches its peak values during the second half of the process in the sleeve retraction phase. As the front surface of the steel rod is increasingly covered with aluminum in the refilling stage of the process, the pressure at the interface decreases in this period. The values obtained in this manner are affected by the freedom of movement of the steel rod, the positioning of the welding tool and the clogging of the steel rod's front surface with aluminum. With this in mind, the values of interface pressure obtained are a first estimate.

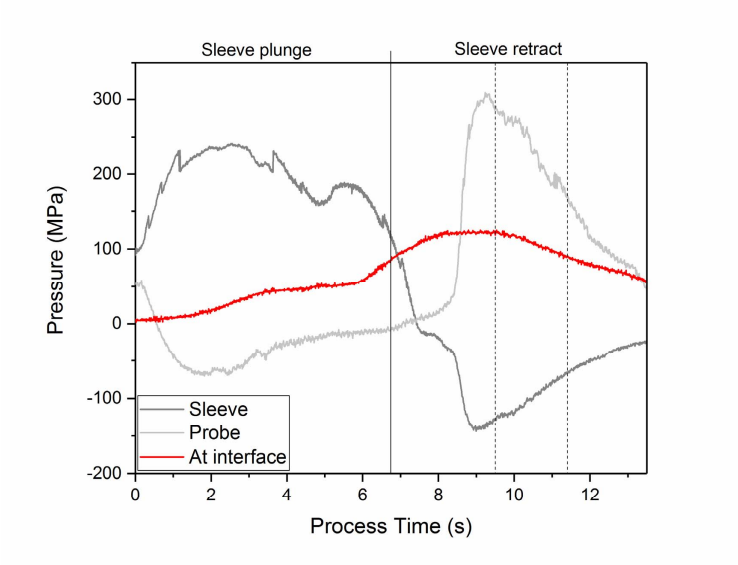

Figure 8.7 Pressure distribution on the front surface of the sleeve, probe and steel rod during a repair weld using RFSSW in AA 7075-T651 using the medium size tool.

To analyze the strength of the welded interface, micro flat tensile specimens were machined from repair welded sheets, Figure 8.8. The welded interface is included in the gauge of the tensile samples. Two specimens welded employing the same process parameters were analyzed for each of the alloys of interest and 6 micro flat tensile specimens were extracted from each welded specimen.

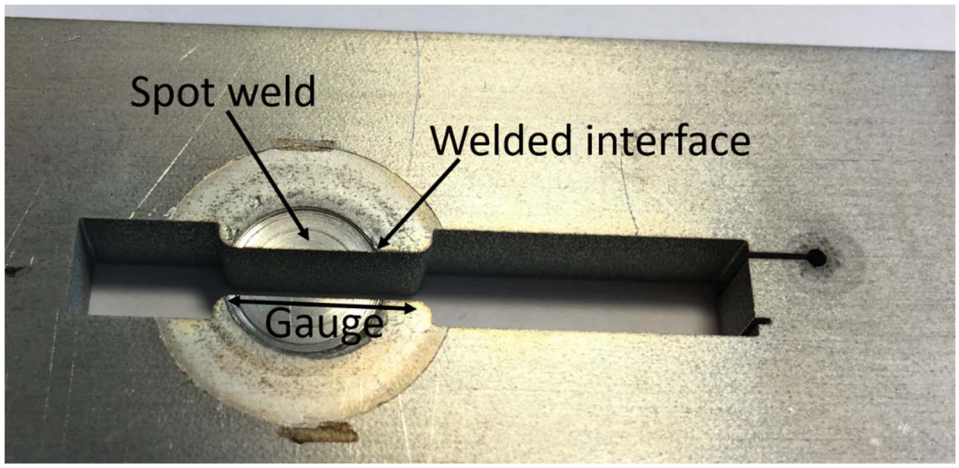

Figure 8.8 Position of the micro flat tensile specimens.

At 166 ±3.1 MPa for AA 6061-T6 and at 354 ±1.4 MPa for AA 7075-T651, the YS was found to be slightly higher than that of standard welded tensile specimens, as the area of lowest hardness was not included in the small micro flat tensile specimens; compare with the typical hardness distribution reported in Chapter 6.3.3 and 6.2.3.In AA 2219-T651, the YS of 165 ±1.6 MPa was found to be slightly lower than the values of the standard specimens.

All of the analyzed micro flat tensile specimens fractured in a region outside of the SZ, as indicated in Figure 8.9. The average UTS was measured at 264 ±2.9 MPa for AA 6061-T6, at 505 ±1.8 MPa for AA 7075-T651 and at 307 ±1.1 MPa for AA 2219-T851. The fracture occurs further from the center of the weld than the welded interface because the strength in these regions is reduced. Additionally, the micro flat tensile specimens do not contain critical crack initiation points such as remnants of the plug-workpiece interface or surface imprints of the sleeve. The UTS of the respective welded interface is thus assumed to be higher than the observed values because the fracture did not occur in the welded interface.

The observed values of YS and UTS for AA 2219-T8 are lower than the values of the standard welded tensile specimen, which started yielding in the region of lowest strength. Even small inaccuracies in sample production can influence the results of the micro flat tensile testing. It is thus assumed that geometrically inaccurate sample production distorted the measurement for AA 2219-T8. The measurements of this alloy can thus not be considered for further analysis.

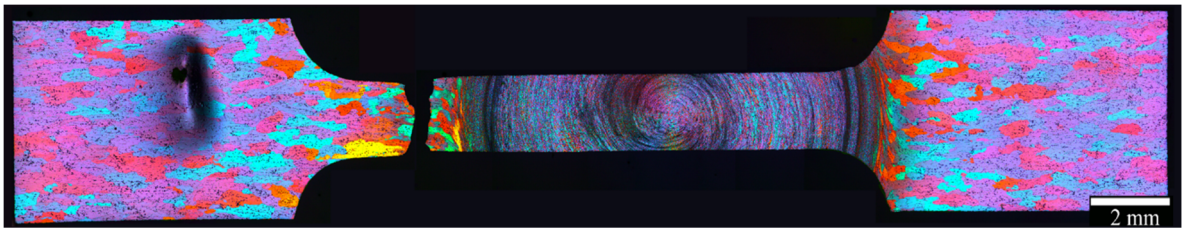

Figure 8.9 Micro flat tensile sample of AA 2219-T8 indicating the typical fracture location. The inhomogeneity on the left clamping area is caused by the sample preparation process.

Appendix D

Figure 8.10 shows solution heat-treated samples of the alloys of interest. The heat treatment was conducted at 530°C for 1 h for AA 2219 and AA 6061 and at 480°C for 1 h for AA 7075. The samples were quenched in water to RT and stored at RT for 8 weeks before the hardness measurements were conducted. The heat treatment caused microstructural changes such as grain growth. In AA 6061, the grain size increased in the upper half of the SZ, whereas grain growth occurred in the entire SZ in AA 2219 and along the shear layer in the SZ in AA 7075. The grain size of the small recrystallized grains in the SZ is on average 27 µm for AA 6061 and 9 µm for AA 7075. In AA 2219, the grain size in the SZ increased to 288 µm on average. The difference in the hardness of the regions in the SZ that exhibit small grains compared to the hardness in the surrounding BM is used to assess the strength contribution of the grain size for the alloys of interest.

The hardness in the small-grain region in the SZ of AA 6061 is 72 $HV_{0.2}$ with a standard deviation of 3.4 %, whereas the BM exhibits a hardness of 70.4 $HV_{0.2}$ and a standard deviation of 3.0 %. In AA 2219, the hardness in the small-grain region in the SZ is 94.1 $HV_{0.2}$ with a standard deviation of 4 %, whereas the BM exhibits a hardness of 87.7 $HV_{0.2}$ and a standard deviation of 3.9 %. In AA 7075, the hardness in the small-grain region in the SZ is 148.9 $HV_{0.2}$ with a standard deviation of 4.5 %, whereas the BM exhibits a hardness of 149.5 $HV_{0.2}$ and a standard deviation of 4.4 %. A significant difference in the increase in hardness with decreasing grain size thus cannot be reported for AA 6061 and AA 7075 in the reported condition. Still, AA 2219 shows a slight trend towards an increase in hardness, which should be considered when the results of this work are interpreted.

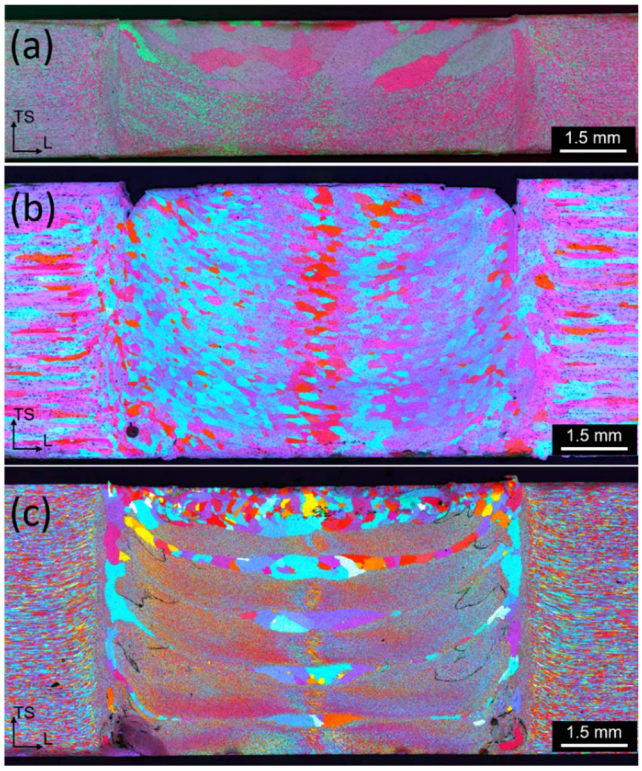

Figure 8.10 Low-magnification overview of post-weld solution heat-treated samples of AA 6061-T6 (a), AA 2219-T851 (b) and AA 7075-T651 (c).

Appendix E

Figure 8.11 indicates that the SZ diameter increases with increasing sleeve revolutions per mm plunge and retract, which is known to increase the energy input, as shown in Figure 5.3. Still, at this point, the statistical significance of the trend cannot be verified because of the large standard deviation at approximately 35 1/mm revolutions per mm plunge and retract.

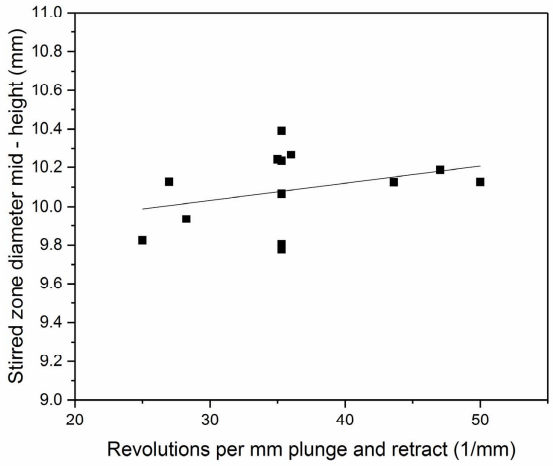

Figure 8.11 Trend towards larger SZ diameters with increasing sleeve revolutions per mm plunge and retract in 3 mm sheets of AA 7075-T651 welded using the medium size tool.

Appendix F

Figure 8.12 indicates that the distance from the region of lowest strength to the center of the weld increases with increasing sleeve revolutions per mm plunge and retract in AA 6061-T6, which is known to increase the energy input, as shown in Figure 5.3.

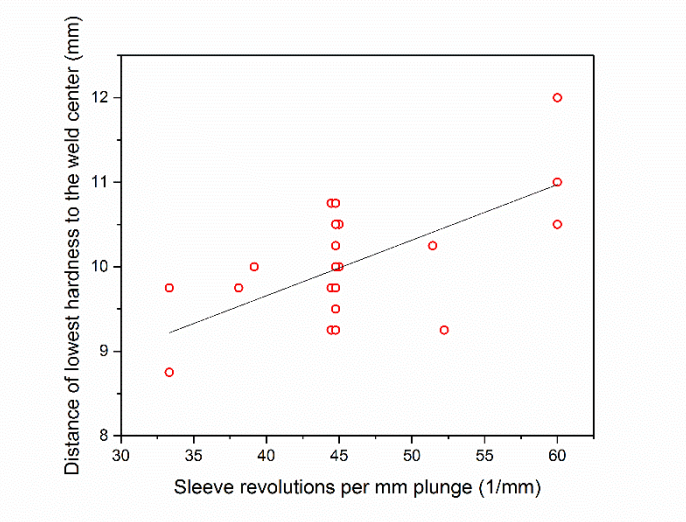

Figure 8.12 Trend towards increasing distance from the regions of lowest hardness to the center of the weld with increasing sleeve revolutions per mm plunge in 6 mm sheets of AA 6061-T6 welded using the medium size tool.

Appendix G

Figure 8.13 indicates that the distance from the region of lowest strength to the center of the weld increases with increasing sleeve revolutions per mm plunge and retract in AA 7075-T651, which is known to increase the energy input, as shown in Figure 5.3. Still, at this point, the statistical significance of the trend cannot be verified because of the low variation in sleeve revolutions per mm plunge and retract within the process parameter window tested to analyze the mechanical properties.

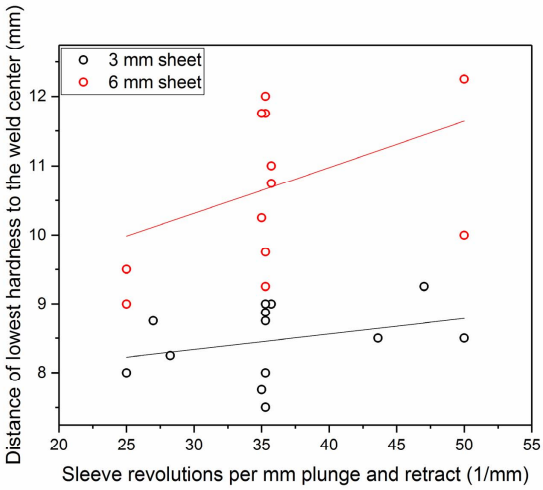

Figure 8.13 Trend towards increasing distance from the regions of lowest hardness to the center of the weld with increasing sleeve revolutions per mm plunge and retract in 3 and 6 mm sheets of AA 7075-T651 welded using the medium size tool.

Appendix H

This section shows a detailed literature review and analysis of the melting behavior of the alloys regarded in this study.

Incipient melting in AA7075

A basic analysis of the incipient melting behavior of AlMgSi(Cu) alloys was reported by Droenen and Ryum [111]. They analyzed the melting behavior of the ternary T-phase and η-phase by up-quenching AlMgZn alloys in approximately 4 s to high temperatures followed by subsequent microstructural analysis. The η-phase was found to melt spontaneously at or above 475°C and to dissolve into the matrix at temperatures below 475°C. The T-phase melted spontaneously at or above 489°C and, after some period of time, at temperatures as low as 480°C.

Phenomena believed to be caused by incipient melting are commonly observed during friction welding processes of AA 7075, for example, by Gerlich et al. [151], who performed friction stir spot welding in AA 7075-T6. They observed strain rates of approximately 600 1/s in the SZ when employing low rotational speeds and low strain rates of less than 20 1/s with rotational speeds greater than 1500 rpm. This dramatic decrease in the calculated strain rate was thought to be indicative of tool slippage occurring due to incipient melting of secondary phases. The calculations of the authors indicate that local melted droplets formed during friction stir spot welding would completely dissolve during the cooling phase of the thermal cycle, removing all evidence indicating that incipient melting had occurred [100, 167]. However, the investigators observed several Cu-, Mg- and Zn-rich grain boundary regions in the SZ. This observation was associated with local melting and subsequent eutectic film formation based on more detailed observations and assumptions made by [168] in AA 7010.

Incipient melting was also assumed to occur by Zhao et al. [64] during conventional RFSSW of similar 7B04-T74 aluminum alloy sheets with a composition close to that of AA 7075. The authors also reported the abovementioned secondary phase-enriched grain boundary films in the SZ, assuming that they indicated the occurrence of incipient melting.

Bjørneklett et al. [163] reported similar but more pronounced metallographic observations of local melting at grain boundary regions when samples of two different AlZnMg extrusions were heated at 330°C/s to 475°C. Incipient melting by spontaneous melting of undissolved secondary phase particles in the as-received base material was reported. At a heating rate of 100°C/s, dissolution of the secondary phases was achieved, and no melting occurred.

Based on the basic material behavior reported by Droenen and Ryum [111] and the often reported phenomena associated with incipient melting during friction-based processing of AA 7075 or similar alloys, it is reasonable to assume that thermal cycles with peak temperatures above 475°C and high heating rates can lead to incipient melting. However, finding supporting metallographic evidence is the key issue as it was reported that local melted droplets formed during welding would completely dissolve during the cooling phase of the thermal cycle, removing all evidence indicating that incipient melting had occurred [100, 167].

Incipient melting in AA 6061

For AlMgSi alloys, the incipient melting behavior depends on the ratio of the Mg and Si contents as reported by Reiso et al. [165]. In their investigation, AlMgSi alloys were up-quenched to various temperatures around 590°C in approximately 20 s. In a quasi-binary Al-Mg_2Si alloy, one melting reaction was found. The Mg_2Si particles melted together with the surrounding matrix at 593°C and, upon solidification, formed a binary eutectic structure consisting of Mg_2Si and α-Al. Starink [77] confirmed the melting peak at approximately 595°C. In alloys with a Si content in excess of that needed to form Mg_2Si, two additional melting reactions were reported [165]. At peak temperatures of 560°C, α-Al, Mg_2Si and Si particles in contact with one another melted and formed a ternary eutectic on the grain boundaries upon solidification. At 577°C, free Si particles melted and formed a binary eutectic of α-Al and Si.

Gerlich et al. [151] reported increasing strain rates of approximately 100 to 400 s^{-1} during friction stir spot welding of AA 6061-T6 upon increasing the rotational speed from 1000 to 3000 rpm. This is a completely different behavior compared to that of AA 7075. Gerlich et al. [172] observed strain rates ranging from 55 to 395 s^{-1} when friction stir spot welding AA 6061-T6 in a peak temperature range from 400 to 550°C. Again, the strain rates were found to increase together with the rotational speed of the tool. Based on these observation, the investigators concluded in both studies that no incipient melting occurred and that the assumption of a no-slip condition is appropriate.

Frigaard et al. [173] calculated the strain rate close to the tool during friction stir spot welding of AA 6082 and AA 7108 from 1.6 to 17 s^{-1}. These values were an order of magnitude lower than those expected based on the tool rotational speed during the welding operation. The authors suggested that this discrepancy was caused by local melting facilitating slippage between the tool periphery and adjacent material. As AA 6082 is an alloy with a Si content in excess of that necessary to form Mg_2Si [71], melting is assumed to occur at temperatures above 560°C. The authors concluded that these temperatures were reached during friction stir spot welding of AA 6082.

AA 6061 is an AlMgSiCu alloy with a slightly higher Si content than the stoichiometric ratio of Mg_2Si [71]. The basic analysis of the material behavior of AlMgSi alloys by [165] suggests that incipient melting can be expected on a small scale at high heating rates to temperatures above 560°C if the AlMgSi alloy in question exhibits a Si content in excess of that necessary to form Mg_2Si. The melting temperature of the Mg_2Si phase was reported at approximately 590°C. No basic research was found on the melting reactions in AlMgSiCu alloys. For friction welding operations, no studies reporting incipient melting in AA 6061 were found.

Incipient melting in AA 2219

Incipient melting of the Al_2Cu phase present in AlCu alloys was investigated by Reiso et al. [164]. When up-quenching AlCu alloy samples to various temperatures around 555°C in 20 s, the authors observed melting of the Al_2Cu phase at or above the eutectic temperature of 547°C. The secondary phase melted together with the surrounding matrix in less than one second to form a liquid with a chemical composition close to the eutectic composition.

Long et al. [145] reported that to explain the flow stress observations during FSW of AA 2219-T87, either incipient melting or sliding friction has to occur. Yang et al. [138] reported molten structures in the SZ of AA 2219-T851 during friction stir spot welding. Clear microstructural evidence was found in the form of large eutectic films scattered in the stir zone.

In AA 2219, melting occurs above the eutectic temperature of 547°C. Incipient melting reactions below the eutectic temperature do not occur, as because of its composition, AA 2219 shows quasi-binary AlCu alloy behavior.

Slow heating rate

To analyze the melting behavior of the alloys of interest when exposed to slow heating rates to high temperatures, samples were tested using DSC, Figure 8.14. During the analysis, the samples were heated to 460°C and then were held isothermal for 15 min at 460°C. Next, further heating at 10°C/s was performed. The applied thermal cycle is assumed to cause complete dissolution of all strengthening precipitates, revealing the melting behavior of the alloys for all thermal cycles that cause a similar dissolution reaction.

The first melting reaction is observed in AA 7075 above 527°C, confirming the reported behavior [161, 174]. This melting reaction can be related to the onset of extensive melting, which is believed to start at inhomogeneities such as secondary phases.

In AA 2219, a large endothermic melting reaction above 545°C occurs, followed by extensive melting at higher temperatures. This corresponds to the eutectic temperature of the binary AlCu-phase, which is reported to be approximately 548°C [138]. Some particles with a composition close to that of θ are assumed to remain present in AA 2219 because the Cu content is above the solute solubility of 5.65 wt-% [138]. These particles melt together with the surrounding matrix, thereby causing the large melting reaction.

AA 6061 shows melting reactions at significantly higher temperatures, i.e., above 580°C which is slightly lower than the reported melting temperature of the Mg_2Si phase [165]. It is assumed that the endothermic reaction corresponds to the melting of secondary phases with a composition close to that of the equilibrium phase. The small shape of the reaction peak suggests that few particles exist at this temperature. At higher temperatures, the onset of melting is followed by a short transition range of no reaction, which is then followed by extensive melting, as reported by Kaibyshev et al. [166].

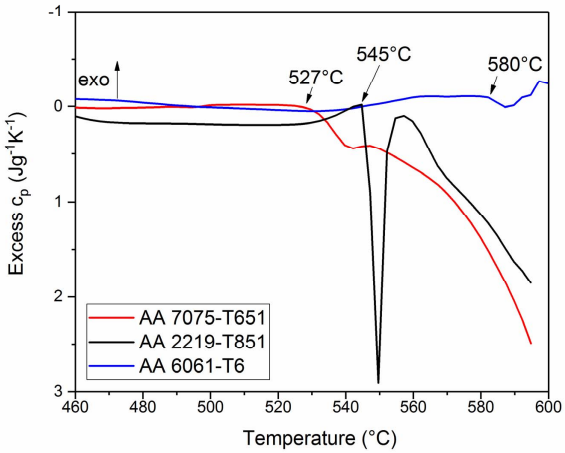

Figure 8.14 DSC thermogram in a high-temperature regime showing the onset of melting for the alloys of interest.

List of Figures

List of Tables